TURUN YLIOPISTO

Age and genesis of the high metamorphic grade Kultanummi gold prospect, southern Finland

Niko Heiskanen

Geology
Master's thesis
Credits: 30 ECTS

Supervisors:
Jaakko Kara
Esa Heilimo

21.10.2025
Turku

Master's thesis

Subject: Bedrock geology
Author: Niko Heiskanen
Title: Age and genesis of high metamorphic grade Kultanummi gold prospect, southern Finland
Supervisors: Jaakko Kara & Esa Heilimo
Pages: 62 pages + 3 appendixes
Date: 21.10.2025

Bedrock of southern Finland is known for hosting multiple major gold deposits, which have been formed during Svecofennian orogeny ca. 1.92 – 1.79 Ga ago. It can be divided into two major phases: the Fennian (1.89 – 1.86 Ga) and Svecobaltic (1.83 – 1.79 Ga). During Fennian phase the majority of the crust was formed, but the metamorphic peak in southern Finland was achieved during Svecobaltic phase. An extensional period is interpreted between the major orogenic stages related to orogenic collapse.

Kultanummi prospect is located near the city of Salo, and it is part of the Uusimaa Belt. It has been studied by Geological Survey of Finland (GTK) in early 2000s including a master's thesis focusing on the local geology. However, the age relationships compared to geological evolution of southern Finland and the possible deposit type are still unclear. In this study these two things were studied, and formation of mineralization was attempted to be linked to the evolution of regional bedrock. Field work was conducted in the Kultanummi area during Spring 2024, and from the collected samples, several thin sections were made. From these thin sections the most suitable ones were selected for scanning electron microscope analysis. With this the suitable minerals for age determination were studied, i.e. zircon, monazite and rutile. Minerals were dated with U-Pb method with laser-ablated inductively coupled mass spectrometer in Geological Survey of Finland research laboratory at Espoo.

Based on the results on this study, several age populations can be interpreted from Kultanummi. Firstly, zircon populations show age populations related to earlier events before Svecofennian orogeny (ca. 2.71 – 1.91 Ga) and furthermore ages related to Fennian phase (ca. 1.88 Ga) and extensional stage (ca. 1.86 Ga). Secondly, monazite age populations also show some ages related to Fennian phase (ca. 1.87 Ga), but they mainly show ages related to metamorphic peak event of Uusimaa Belt (ca. 1.815 Ga) during Svecobaltic phase and hydrothermal activity (ca. 1.79 Ga) after the metamorphic peak. Thirdly, single rutile population shows ages related to same hydrothermal activity (ca. 1.78 Ga) than one monazite population.

Kultanummi is untypical gold prospect compared to other gold prospects in southern Finland due to its high metamorphic grade and unusual mineralogy, but it can be interpreted to represent orogenic gold deposit with Al-rich fluid. Gold in Kultanummi is closely associated with sillimanite- and cordierite-rich lithologies and it tends to be structurally controlled. Sillimanite is considered to be an alteration product from Al-rich fluid, and this fluid activity is interpreted to occurred after 1.80 Ga. Based on the results, Kultanummi is interpreted to be an orogenic gold deposit, which has been formed from Al-rich fluid activity between 1.80 – 1.77 Ga.

Keywords: Svecofennian orogeny, orogenic gold, geochronology, U-Pb dating, LA-ICP-MS

Pro gradu -tutkielma

Pääaine: Kallioperägeologia
Tekijä: Niko Heiskanen
Otsikko: Age and genesis of high metamorphic grade Kultanummi gold prospect, southern Finland
Ohjaajat: Jaakko Kara & Esa Heilimo
Sivumäärä: 62 sivua + 3 liitettä
Päivämäärä: 21.10.2025

Etelä-Suomen kallioperästä tunnetaan useita huomattavia kultakohteita, jotka ovat muodostuneet Svekofennisen orogenian aikana n. 1,92–1,79 miljardia vuotta sitten. Siitä voidaan erottaa kaksi päävaihetta, jotka ovat Fennian (1,89–1,86 Ga) ja Svekobaltian (1,83–1,79 Ga) vaiheet. Suurin osa kallioperästä on muodostunut Fennian vaiheen aikana, mutta Etelä-Suomen metamorfinen huippuvaihe on saavutettu Svekobaltian vaiheen aikana. Näiden kahden vaiheen välissä on tulkittu olevan ekstensionaalinen vaihe, jonka on katsottu liittyvän orogeeniseen romahdukseen.

Kultanummen kultaesiintymä sijaitsee lähellä Salon kaupunkia ja se on osa Uudenmaan jaksoa. Sitä on tutkittu Geologian tutkimuskeskuksen (GTK) toimesta 2000-luvun alussa, ja yksi pro gradu -tutkielma tehtiin siellä samaan aikaan. Aiemmista tutkimuksista huolimatta Kultanummen mineralisaation ikä ja mahdollinen esiintymätyyppi eivät ole selvillä. Tämän tutkimuksen tarkoitus oli selvittää näitä kahta edellä mainittua asiaa sekä yhdistää mineralisaation muodostuminen alueelliseen kallioperän kehitykseen. Kenttätyöt toteutettiin keväällä 2024, ja kentältä kerätyistä näytteistä tehtiin ohuthieet, joista valittiin edustavimmat jatkotutkimuksia varten elektronimikroskoopille. Tämän avulla tunnistettiin ikämääritettäviä mineraaleja, kuten zirkoneja, monatsiittia ja rutiilia. Mineraalit ikämääritettiin U-Pb menetelmällä laserherätteisellä induktiivisestikytketyllä massaspektrometrilla GTK:n Espoon laboratoriossa.

Saatujen tulosten perusteella Kultanummelta voidaan havaita eri ikäpopulaatioita. Ensiksi, zirkoneista on havaittavissa ikäpopulaatiot liittyen Svekofennistä orogeniaa edeltäviin tapahtumiin (n. 2,71–1,91 Ga), Svekofennisen orogenian Fennian vaiheeseen (n. 1,88 Ga) ja tämän jälkeiseen ekstensionaaliseen vaiheeseen (n. 1,86 Ga). Toiseksi, monatsiiteista on havaittavissa ikäpopulaatiot liittyen Fennian vaiheeseen (n. 1,87 Ga), Uudenmaan jakson metamorfiseen huippuvaiheeseen (n. 1,815 Ga) ja tämän jälkeiseen fluiditoimintaan (n. 1,79 Ga). Kolmanneksi, rutiileista on havaittavissa vain yksi ikäpopulaatio liittyen fluiditoimintaan (n. 1,78 Ga) monatsiittien tapaan.

Kultanummi on epätyypillinen kultaesiintymä verrattuna muihin Etelä-Suomen kultakohteisiin, johtuen sen korkeasta metamorfoosiasteesta ja epätyypillisestä mineralogiasta. Kultamineralisaatio on läheisesti kytköksissä sillimaniitti- ja kordieriitti-rikkaiden litologioiden kanssa ja siinä on havaittavissa rakennekontrolli. Sillimaniitin voidaan tulkita olevan muuttumismineraali ja se on syntynyt fluiditoiminnan johdosta 1,80 Ga jälkeen. Tulosten perusteella esiintymätyyppi edustaa orogeenistä kultaesiintymää, joka on muodostunut Al-rikkaan fluiditoiminnan seurauksena noin 1,80–1,77 Ga.

Avainsanat: Svekofenninen orogenia, orogeeninen kulta, geokronologia, U-Pb ikämääritys, LA-ICP-MS

Contents

1 Introduction

Age determination of gold deposits is essential for understanding their connection to the evolution of bedrock which they are hosted in. This is also the case in Finland as it is known for hosting multiple gold deposits with varying ages (Eilu, 2015). Bedrock of Finland consists mainly of Archean and Proterozoic rocks, and it is divided into several provinces (Figure 1). Major part of the bedrock was formed during Svecofennian orogeny, which took place between ca. 1.9 – 1.8 Ga ago (Figure 2). During this time, multiple gold deposits have been formed, and therefore many gold deposits can be found from southern Finland (Figure 3). Most of the prospects are characterised to be orogenic gold, and the most prominent in southern Finland are Satulinmäki, Riukka (Saalmann et al., 2009) and Jokisivu (Saalmann et al., 2010). In addition, some epithermal gold deposits are also found in southern Finland, for example Kutemajärvi deposit (Eilu, 2015).

The research area of this study is Kultanummi, located near the city of Salo within the Uusimaa Belt (Figure 4). It has been studied by Geological Survey of Finland (GTK) by early 2000s (e.g. Grönholm et al., 2005; Grönholm & Kärkkäinen, 2006) due to gold prospectivity of the area based on layman samples sent to GTK. The studies concluded by GTK focused mainly on economic potential of the gold mineralization, therefore the relationships of the local geological evolution and formation of the mineralization compared to the surrounding high metamorphic grade Uusimaa Belt remain unresolved. In addition, the deposit type of Kultanummi and the age of gold mineralization remain unresolved.

The aim of this study is to determine the age of fluid activity and gold mineralization of Kultanummi. Secondary objective is to define the genetic type of the deposit. Thin sections were made from the samples collected from Kultanummi for age determination and petrographical purposes. Age determinations were carried out in-situ by U-Pb method on zircons, monazites and rutiles. In addition of these, field observations, thin sections and previous studies were used for defining the possible deposit type for Kultanummi gold mineralization.

2 Geological setting

2.1 Svecofennian orogeny

The Svecofennian orogeny, ca. 1.92 – 1.79 Ga, is a major crust forming event when most of the bedrock in southern and central Finland was formed (Lahtinen et al., 2005). It is one of the two major Paleoproterozoic orogenic stages in Fennoscandia with the Lapland-Kola orogeny which took place ca. 1.94 – 1.86 Ga ago (Daly et al., 2006). In Finland the oldest rocks in the Svecofennian orogen are the 1.93 – 1.92 Ga island arc rocks found in the Savo Belt in central Finland (Lahtinen et al., 2009). The extent of the Svecofennian crust is illustrated in the Figure 1.

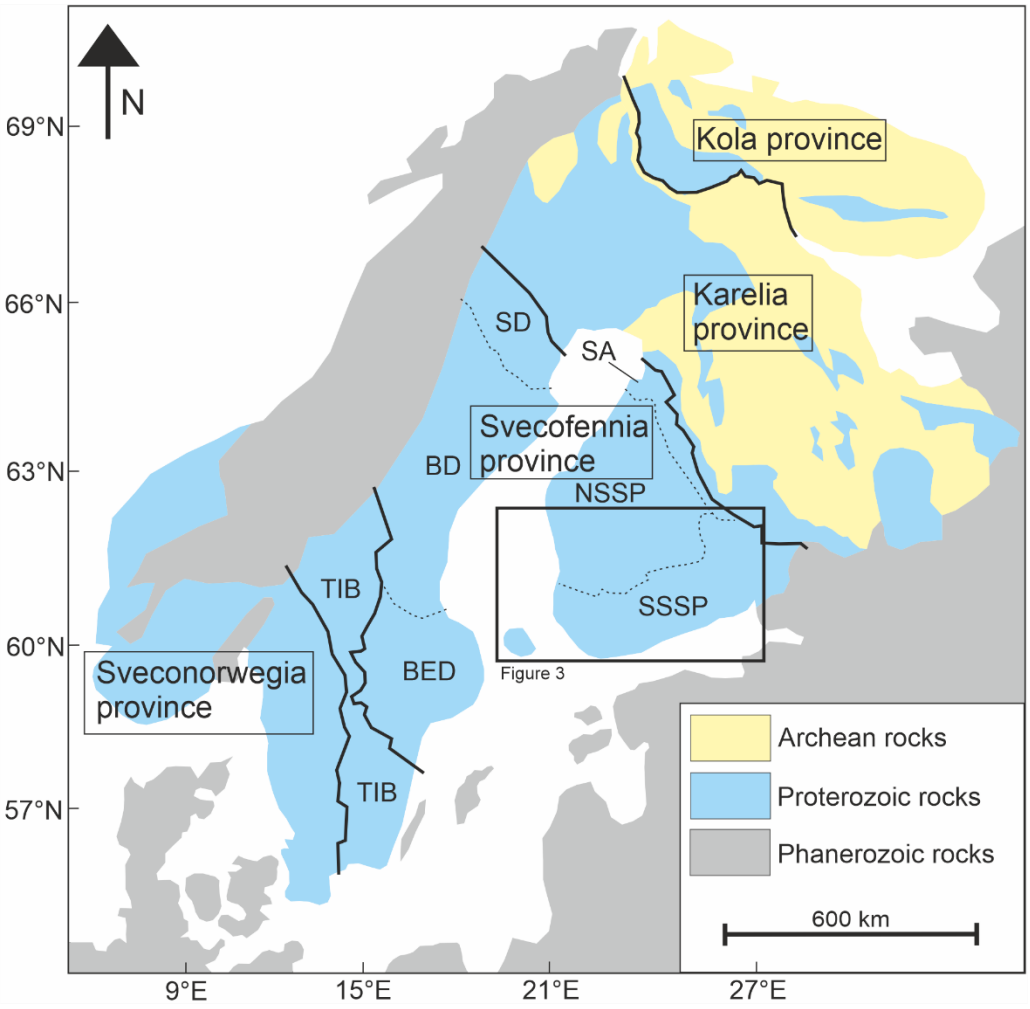

Figure 1. Simplified map of Fennoscandian shied. The black box indicates the location of southern Svecofennia and it is illustrated in Figure 3. The abbreviations are as following: SA = Savo arc; NSSB = Northern Svecofennian Subprovince; SSSP = southern Svecofennian Subprovince; SD = Skellefte district; BD = Bothnian district; BED = Bergslagen district; TIB = Transscandinavian igneous belt. Modified after Vaasjoki et al. (2005).

The onset of the Svecofennian orogeny is interpreted to take place in ca. 1.92 Ga ago (Lahtinen et al., 2009) simultaneously with the Lapland-Kola orogeny. Different models of the tectonic setting/evolution of the Svecofennian orogeny have been proposed by numerous authors. One common model suggests that the orogeny can be characterized by one continuous subduction beneath an active continental margin (Gorbatschev & Bogdanova, 1993; Hermansson et al., 2008). Based on data obtained from central Sweden, Hermansson et al. (2008) suggested a presence of one subduction system where extensional and contractional tectonics changed during the orogeny, which is shown as different age peaks between magmatic phases. In this model the first phase was 1.91 – 1.89 Ga bimodal volcanism, which was characterized by extensional back-arc setting. Subsequently, the direction of plate motions started to change resulting in waning extension between 1.89 – 1.87 Ga. After the waning stage, the subduction hinge advanced and during 1.87 – 1.86 Ga compression was present in back-arc setting. At 1.86 Ga the direction was changed and compression switched into extension.

The second common model of the Svecofennian tectonics is related to collision of several arc complexes/microcontinents into Archean crust (Nironen, 1997). In this model two arc complexes collided between 1.91 – 1.87 Ga with first arc colliding in 1.91 Ga and the second one in 1.89 Ga with sedimentary basin development occurring in between the collisions. The second arc collision was followed by an intracratonic stage at ca. 1.86 Ga and a high-grade metamorphism at 1.84 – 1.82 Ga. During the metamorphic event the thickened crust partially melted and migmatites were formed.

The model by Nironen (1997) has been refined subsequently by multiple arc complexes/microcontinents and collisions in several orogenic stages (Lahtinen et al., 2005; Lahtinen et al., 2009). This tectonic evolution model is presented in the Figure 2. Lahtinen et al. (2005) divided the Svecofennian orogeny into several phases: Lapland-Savo North (ca. 1.92 Ga), Lapland-Savo South (ca. 1.92 – 1.91 Ga), Fennian (1.89 – 1.86 Ga), Svecobaltic (1.83 – 1.79 Ga) and Nordic (1.82 – 1.79 Ga). In the first phase (Lapland-Savo) proposed microcontinents Keitele and Norbotten collided with Karelia province between 1.92 – 1.91 Ga (Lahtinen et al., 2005). This was followed collision of another microcontinent called Bothnia with Norbotten and Keitele at 1.90 Ga, which included a short change of the subduction direction. This resulted in deposition of the rocks of the Tampere Belt (Lahtinen et al., 2005).

After these collisions it is interpreted that a short extensional period took place followed by the change in the subduction polarity from west to north. This resulted in collision between volcanic arcs in south and Keitele microcontinent in north, i.e. Fennian phase (Lahtinen et al., 2005), which continued until 1.87 Ga. Lahtinen et al. (2005) suggested that majority of crust of southern Finland was formed during this orogeny event. The Fennian phase was followed by an extensional period which was related to orogenic collapse caused by the shift of plate movements and the instability of young and hot crust (Lahtinen et al., 2005). The extensional period continued until 1.84 Ga, and it is characterized by migmatisation and granitic magmatism caused by rapid temperature rise in the crust due to asthenosphere upwelling (Lahtinen et al., 2005).

The Svecobaltic phase took place after the extensional period (Lahtinen et al., 2005), which was initiated by the collision of the Sarmatia craton into Fennoscandia from south-east (Lahtinen et al., 2009). This phase in characterized by the change of the extensional system into compression and high grade metamorphism and migmatisation (Patchett & Kouvo, 1986; Suominen, 1991). Complex thrusting and folding occurred, and peak metamorphic conditions were obtained during this period in southern Finland (Väisänen & Hölttä, 1999; Lahtinen et al., 2005). In places the metamorphic grade reached granulite facies conditions (Väisänen et al., 2000).

Simultaneously with Svecobaltic orogeny the Nordic phase took place due to collision between Amazonia and Fennoscandia in the northwest (Lahtinen et al., 2005). Moreover, the Transscandinavian Igneous Belt (TIB) was formed in western Sweden during this period (Gorbatschev and Bogdanova, 1993). The first phase of TIB (TIB 1, 1.81 – 1.77 Ga) might be evidence of magmatism within convergent plate boundary (Gorbatschev & Bogdanova, 1993). This phase is not well represented in southern Finland, and the only evidence might be the 1.80 – 1.79 Ga pegmatites (Alviola et al., 2001).

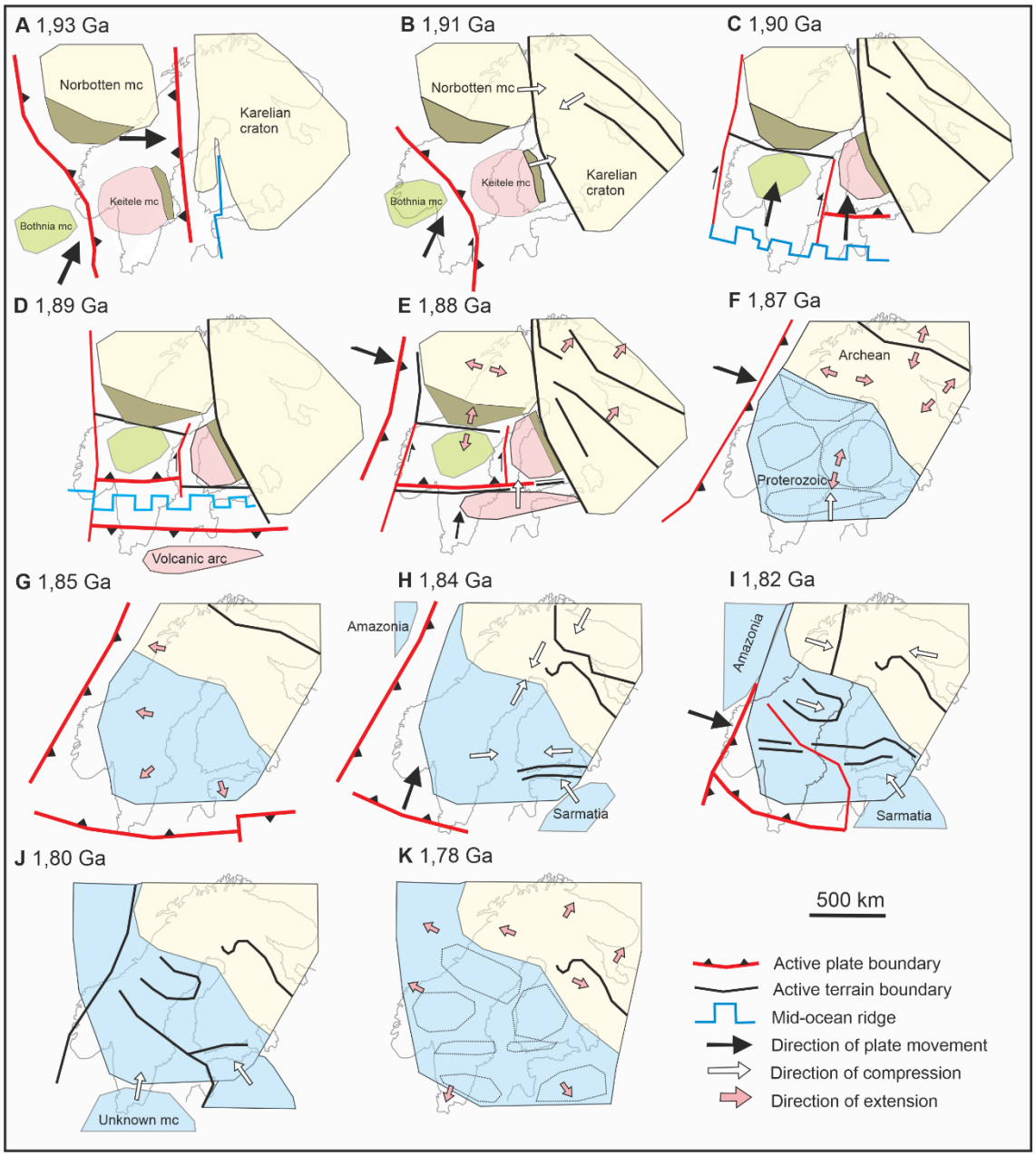

Figure 2. Tectonic model of the Svecofennian orogeny (modified after Lahtinen et al. 2005). A) Keitele and Norbotten subducts towards west under Karelian craton. B) Peak of the Lapland-Savo phase. C) Bothnia microcontinent docks with Norbotten and Keitele. Subduction reversal occurs during this period. D) Subduction direction switches to north under Bothnia and south under volcanic arc. Subduction under Keitele ends. E) Fennian phase peak stage occurs, and volcanic arc collides with Keitele, which results shortening of the crust and reactivation of the Lapland-Savo suture zone. Subduction continues under Bothnia and rifting occurs in Skellefte district. There's also subduction under Norbotten towards east. F) Fennian phase collapse and subduction zone switches to southwards. G) Subduction zones towards southeast and northeast. Hot and unstable crust causes large-scale extension. H) Svecobaltic phase period starts as the Sarmatia collides with Fennoscandia from southeast. Subduction towards northeast and southeast are still active during this period. I) Svecobaltic phase peak event and Nordic phase starts. The collision between Fennoscandia and Sarmatia causes a crustal-scale shear zone that divides Svecobaltic orogen into two different compressional regimes. Amazonia collides with Fennoscandia from the northwest. J) Paleoproterozoic supercontinent forms as Laurentia, Fennoscandia, Amazonia, Sarmatia and an unknown continent combine. K) Stabilization of Fennoscandian shield by the orogenic collapse and lithospheric delamination.

2.2 Geology of the Uusimaa Belt

The Uusimaa Belt is one of the two major volcanic belts in the southern Finland with the Häme Belt (Figure 3). Majority of the Uusimaa Belt consists of metasedimentary rocks (mudstones, greywackes, schists and gneisses), felsic to ultramafic volcanic rocks, granites and migmatites (Kähkönen, 2005). With these some volcanogenic massive sulfide (VMS) deposits and minor banded iron formations (BIF) have been described, which brings up economic interests alongside with gold deposits in the Uusimaa Belt. The metamorphic conditions in the Uusimaa Belt varies from amphibolite to granulite facies (Kähkönen, 2005). For example, in Orijärvi region, the primary structures are well-preserved, and metamorphic conditions are in lower amphibolite facies. This locality played a key role for metamorphic studies since Eskola (1914) introduced the first steps in metamorphic facies classification based on the observations in Orijärvi.

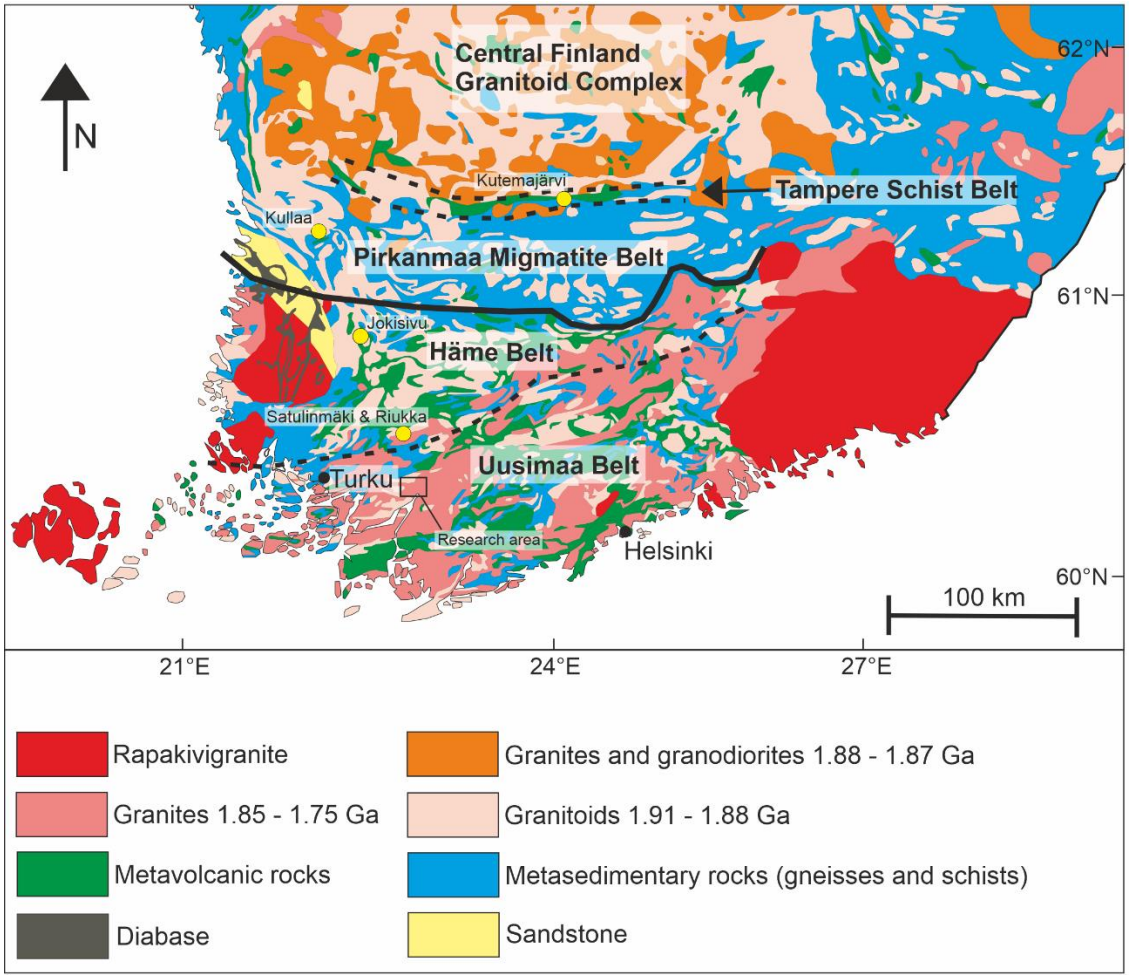

Figure 3. Simplified geological map of southern Finland. Dashed line represents the terrain boundaries and solid line represents the boundary between southern and central Svecofennian. Salo area is highlighted with black box on the map and it is shown in Figure 4. Gold deposits mentioned are also marked on the map. Modified after Koistinen et al. (2001).

The Uusimaa Belt was strongly reworked during the Svecofennian orogeny. Ages of the volcanic rocks vary mainly between 1.90 – 1.88 Ga (e.g., Väisänen & Mänttäri, 2002; Väisänen & Kirkland, 2008). First metamorphic peak (e.g., Väisänen et al., 2002) is defined at 1.87 – 1.86 Ga related to peak collision stage during the Fennian phase (Chapter 2.1). During the collision granitoids were intruded into the crust (Ehlers et al., 1993). Second metamorphic peak took place when the Sarmatia craton collided with Fennoscandia from southeast between 1.84 – 1.82 Ga (Chapter 2.1). This metamorphic peak has been dated around 1.825 Ga in southern Finland (Väisänen et al., 2002). During this period migmatisation, deformation and intrusion of late-orogenic granitoids occurred widely across the southern Finland (Ehlres et al., 1993).

2.3 Geology of Kultanummi area

The study area, Kultanummi, is located near the village of Kytö, about 15 kilometres to northeast from the center of Salo (Figure 4). Interest in Kultanummi area was introduced in 1990s when Geological Survey of Finland received layman samples, which contained anomalous amounts of gold including visible gold grains. The area was studied by GTK in the early 2000s (e.g. Vanhala, 2002; Ruotoistenmäki, 2004; Grönholm et al., 2005; Grönholm & Kärkkäinen, 2006), and one master's thesis has been done from the same area in Åbo Akademi (Wiik, 2004). Mapping, trenching, drilling and geophysical measurements have been conducted at the site (Grönholm & Kärkkäinen, 2006).

Bedrock of Kultanummi area consists mainly of metasedimentary rocks (mica schists/gneisses, quartz-rich sillimanite gneisses and sillimanite-cordierite gneisses), metavolcanic rocks, which are intruded by granites and pegmatites. Principal minerals in mica gneisses are biotite, quartz, plagioclase, K-feldspar, with minor amounts of garnet, zircon, apatite, monazite, xenotime and tourmaline. Both quartz-rich sillimanite gneisses and sillimanite-cordierite gneisses contain rusty, tightly folded quartz veins. These gneisses contain fibrous sillimanite, cordierite, plagioclase, quartz, K-feldspar and biotite. Granitic and pegmatitic dykes contain garnet, magnetite and tourmaline in places. Metamorphic conditions of the area are mainly in upper amphibolite facies, which is typical for southern Finland (Grönholm et al., 2005). Regional structural trend is about E-W direction, and structures tends to be tightly folded (Wiik, 2004).

The gold mineralization in Kultanummi is mainly associated with silicified sillimanite gneisses, and the highest concentrations measured are about 10 ppm in one meter length and 6.5 ppm in 0.7-meter length, the average concentration being 0.3 – 1.8 ppm.

Ore minerals are mainly pyrite and pyrrhotite with minor amounts of arsenopyrite and chalcopyrite (Grönholm & Kärkkäinen, 2006). Hydrothermal alteration is common in Kultanummi area, which is manifested by the increasing sulfide content, sillimanite and cordierite bearing gneisses, silicification, magnetite bearing rocks and also the abundance of rutile in samples (Grönholm et al., 2006).

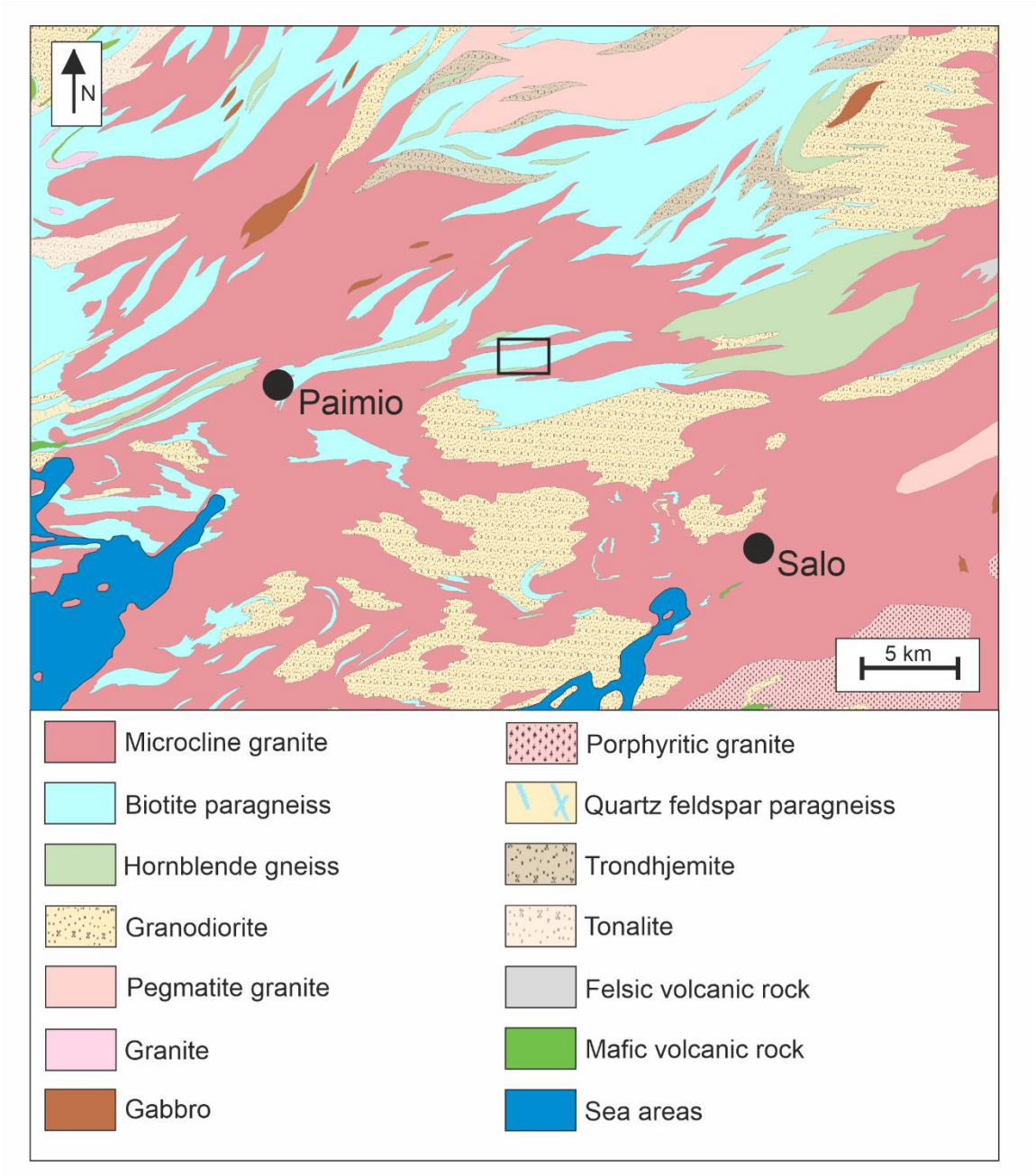

Figure 4. Bedrock map of Salo area. Kultanummi is highlighted with small black box. Map is based on digital bedrock map 1:200 000 produced by Geological Survey of Finland (Bedrock of Finland – DigiKP200). Index for the locality is available in Figure 3.

3 Hydrothermal gold deposits

3.1 Orogenic gold deposits

Throughout the history diverse terminology regarding one coherent gold deposit type has caused discussion and confusion between scientists (Groves et al., 1998). One reason for the broad terminology of gold deposits was the relatively low price of gold before 1970s, which led to disregard of gold studies (Groves et al., 1998). After the price of gold raised up in the 1970s, the number of studies regarding gold deposits increased drastically. During the 1990s term “mesothermal” deposit was widely adopted to describe different but fairly similar gold deposits (Groves et al., 1998). Term “mesothermal” was originally defined by Lindgren (1933), and it described the deposits that formed between 1.2 – 1.6 km depth. This term is not suitable for all the gold deposits because the depth range is more extensive than 1.2 – 1.6 km, so instead of this and because it is said that many of the gold deposits are associated with orogenic processes, the term “orogenic gold” saw the daylight (Groves et al., 1998).

Orogenic gold deposits are hydrothermal deposits formed during orogenic processes in collisional or accretionary settings in convergent plate boundaries (Groves et al., 1998; Goldfarb et al., 2001). They are often associated with low-grade metamorphic terranes, and they are structurally controlled (Groves et al., 1998). As the orogenic gold is described to be a hydrothermal deposit, the hydrothermal alteration is in key role when characterising these types of deposits (Groves et al., 1998). Such mineralization is interpreted to occur during the peak- or post-peak metamorphism (Gebre-Mariam et al., 1995; Groves et al., 1998). Although orogenic gold deposits are usually formed in lower metamorphic conditions, mainly in lower- to mid-greenschist facies, some gold deposits in higher metamorphic conditions have been described (Eilu et al., 1999).

3.1.1 Hydrothermal alteration and carrier fluids for the ore

Orogenic gold deposits usually show strong lateral variations in alteration due to hydrothermal fluid movements through cracks and fractures in bedrock. Mineralogy and the width of alteration zone is dependent on the type of wallrock and the depth of the crust (Eilu et al., 1999). In addition, the mineralogy is also dependent on temperature and pressure (i.e., metamorphic conditions), fluid composition and the amount of fluid compared to wall rock (i.e., fluid/rock ratio) (Reed, 1997). Figure 5 illustrates an alteration scheme of mafic wallrock in greenschist facies conditions.

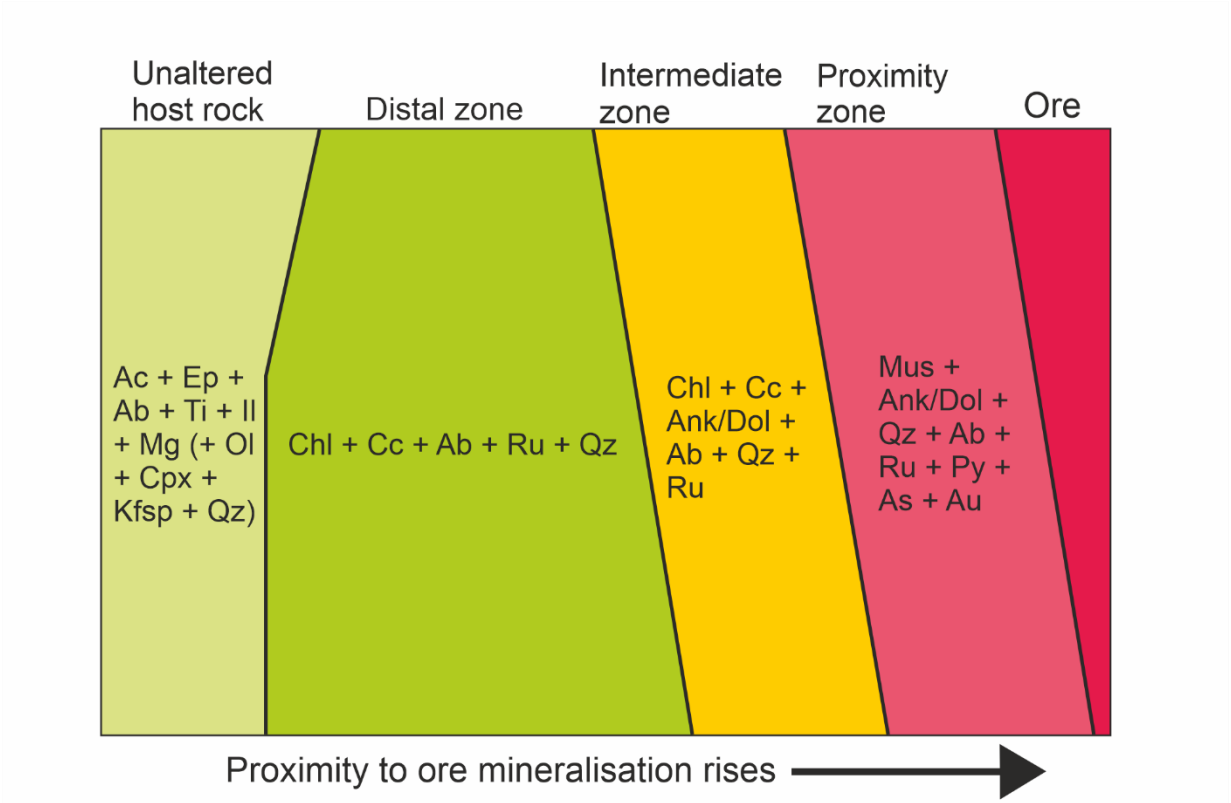

Figure 5. An illustration of wallrock alteration zoning through the interaction of ore fluid where the typical mineralogy in different alteration zones is shown. Wallrock is mafic in composition and P-T conditions are in greenschist facies. Abbreviations are the following: Ac = actinolite; Ep = epidote; Ab = albite; Ti = titanite; Il = ilmenite; Mg = magnetite; Ol = olivine; Cpx = clinopyroxene; Kfsp = K-feldspar; Qz = quarz; Chl = chlorite; Cc = calcite; Ru = rutile; Ank = ankerite; Dol = dolomite; Mus = muscovite; Py = pyrite; As = arsenopyrite; Au = gold. Modified after Eilu et al. (1999).

Orogenic gold deposits are also identified from high-metamorphic terranes (e. g. Barnicoat et al., 1991; Cassidy, 1992; Bloem, 1994), but they are much less common compared to deposits found from lower-metamorphic terranes. These types of deposits are for example Big Bell, Renco, and Griffins Find deposits in Australia (Phillips & Powell, 2009). The alteration scheme in high-metamorphic terranes differs from lower metamorphic terranes; alteration zones are often narrower, and the intermediate zone might be absent (Eilu et al., 1999). According to Eilu et al. (1999) the typical alteration mineralogy in mafic rock in upper amphibolite to lower granulite facies is the following: in **distal zones** the alteration mineralogy is characterized by biotite + plagioclase + hornblende + ilmenite and minor amounts of pyrrhotite and quartz. In granulite facies orthopyroxene and K-feldspar are also present. In **intermediate zones** (if present) the minerology is typically characterized by plagioclase + hornblende + quartz + calcite and ilmenite. In granulite facies orthopyroxene is also present. In **proximal zones** typical

minerology is hornblende + diopside + calcite + biotite + ilmenite + quartz + plagioclase + K-feldspar + tremolite + garnet + titanite + loellingite + arsenopyrite and pyrrhotite. In granulite facies the minerology is typically orthopyroxene + K-feldspar + quartz + diopside + plagioclase + garnet + titanite + loellingite + pyrrhotite and arsenopyrite, the last two being also the common ore minerals.

Ore fluid composition in orogenic gold is typically $H_2O – CO_2 + H_2S \pm CH_4 \pm N_2$ and it is characterized by low salinity and near-neutral pH (Groves et al., 1998). Low salinity is characterized by ≤ 6 wt. % of NaCl and $CO_2 \pm CH_4$ contents between 5 – 30 mol% (McCuaig & Kerrich, 1998). H_2S is suggested to be an important carrier for gold in fluids, and the concentration varies between 0.01 – 0.36 mol% in most gold provinces (Goldfarb & Groves, 2015). Fluid source is interpreted to be metamorphic and/or magmatic (Tomkins, 2013). Several sources of gold have been suggested: metamorphic rocks of which the carrier fluids are generated from, and felsic-intermediate magmas, where fluids are released from as they crystallize (Tomkins, 2013). Moreover, hydrated mafic rock source have been suggested, but for the economically valuable deposit there needs to be a huge volume of rock present because the concentration of gold is often low in such rocks (Phillips & Powell, 2009; Tomkins, 2013).

3.1.2 Structural control of gold deposits

One of the distinct characteristics of orogenic gold deposits is the clear structural control. Faults and fractures in bedrock acts as a path for gold-bearing fluids (Groves et al., 1998). Second or third order structures near large-scale compressional structures like faults and shear zones are common places for gold mineralization precipitation (Groves et al., 1998). These includes structures from ductile to brittle, which are variable in type, for example brittle faults, ductile shear zones, stockwork networks, fault arrays, breccia zones, foliated rocks and fold hinges (Groves et al., 2000). Deposits are typically formed during late orogenic events when shift from compressional to transpressional regime occurs and create suitable pathways for mineralizing fluids (Goldfarb & Groves, 2015).

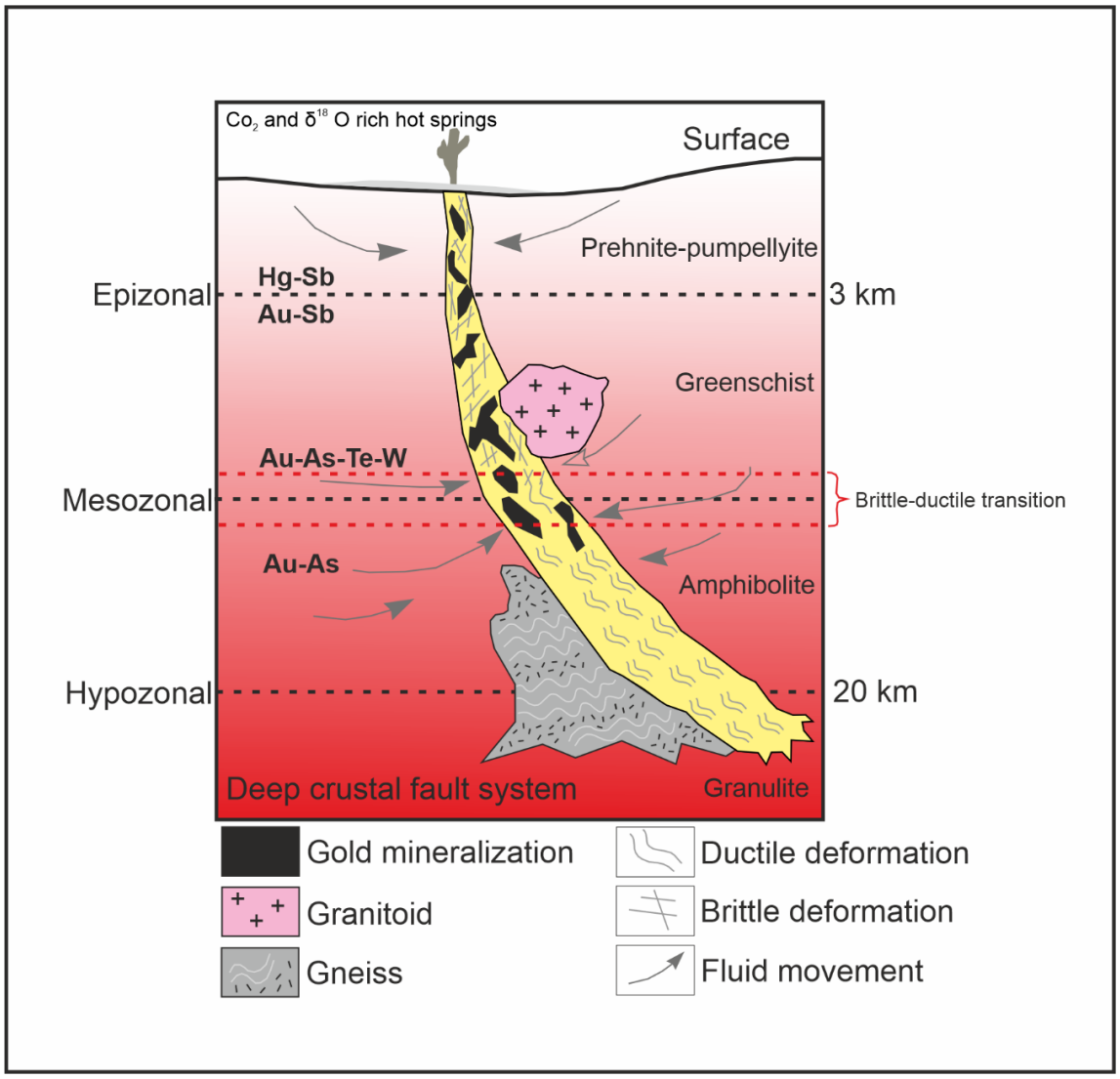

Figure 6. Schematic view of orogenic gold formation in different depths and metamorphic conditions. Modified after Goldfarb & Groves (2015).

3.1.3 Orogenic gold deposits in Finland

In the similar manner globally, in Finland minor effort was focused into the gold exploration due to relatively low price of gold. There was a common consensus in 1980s that Finland lacked the major gold deposits (Eilu, 2015), but after the gold price rise, the exploration of gold and research related to gold deposits increased significantly and many major deposits have been found since then.

Orogenic gold deposits are recognized in both Archean and Proterozoic areas, and the main hosts for these deposits are the greenstone belts formed during Archean and Paleoproterozoic in eastern Finland and Lapland (Eilu et al., 2003). The age of mineralization of the major gold deposits are 2.72 – 2.64 Ga or 2.68 – 2.64 Ga in Archean and 1.91 – 1.77 Ga in Paleoproterozoic (Eilu, 2015). These time intervals can be united with global peaks of orogenic gold mineralizations, which are linked to supercontinent cycle (Groves et al., 2005).

Svecofennian domain in southern Finland contains numerous amounts of orogenic gold deposits with other various genetic types (Eilu et al., 2003; Saalmann et al., 2009). Gold deposits are mainly associated with quartz veins and shear zones aligned in SW – NE to E – W and NW – SE striking zones (Saalmann et al., 2009; Kara et al., 2021). Due to clear structural control in many gold deposits, most of the gold deposits in southern Finland has been classified as orogenic gold deposits (Saalmann et al., 2009). In addition, the evolution of Svecofennian crust shows multiple accretionary events and orogenic phases (Lahtinen et al., 2005), thus providing suitable conditions for orogenic gold formation. In contrast, many gold deposits remain unstudied, and especially their absolute ages and relationships to specific tectonic events are not very well established (Saalmann et al., 2009). Some work has been done to determine these aspects in various gold deposits; for example, the Jokisivu prospect between boundary zone of Häme and Pirkanmaa Belts (Figure 3) have been impacted by several deformation stages and the precipitation of gold took place in late Svecofennian tectonic event at 1.82 – 1.78 Ga (Saalmann et al., 2010). Other gold deposits that have been studied includes for example Satulinmäki and Riukka from Häme Belt (Saalmann et al., 2009).

3.2 Epithermal gold deposits

Another type of hydrothermal gold deposits are epithermal gold deposits. Epithermal gold deposits are typically found in subaerial volcanic arcs at convergent plate margins, and the formation depth is typically under 1.5 km below the surface (John et al., 2018). Like the orogenic gold deposits, epithermal gold deposits can be structurally controlled by faults and fractures in bedrock (John et al., 2018). However, epithermal deposits are often associated with hot springs, mud pools and other types of geothermal systems at the Earth's surface (Taylor, 2007) and are nearly always linked to porphyry deposits (Sillitoe, 2010). In addition of gold, other common metals associated with these deposits are silver (Ag), and sometimes also copper (Cu), zinc (Zn) and lead (Pb). Most of the epithermal gold deposits are young (mostly Paleogene – Quaternary in age), but there are also some Precambrian examples (Taylor, 2007).

3.2.1 Deposit types and hydrothermal alteration

There are two proposed types for epithermal gold deposits: low sulfidation and high sulfidation deposits (Figure 7). The division is based on the sulfidation state of the sulfide minerals (Taylor, 2007). In low sulfidation deposits, the mineralizing fluids are derived from circulation of meteoric water in the crust, which leach out gold and silver from host rock and bond with H_2S in the mineralizing fluid (White & Hedenquist, 1995). They are often associated with geothermal systems at the surface, typically near the volcanoes, but there are also cases that volcanic activity is not present in proximity of geothermal systems (Hedenquist et al., 2000). Fluids are typically low-salinity, near-neutral pH, NaCl-CO_2-H_2S in composition. The conditions are typically reducing in low-sulfidation environments.

In high sulfidation deposits, the mineralizing fluids are derived from magmatic-hydrothermal systems in volcanic environments (White & Hedenquist, 1995). They are characterized by higher temperatures and more acidic fluids compared to low sulfidation deposits (Hedenquist et al., 2000). The conditions are oxidizing, and gold is typically bonded with Cl^- and HS^- complex ions in magmatic fluid. Although the high sulfidation deposits are very different compared to low sulfidation deposits, they can coexist very near to each other (Hedenquist et al., 2000).

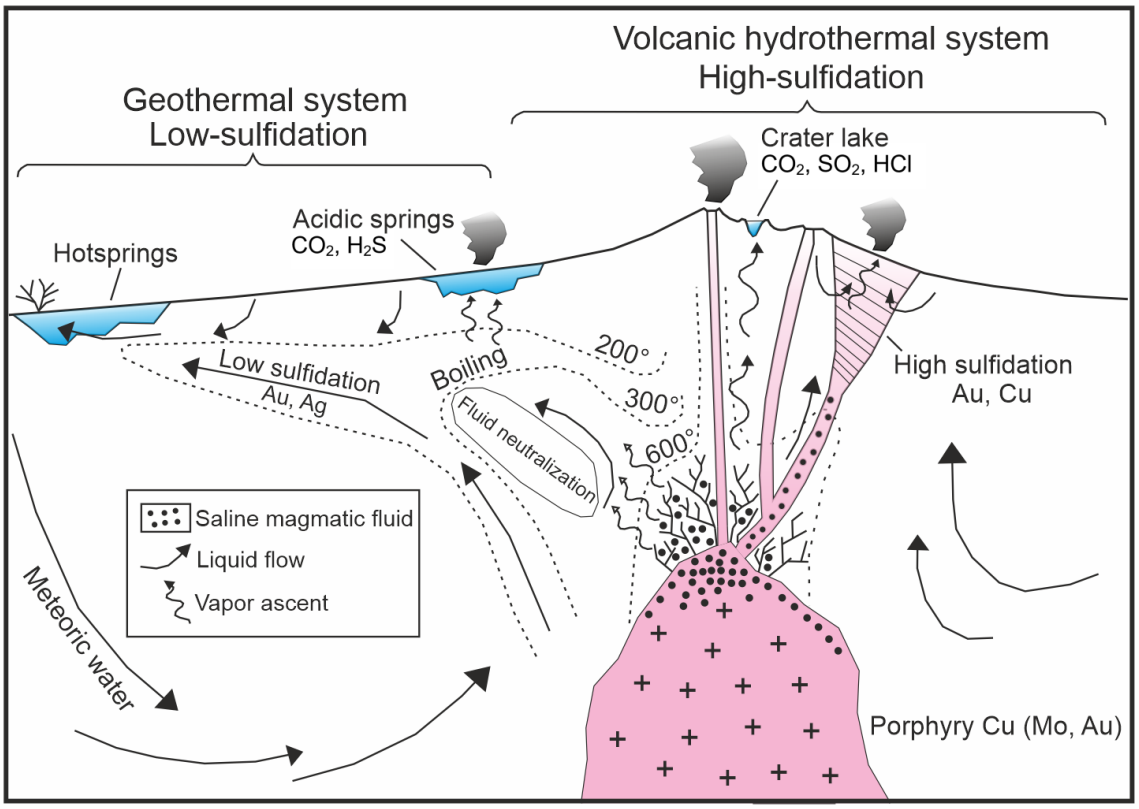

Figure 7. Schematic model of high- and low-sulfidation epithermal deposits. Modified after Hedenquist et al. (2000).

Low- and high-sulfidation deposits are separated by alteration assemblages, which are controlled by multiple factors. The most common alteration schemes for epithermal deposits are shown in the Figure 8.

In high sulfidation deposits (Figure 8A), the host rock for the ore is commonly leached silicic host, often referred to as “vuggy quartz” (Hedenquist et al., 2000). Common alteration minerals around the ore are quartz, alunite, pyrophyllite, kaolinite, illite, montmorillonite and chlorite. In contrast, the host rock for the ore in low sulfidation deposits (Figure 8B) is typically quartz-adularia-carbonate veins and alteration minerals are smectite, sericite, illite, adularia, chlorite, calcite and epidote (Hedenquist et al., 2000).

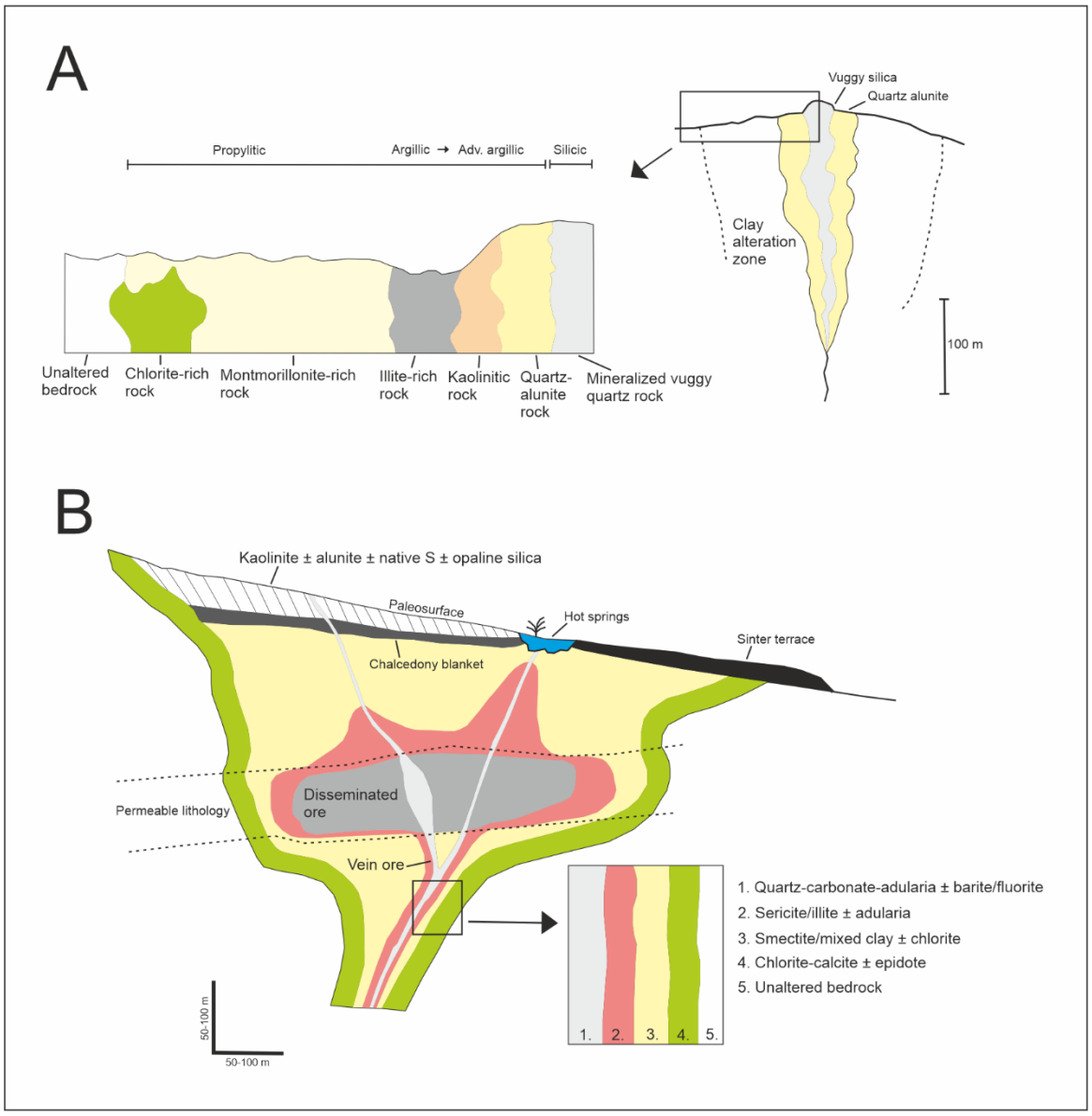

Figure 8. Schematic models for alterations in A) high-sulfidation deposits & B) low-sulfidation deposits. The common structure of these deposits is also well illustrated. Modified after Hedenquist et al. (2000).

3.2.2 Epithermal gold deposits in Finland

Only a few epithermal gold deposits have been described in Finland compared to orogenic gold deposits. The most prominent one is Kutemajärvi deposit in the Tampere Belt (Eilu, 2015). The Tampere Belt is suitable for epithermal deposit formation as it is interpreted to be formed in volcanic arc setting. Other minor epithermal deposits have also been described from Finland, and one of them is possibly Kultanummi minor deposit in Salo (Grönholm & Kärkkäinen, 2006).

4 U-Pb age determination

4.1 Introduction to isotope geology

The basis of U-Pb age determination is in isotope geology, where the key element are the different isotopes of different atoms (Faure & Mensing, 2005). The internal structure of atoms consists of nucleus, which contains protons and neutrons. Protons are positively charged, and neutrons doesn't have electrical charge at all (Faure & Mensing, 2005). The nucleus is surrounded by electron cloud, which contains negatively charged electrons. The total mass of the nucleus, referred as mass number (A), is calculated by a simple equation A = Z + N, where Z is number of protons and N is number of neutrons (Faure & Mensing, 2005). Different isotopes are often presented as a shorthand notation like the following: ${}^{A}_{Z}X$, where A is mass number, Z is number of protons (atomic number) and X is element (for example carbon C or uranium U). For example, uranium-238 can be written as ${}^{238}_{92}U$, as its mass number is 238 and it contains 92 protons. If we want to find out the number of neutrons in uranium-238, we just subtract the number of protons from mass number: 238 – 92 = 146 neutrons.

Chemical elements can have different mass numbers due to different amounts of neutrons in their nucleus. These differences are referred as isotopes, which can be either stable or unstable. If the isotope is unstable, i.e., radioactive, it will lose energy by emission of particles and energy; therefore, isotope is referred as radioactive isotope (Faure & Mensing, 2005). There are four different radioactivity types: α-decay, β^+-decay, β^--decay and electron capture (EC). α-decay requires nuclides that have atomic number of 58 or greater, therefore it is only available for heavier isotopes, but also some light isotopes of helium, lithium and beryllium can decay by α-decay due to their short half-lives. In α-decay parent isotope loses two protons and two neutrons from its nucleus, basically a ${}^{4}_{2}He$ nucleus. In β^+-decay (also known as positron decay) proton inside the nucleus is transformed into a neutron and at the same time positron and electron neutrino are released. In this decay the atomic number Z decreases by one and in the other hand the neutron number N increases by one. In β^--decay (also known as negatron decay) the process of decay is inverted compared to β^+-decay, as the neutron is converted into proton, electron and antineutrino. Therefore, the atomic number Z increases by one and neutron number N decreases by one. Electron capture (EC) decay is a different decaying process as it involves electrons of radioactive nucleus. In this process the nucleus takes electron from its orbiting electron cloud (mainly from the K-shell as it's the closest one to the nucleus) and a proton from the nucleus then converts into neutron and at the same

time the neutrino is emitted from the nucleus. Atomic number Z is decreased by one and neutron number N is increased by one (Faure & Mensing, 2005).

4.2 Basic principles of radioactivity dating

All absolute age determination procedures in geology are based on radioactive decay of radiogenic isotopes. In radioactive decay the unstable parent isotope disintegrates (decays) into daughter isotopes, which is the product of the decay process. Energy is released from the process in the form of ionizing radiation. The daughter isotopes are also often unstable, so they will also disintegrate by radioactive decay and therefore a decay series begins, which continues until a stable daughter isotope is formed (Allègre, 2008). The Curie-Rutherford-Soddy (CRS) law describes that the rate at which nuclei decay is a fixed proportion of the total number of nuclei present, and this remains unaffected by the environmental factors such as temperature, pressure, chemical state, or other conditions (Rutherford & Soddy, 1902; Faure & Mensing, 2005). The equation for this is written as the following:

$$-\frac{dN}{\mathrm{d}t} = \lambda \mathrm{N} \tag{1}$$

where N is the number of nuclei, t is the time and λ is the decay constant. $\frac{dN}{dt}$ represents the rate of change of the amount of parent atoms N in at any time t. Decay constant is the probability of any given nucleus that will decay in certain time interval dt, and each radionuclide has their own decay constant value. When the equation 1 is reworked, we get the following equation:

$$N = N_0 e^{-\lambda t} \tag{2}$$

where N is number of remaining radioactive nuclides and N_0 is the number of radioactive nuclides at the time t_0. Equation 2 can describe all radioactive decay processes (Faure & Mensing, 2005).

One important aspect of radioactive decay is the phenomenon called half-life. It describes the time that given number of radioactive atoms takes to decay so that half of the atoms are left. Decay constant λ and half-life $T_{1/2}$ are related to each other (Faure & Mensing, 2005). When equation 2 is reworked so that t = $T_{1/2}$ and N = $\frac{1}{2}N_0$, we get the following equation for the half-life:

$$T_{1/2} = \frac{ln2}{\lambda} = \frac{0{,}693}{\lambda} \quad (3)$$

Equation 3 therefore shows that the half-life is dependent of the decay constant, which means that because decay constant is different for each radionuclide, each radionuclide has their own half-life. Half-life can vary from seconds to billions of years so it is important to know which system will be chosen for dating purposes, because if the system with short half-life for very old rocks is chosen, results will be unreliable (Allègre, 2008). Sometimes the term mean life τ is used to describe the radioactive decay. It describes the average life expectancy of a radioactive atom and is defined by the following equation:

$$\tau = -\frac{1}{N_0}\int_{t=0}^{t=\infty}(t)dN \quad (4)$$

When equation 4 is reworked, we get the following equation for mean life:

$$\tau = \frac{1}{\lambda} \quad (5)$$

During each mean life the activity of radioactive particle is reduced by factor of 1/e of its initial value. From these two methods the half-life is more used compared to mean life (Faure & Mensing, 2005).

Decaying process continues until all the initial radioactive particles have been decayed into stable daughter isotopes D*. Decaying process of ^{238}U and ^{235}U is demonstrated in the Figure 9. The number of daughter isotopes in certain radioactive system can be determined by following equation:

$$D^* = N_0 - N \quad (6)$$

where N_0 is the number of initial parent particles and N is the number of parent particles in certain time t when decay process has been going on.

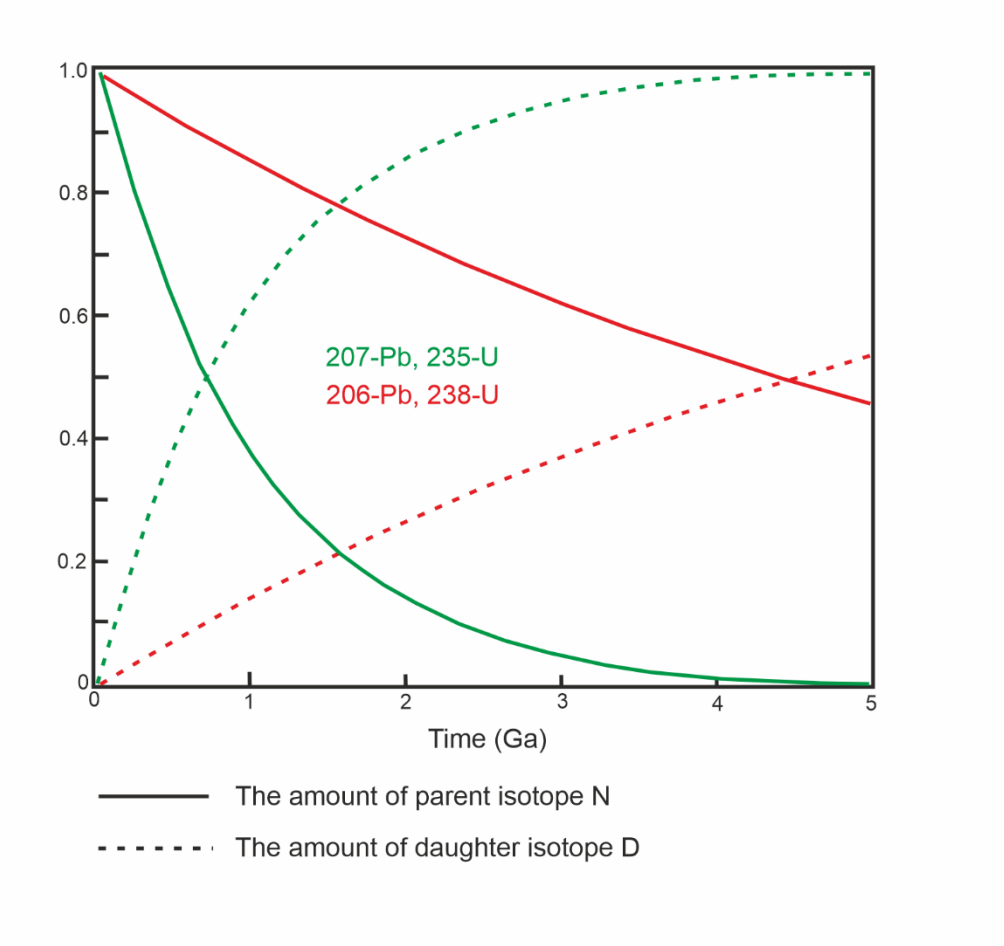

Figure 9. Evolution of two U-Pb systems which shows how the amounts of parent (solid line) and daughter (dashed line) isotopes changes in function of time. Modified after Schoene (2014).

When equation 6 is reworked with equation 2, we get the following equation:

$$D^* = N_0 - N_0 e^{-\lambda t}$$

Which can then be further reworked to the following:

$$D^* = N_0(1 - e^{-\lambda t}) \quad (7)$$

However, for age determination the equation 7 is not suitable because it is not possible to measure the initial number of parent isotopes N_0. Therefore, N_0 in equation 6 needs to be replaced by the following equation:

$$N_0 = Ne^{\lambda t} \tag{8}$$

Which will give us:

$$\begin{aligned} D^* &= Ne^{\lambda t} - N \\ &= N(e^{\lambda t} - 1) \end{aligned} \tag{9}$$

The number of daughter atoms in certain time can be determined by the following equation:

$$D = D_0 + D^* \tag{10}$$

where D_0 is the initial number of daughter atoms. When equation 9 is added to equation 10, we finally get the equation for determining the number of radiogenic daughter isotopes:

$$D = D_0 + N(e^{\lambda t} - 1) \tag{11}$$

From this equation we can also solve t which will give us the time when the mineral which has radiogenic particles was formed:

$$t = \frac{1}{\lambda} \ln\left(\frac{D - D_0}{N} + 1\right) \tag{12}$$

Some assumptions are made for interpretation of the functionality of equation 12. The assumptions are as follows (Faure & Mensing, 2005):

1. The system (rock or mineral that is dated) has remained closed so there hasn't been any addition or reducing in amounts of parent or daughter isotopes. Only way that parent isotope loss is acceptable is the decaying to daughter isotopes. This aspect is particularly complex in sedimentary and metamorphic rocks because sedimentary rocks consist of pre-existing minerals that have been deposited from elsewhere by weathering processes and metamorphic rocks are recrystallised from pre-existing igneous or sedimentary rocks.
2. The decay constant λ is independent of time and is not affected by the prevailing environmental conditions. Its value is known accurately.
3. A suitable value for D_0 is chosen for the calculation, depending on what is known about the chemical characteristics of the daughter element or the isotope composition found in the Earth's reservoir where the rock or mineral formed.
4. The values for D and N that have been measured are accurate and representative for dated rocks or minerals.

4.3 U-Pb dating methods

U-Pb dating methods are the most widely used for the age determinations of Precambrian areas. Uranium (U) has three naturally occurring isotopes which all have different half-lives and decay constants: ^{238}U, ^{235}U and ^{234}U. Relevant information of these isotopes are listed in the Table 1. It is noted that ^{234}U is an intermediate decay product of ^{238}U, which is shown in the Figure 10. Uranium is a common element in e.g. zircon, xenotime, monazite, apatite, titanite and rutile, where it replaces the elements in their crystal lattice (Allègre, 2008). For example, zircon ($ZrSiO_4$) has very high resistance against weathering and its closure temperature is high, so the system stays closed relatively well in various geological processes. These minerals also have low concentrations of initial lead (Pb) which leads to high U/Pb ratio, which is favourable for dating purposes.

Table 1. Abundances, half-lives, decay constants and end-products of naturally occurring uranium isotopes. Data after Faure & Mensing (2005).

Isotope	Abundance (%)	Half-life (a)	Decay constant λ	End decay product
^{238}U	99.2743	4.468×10^{9}	1.55125×10^{-10}	^{206}Pb
^{235}U	0.7200	0.7038×10^{9}	9.8485×10^{-10}	^{207}Pb
^{234}U	0.0055	2.45×10^{5}	2.829×10^{-6}	^{206}Pb

Decaying of ^{235}U and ^{238}U isotopes are shown in the Figure 10. In both systems the end-products are stable isotopes of lead (^{207}Pb and ^{206}Pb). Both have multiple stages of intermediate daughter isotopes; ^{238}U decays to ^{206}Pb by 8 α and 6 β^- emissions, and ^{235}U decays to ^{207}Pb by 7 α and 4 β^- emissions (Allègre, 2008). This is the most distinctive character of U-Pb systems compared to other systems as the daughter isotopes themselves are also radioactive (Dickin, 2018). Because the half-lives of the parent isotopes ^{235}U and ^{238}U are much longer compared to their intermediate daughter isotopes, the U-Pb system reaches a point of secular equilibrium, in which the number of intermediate daughter particles is constant. If the system in which the decay process occurs has remained closed and the secular equilibrium has been reached, the rates of parent isotope decaying and the daughter isotope producing are equal. Therefore, the whole U-Pb system can be treated as if the parent isotope has been decayed into daughter isotope straight away like in the simple parent-daughter system (Faure & Mensing, 2005).

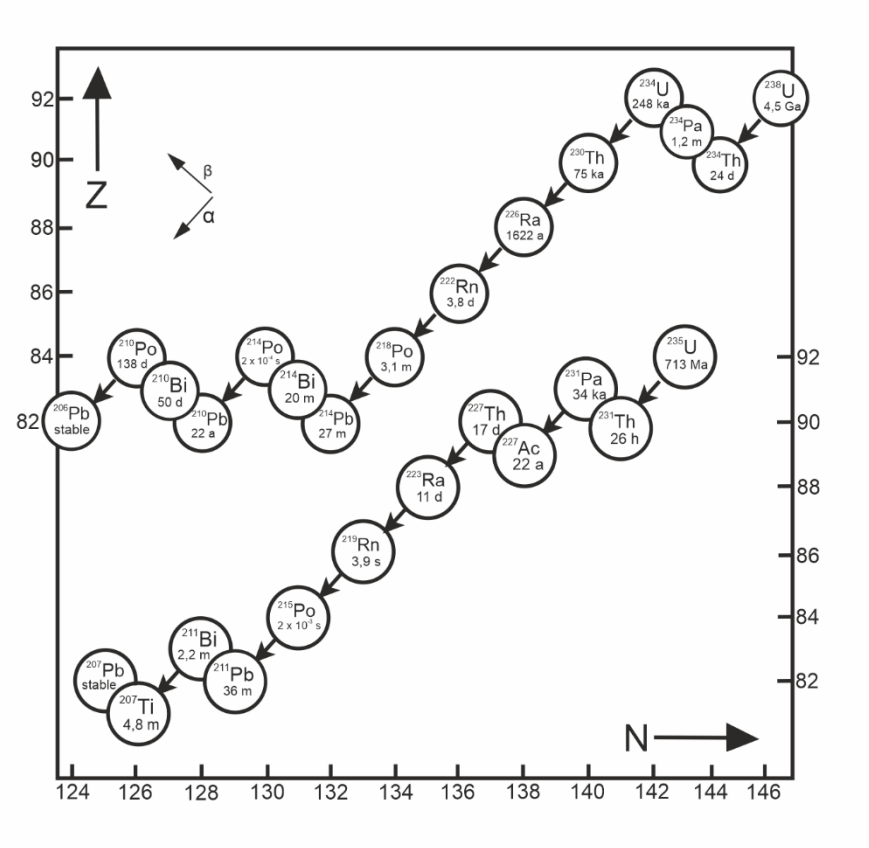

Figure 10. The decay chains for ^{238}U and ^{235}U. Parent and intermediate daughter isotopes are present with their half-lives. Modified after Allègre (2008).

4.4 Interpretation of U-Pb data

The distinct characteristic of U-Pb system compared to other systems is having the two separate geochronometers ($^{206}Pb/^{238}U$ and $^{207}Pb/^{235}U$), which makes the interpretation of age data the most reliable and robust of all dating methods. The accumulation of daughter Pb isotopes from radioactive decay of ^{238}U and ^{235}U can be described when the law of radioactive decay is used from equation 11. The equation for both U isotopes are as followings:

$$\frac{^{206}Pb}{^{204}Pb} = \left(\frac{^{206}Pb}{^{204}Pb}\right)_i + \frac{^{238}U}{^{204}Pb}\left(e^{\lambda_{238}t} - 1\right) \tag{13}$$

$$\frac{^{207}Pb}{^{204}Pb} = \left(\frac{^{207}Pb}{^{204}Pb}\right)_i + \frac{^{235}U}{^{204}Pb}\left(e^{\lambda_{235}t} - 1\right) \tag{14}$$

In these equations the ^{204}Pb is used because it's the only stable non-radiogenic isotope of Pb. When interpretation of U-Pb data is done, several assumptions must be made (Faure & Mensing, 2005):

1. Mineral system has remained closed
2. Correct initial Pb ratios have been used
3. Decay constants for ^{238}U and ^{235}U are known accurately
4. Composition of U is normal ($^{238}U/^{235}U$ = 137.88) and hasn't been affected by isotope fractionation or by the natural chain reaction of induced fission of ^{235}U
5. All results are accurate and error free

When the dating results satisfy these assumptions, the derived ages should be the same, in other words concordant. This is not the case in most of the time, because the loss of U and Pb often occurs because of the opening of closed system, which is a common phenomenon in geological processes. Especially the Pb loss can be a problem when interpreting U-Pb data; this is the case especially in younger rocks and if the rocks have low U/Pb ratio (Faure & Mensing, 2005). The problem of Pb loss can be minimized when the date is calculated based on $^{207}Pb/^{206}Pb$ ratio by combining the equations 13 and 14:

$$\left(\frac{^{207}Pb}{^{206}Pb}\right)^{*} = \frac{^{207}Pb/^{204}Pb - (^{207}Pb/^{204}Pb)_i}{^{206}Pb/^{204}Pb - (^{206}Pb/^{204}Pb)_i} = \frac{^{235}U}{^{238}U}\left(\frac{e^{\lambda_{235}t} - 1}{e^{\lambda_{238}t} - 1}\right) \qquad (15)$$

It can be seen from this equation that the concentration of U isotopes is not necessary for calculating the $^{207}Pb/^{206}Pb$ ratio. $^{235}U/^{238}U$ ratio is constant and its value is 1/137.88.

Several graphical methods for interpreting the U-Pb data have been developed. The methods are as followings: Wetherill's concordia diagram, Tera-Wasserburg diagram and U-Pb isochron diagram. The visualization of these methods is summarized in Figure 11.

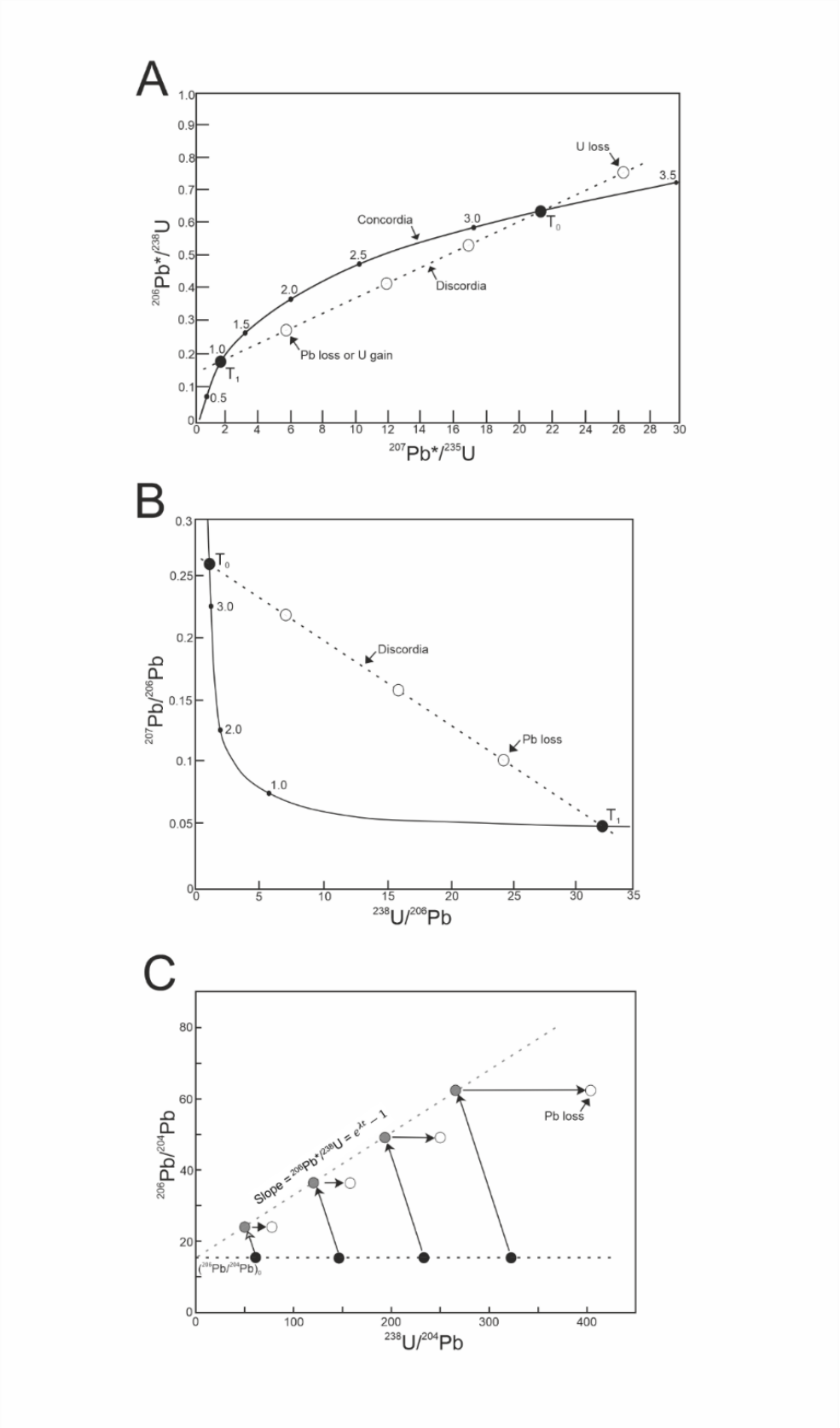

Figure 11. Three U-Pb dating methods: A) Wetherill's diagram, B) Tera-Wasserburg diagram, and C) U-Pb isochron diagram. Modified after Faure & Mensing (2005) and Schoene (2014).

The most used method to visualize the U-Pb ages is the **concordia method** (Figure 11A) first developed by Wetherill (1956). In this method, the two U-Pb systems $^{206}Pb/^{238}U$ and $^{207}Pb/^{235}U$ are paired and shown in the same diagram where y = $(e^{\lambda_{238}t} - 1)$ and x = $(e^{\lambda_{238}t} - 1)$. The samples/analyses that haven't been affected by the lead loss will fall on the concordia curve and thus they are called concordant samples. Location on the concordia curve will show the age that has passed since the system closure (Schoene, 2014).

If the lead loss occurs in the system, the samples will fall out of the curve, and they are called discordant samples. Lead loss can occur for example in metamorphic events where rising P-T conditions leads to the system opening (Faure & Mensing, 2005). As the time passes, more and more lead loss will occur and the samples will arrange themselves linearly in the same concordia diagram (Figure 11A), and therefore discordia line can be drawn from discordant samples. Discordia line will intersect with concordia curve in two points, T_0 and T_1, therefore granting two different ages. From these two T_1 is not taken account when age determination is done because the interpretation of T_1 can be challenging, so only T_0 is taken account; this method is called the **upper intercept method** (Tilton, 1960). In this method T_0 represents the initial formation of studied system.

Other methods have also been developed of which the most popular is the diagram by Tera & Wasserburg (1972) known as **Tera-Wasserburg diagram** (Figure 11B). This method doesn't require knowledge of initial ratios of $^{206}Pb/^{204}Pb$ and $^{207}Pb/^{204}Pb$ but alternatively uses ratios of $^{238}U/^{206}Pb$ on the x-axis and $^{207}Pb/^{206}Pb$ on the y-axis. Tera & Wasserburg (1972) calculated the values for x- and y-coordinates which are the following: $x = \frac{1}{e^{\lambda_{238}t}-1}$ and $y = \frac{1}{137.88}\left(\frac{e^{\lambda_{235}t}-1}{e^{\lambda_{238}t}-1}\right)$. These values form the concordia curve for the diagram. In the similar manner compared to Wetherill's concordia (Figure 11A) the occurrence of lead loss forms discordia curve which intercepts the concordia curve in two spots T_0 and T_1. This method is suitable for samples which contains high amounts of initial Pb (Schoene, 2014).

Traditional **isochron methods** can also be used for U-Pb systems (Figure 11C). These are successfully derived especially in systems where U haven't been lost in geological processes like weathering (Faure & Mensing, 2005). In the Figure 11C the $^{238}U/^{206}Pb$ is shown as an example, but the same procedure can also be used for $^{235}U/^{207}Pb$ system as well. In this system ^{204}Pb is regarded as a stable isotope and the amount of ^{206}Pb increases relative to amount of ^{204}Pb as time goes by, leading to increasing of the slope

of isochron. X-axis contains $^{238}U/^{204}Pb$ and y-axis $^{206}Pb/^{204}Pb$ and the slope is $e^{\lambda_{238}t} - 1$, derived from equation 13. From this slope the age can be determined. For systems that have suffered U-loss, the **Pb-Pb isochron** can be used (Schoene, 2014). Pb-Pb isochron derives the slope from the Equation 15, and in similar manner than U-Pb isochron, the age can be derived from the slope.

4.5 U-Pb geochronometry of zircon, monazite and rutile

The mineral system being studied should have remained closed so that no loss of parent and/or daughter isotopes has occurred. This is rare in nature because uranium is very mobile element and therefore often lost during weathering processes (Faure & Mensing, 2005). In addition, although uranium is a common element in many minerals, only a few of them are suitable for age determinations. Mineral should also be as resistant as possible for weathering and metamorphism, and they should be widely distributed in rocks. Minerals that come along with these terms are for example zircon, monazite and rutile (Faure & Mensing, 2005).

Majority of the age determinations are carried by the analysis of zircons ($ZrSiO_4$). It is a common accessory mineral in both igneous and metamorphic rocks, and also in sedimentary rocks as detrital grains (Hoskin & Schaltegger, 2003). Its ability to survive in variety of magmatic, metamorphic and erosional processes and the ability to host enough high amounts of uranium for age determination purposes makes it suitable for age determination purposes (Corfu et al., 2003). Zircon is tetragonal and its structure is a chain of alternating edge sharing SiO_4 tetrahedra and ZrO_8 triangular dodecahedra (Robinson et al., 1971). Crystal structure is similar with minerals like scheelite ($CaWO_4$), monazite [LREE(PO_4)], rutile (TiO_2), garnet ($X_3Y_2T_3O_{12}$), and anhydrite ($CaSO_4$). The crystal structure is relatively open with voids between SiO_4 and ZrO_8, which allows impurities (other elements) to substitute Zr-ions in the crystal lattice (Finch & Hanchar, 2003).

Distinct characteristics of zircons are zoning structures of different ages which are caused by magmatic and/or metamorphic processes. They can typically be identified with CL and BSE imaging (Corfu et al., 2003). With these methods it is possible to see preserved magmatic cores (which were formed first time when zircons were crystallised), recrystallisation zones and metamorphic rims. There are wide variety of textures for metamorphic zircons mainly because of the wide range of P-T conditions zircons can grow under (Hoskin & Schaltegger, 2003). In high grade metamorphic rocks zircons often

show wide variety and complexity of different textures, and in some cases the magmatic cores are very well preserved but sometimes they can be very highly altered (Corfu et al., 2003). Metamorphic processes can often lead to the opening of the crystal lattice of zircon and therefore lead loss can occur. Another process that leads to the damaging of crystal lattice is the internal radiation damage caused by decaying of radioactive isotopes of uranium and thorium, the elements that are often abundant in zircon (Weber et al., 1994). This radiation damage will make the crystal structure amorphous; in other words the crystal structure won't be as organized as it was before the process. This whole process is called metamictization (Balan et al., 2001).

Monazite [LREE(PO_4)] is an anhydrous phosphate mineral containing cerium (Ce) group of rare earth elements (REE) and it is also one of the most common REE-bearing minerals (Ni et al., 1995). It occurs widely as accessory mineral in medium- to high-grade metasedimentary rocks (especially in pelitic gneisses and migmatites) and in magmatic rocks like diorite, granite and pegmatite (Overstreet, 1967). The structure of monazite is monoclinic, and it is composed of chain of alternating PO_4 tetrahedra and $LREEO_9$ polyhedra (Ni et al., 1995). Monazite is not as resistant against weathering compared to zircon, but it can still be found as detrital grains in metasedimentary rocks. Similarly to zircons, uranium and thorium may replace REE-elements in monazites crystal lattice, which makes it suitable for age determination studies (Overstreet, 1967; Parrish, 1990).

Similarly to zircon, monazite often contains zoning structures of different ages due to metamorphic and/or magmatic processes. Zonation types can be divided into concentric, patchy, and intergrowth-like types. Zonation can be formed in various ways, for example regrowth, recrystallization, replacement, intergrowth and overgrowth (Zhu & O'Nions, 1999). Different zonation patterns may form in wide variety of metamorphic timings from prograde to peak metamorphism all the way to retrograde metamorphism (Ayers et al., 1999). Monazite may also be affected by hydrothermal fluids and that might be able to notice from different zones in monazite grains (Poitrasson et al., 1996).

Because monazite can host radioactive isotopes of uranium and thorium like zircon, monazite can also suffer from radiation damage caused by decaying of these radiogenic isotopes. Compared to zircon, monazites crystal structure tends to amorphise at much lower temperatures of about 175 °C, whereas amorphization temperature of zircon is about 740 °C (Meldrum et al., 1998). Even though the amorphization temperature of monazite is lower, the structure of monazite recovers through annealing process better compared to zircon and therefore it is more resistant against radiation damage compared to zircon, and metamictic monazites are rare in nature. This also means that monazite

doesn't suffer from lead loss as much as zircon (Meldrum et al., 1998). What is problematic in monazite related to age determination purposes are its high amounts of thorium as the initial ^{230}Th causes the excess of ^{206}Pb, causing the negative $^{207}Pb/^{206}Pb$ and therefore causing the results to plot above the concordia curve (Schärer, 1984). Therefore, these results should be corrected for obtaining reliable results.

Rutile (TiO_2) is a titanium bearing oxide mineral and the most common natural form of TiO_2. It can be found from various types of rocks ranging from metamorphic, igneous and sedimentary rocks and from hydrothermal systems (Zack & Kooijman, 2017), although it tends to be absent from various important rock types, like granites, felsic gneisses and low-grade metamorphic rocks. In contrast, rutile is common mineral in high-grade metamorphic rocks and high-pressure mafic rocks (Zack et al., 2004b). Crystal structure of rutile is tetragonal. In the unit cell of rutile each titanium ion (in form of Ti^{4+}) is surrounded by six oxygen ions (in form of O^{2-}) and they are chained by the way that each oxygen ion is surrounded by three titanium ions (Meinhold, 2010). There are various elements that can substitute titanium in rutiles crystal lattice, for example chromium (Cr), hafnium (Hf), iron (Fe), niobium (Nb) and uranium (U).

The presence of uranium makes it possible to use rutile for age determination purposes (Meinhold, 2010). Typically, rutile does not contain as high amounts of uranium compared to zircon, but sometimes the amounts of uranium can be enough for U-Pb and Pb-Pb dating (Mezger et al., 1989). There are some advantages on age determination of rutile; for example, rutile is more resistant against resetting of Pb values compared to zircon (Vry & Baker, 2006), and the rather low closure temperature of rutile makes it suitable for being able to record hydrothermal processes (Meinhold, 2010). In other hand, disadvantages of rutile compared to zircon are mainly related to its lower amount of U in crystal lattice and the absence of suitable rutile standard grains for age determination purposes compared to zircon (Luvizotto et al., 2009b). Cooling temperature of rutile (about 500 °C) is also much lower compared to zircon and monazite, and therefore in some cases the ages determined from rutile grains can be significantly younger compared to zircon (Chreniak, 2000). These younger ages can resemble hydrothermal activity related to slow cooling after peak metamorphism in similar way with monazite. In similar way with zircon and monazite, rutile grains can have distinct zoning structures related to its crystallization age and metamorphic history, especially in larger rutile grains (Zack & Kooijman, 2017).

4.6 Age determination with LA-ICP-MS

A big step in isotopic studies was achieved in the beginning of 20th century when mass spectrometers were invented. Mass spectrometer can be defined as a device that uses magnetic field to separate charged particles (atoms and molecules) based on their masses. First mass spectrometer was developed at the Cavendish Laboratory of the University of Cambridge by J. J. Thompson, and it was first used to proof that neon (Ne) has two different isotopes with different masses $^{20}_{10}Ne$ and $^{22}_{10}Ne$ (Faure & Mensing, 2005). Modern mass spectrometers are based on the design of Alfred Nier developed in 1940 (Nier, 1940; Griffiths, 2008). This type of mass spectrometer is composed of three important parts: an ion beam source, a magnetic analyser and an ion collector (Figure 12).

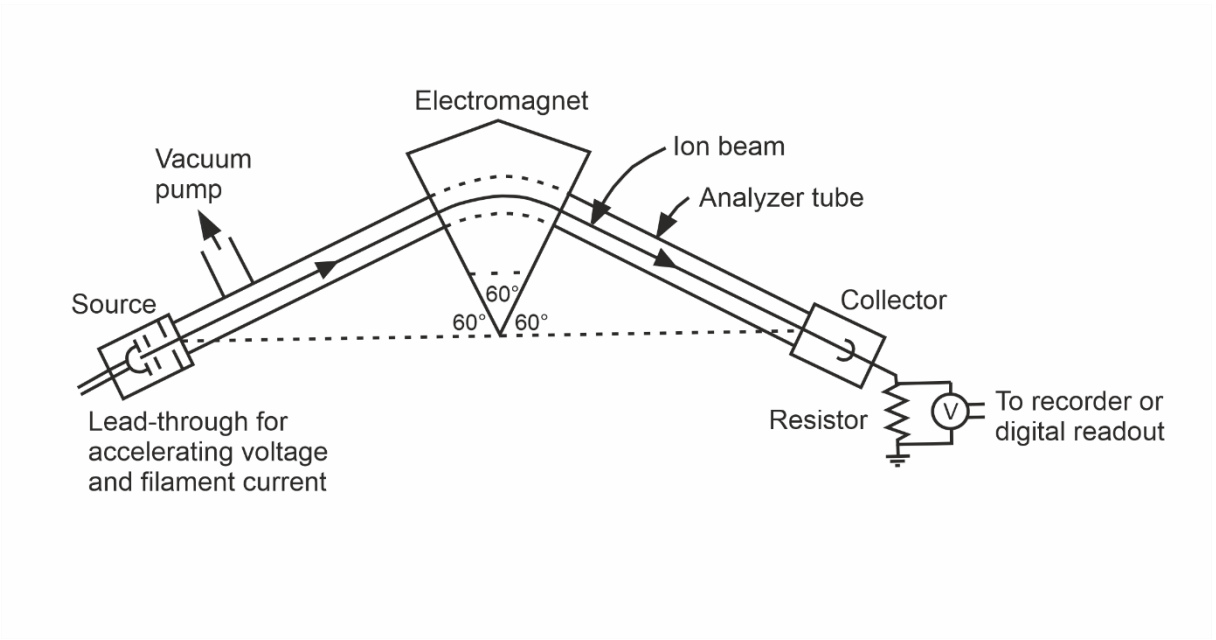

Figure 12. Schematic diagram of Nier type mass spectrometer. Modified after Faure & Mensing (2005).

The functions of different parts of mass spectrometer are explained according to Faure & Mensing (2005) and Allègre (2008). The ion beam source ionizes atoms from the sample by electron bombardment and accelerates them. After the acceleration, the ions enter the magnetic analyser. In the analyser the ions are separated based on their masses. The principle of this is that the ions with different masses have different traveling paths which can then be detected by measuring instruments. After the magnetic analyzer the ions travel further to the ion collector. Collector is a metal cup (for example a Faraday

cup) that collects the charged ions. When the ions are collected, they are converted into a current that is further conducted through a resistor. The potential differences generated in the resistor are then analysed and measured and with them the data is obtained.

Different types of mass spectrometers have been developed throughout the years, and one of them is the laser ablated inductively coupled plasma mass spectrometer (LA-ICP-MS). Schematic picture of this kind of mass spectrometer is shown in the Figure 13. Developed in 1970s, the ICP-MS uses argon plasma torch for ionizing the sample. The usage of plasma, which temperature can be as high as 10 000 K, is able to completely ionize elements that are otherwise hard to ionize, like hafnium and thorium (Allègre, 2008; Dickin, 2018). Laser ablation (LA) is used for removing atoms from solid mineral grains which are then transported into plasma. In the plasma the atoms are then ionized and carried out to plasma spectrometry through magnetic field and the collected into detector for analysis (Allègre, 2008). There have been some delays with adapting LA-ICP-MS because of problem related to different elements mass fractionations which requires the usage of standards for different minerals like zircon and monazite (Hirata & Nesbitt, 1995; Horn et al., 2000). However, the LA-ICP-MS is a productive tool for age determination purposes because the sensitivity of elemental determination is very good (Faure & Mensing, 2005).

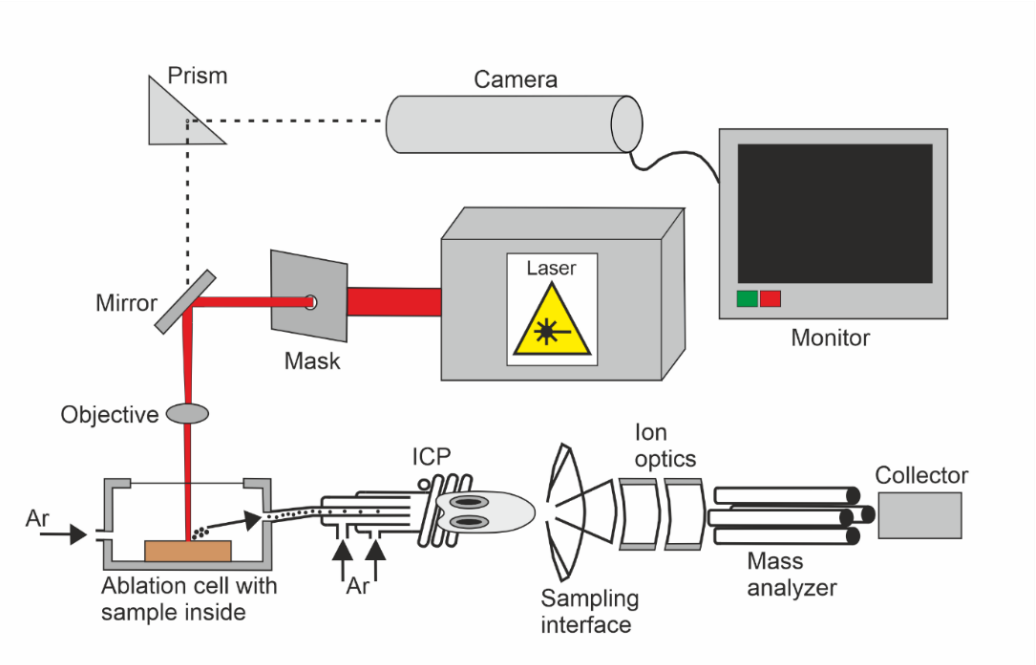

Figure 13. Schematic model of LA-ICP-MS. Modified after Ghent University 2025.

5 Materials and methods

5.1 Field work and sampling

Field work was executed during spring 2024 in Kultanummi area near the town of Salo (Figure 14). One day was also executed during September 2024 for photography purposes. The samples were collected from interesting localities regarding the structures, mineralization and alteration. The tools used for sampling were geological hammer and additionally samples were collected also with minidrill. A total of 13 oriented samples were collected and of those seven were collected by the drill. Structural measurements were also taken from the outcrops with Breithaupt compass.

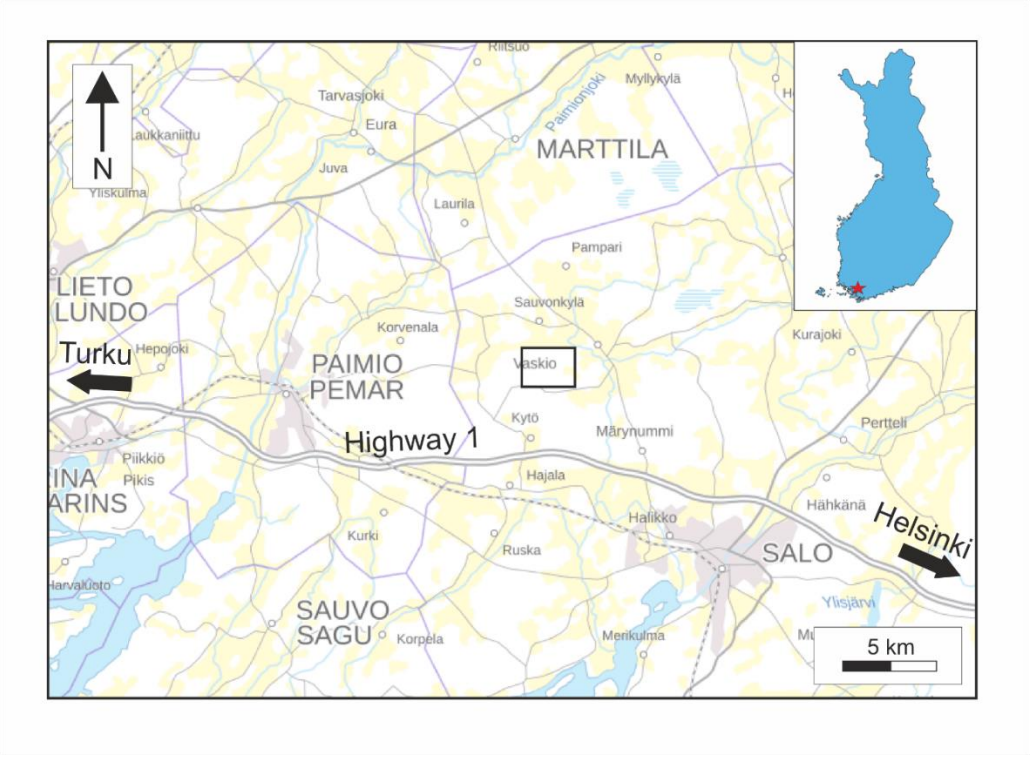

Figure 14. Basemap of the Salo area. Kultanummi is highlighted with the black box.

5.2 Thin sections

The samples were stored and cut in the laboratory at Geohouse at University of Turku. After the treatment, thin sections were made from the selected samples at Geohouse by laboratory technician Arto Peltola. A total of 18 thin sections were made of which seven were chosen for polishing. Decisions were made based on the mineralogy and microstructures. Orientation of thin section were preserved, and sections were cut so that examined surface is perpendicular to the foliation and parallel to the lineation.

5.3 SEM analysis

SEM (Scanning Electron Microscope) was used to find suitable minerals from thin sections for age determination purposes. SEM used for this study was located at Espoo laboratory in Geological Survey of Finland (GTK). Analyses were done by PhD Jaakko Kara and present author on September 2024 with guidance from PhD Paavo Nikkola from GTK. BSE (Back-Scattered Electron) images were further handled with Aztec software (version 6.1) by Oxford Instruments at Geohouse to find and identify the suitable minerals, to study their texture, mineral assemblage and structural setting from thin sections.

5.4 LA-ICP-MS analysis

Age determination analysis were performed by LA-ICP-MS at Espoo lab in GTK during December 2024. Analyses were done by PhD Jaakko Kara and present author with guidance from PhD Matti Kurhila from GTK. Following setting for ablation were used for zircon and monazite: beam diameter: 25 µm (zircon) and 20 µm (monazite); pulse frequency: 5 Hz; argon flow of 0.95 l/min and for rutiles: beam diameter 35 µm; energy: 31.7 % of 5 mJ; beam energy density: 1.72 J/cm^2, argon flow 1.00l/min; 5-shot preablation was used for each U-Pb measurement. Three calibration standards were used for zircons and monazites and two for rutiles. They are as following: for zircons standards GJ-1 (609 ± 1 Ma; Belousova et al., 2005), an in-house standard A382 (1876 ± 2 Ma; Huhma et al., 2012), and an in-house standard A1772 (2712 ± 1 Ma; Huhma et al., 2012); for monazites standards TS (910.4 ± 0.34 Ma; Budzyń et al., 2021), an in-house standard A49 (1874 ± 3 Ma) and an in-house standard A1326 (2635 ± 2 Ma, Hölttä et al., 2000); for rutiles standards R10 (1090 ± 5 Ma; Luvizotto et al., 2009) and R632 (496 ± 2 Ma; Axelsson et al., 2018). Standards were analysed at the beginning and end of the whole set and also at regular intervals during the session. Raw data was collected and monitored on-line with Glitter program (Van Achterbergh et al., 2001) and the final data reduction was done with U-Th-Pb Saturn 2.0 software (Iana & Figueiredo, 2023). Excel extension Isoplot 4.15 (Ludwig, 2003) was used for calculating and plotting the data.

6 Results

6.1 Lithology and petrography of the Kultanummi area

Rocks in the study area are mainly composed of metasedimentary rocks (Figure 15). With these some granitic rocks and pegmatites are also observed. Pegmatite veins are scattered around the area, and they are cutting the metasedimentary outcrops. Granitic rocks are mostly situated at the northernmost part of the area.

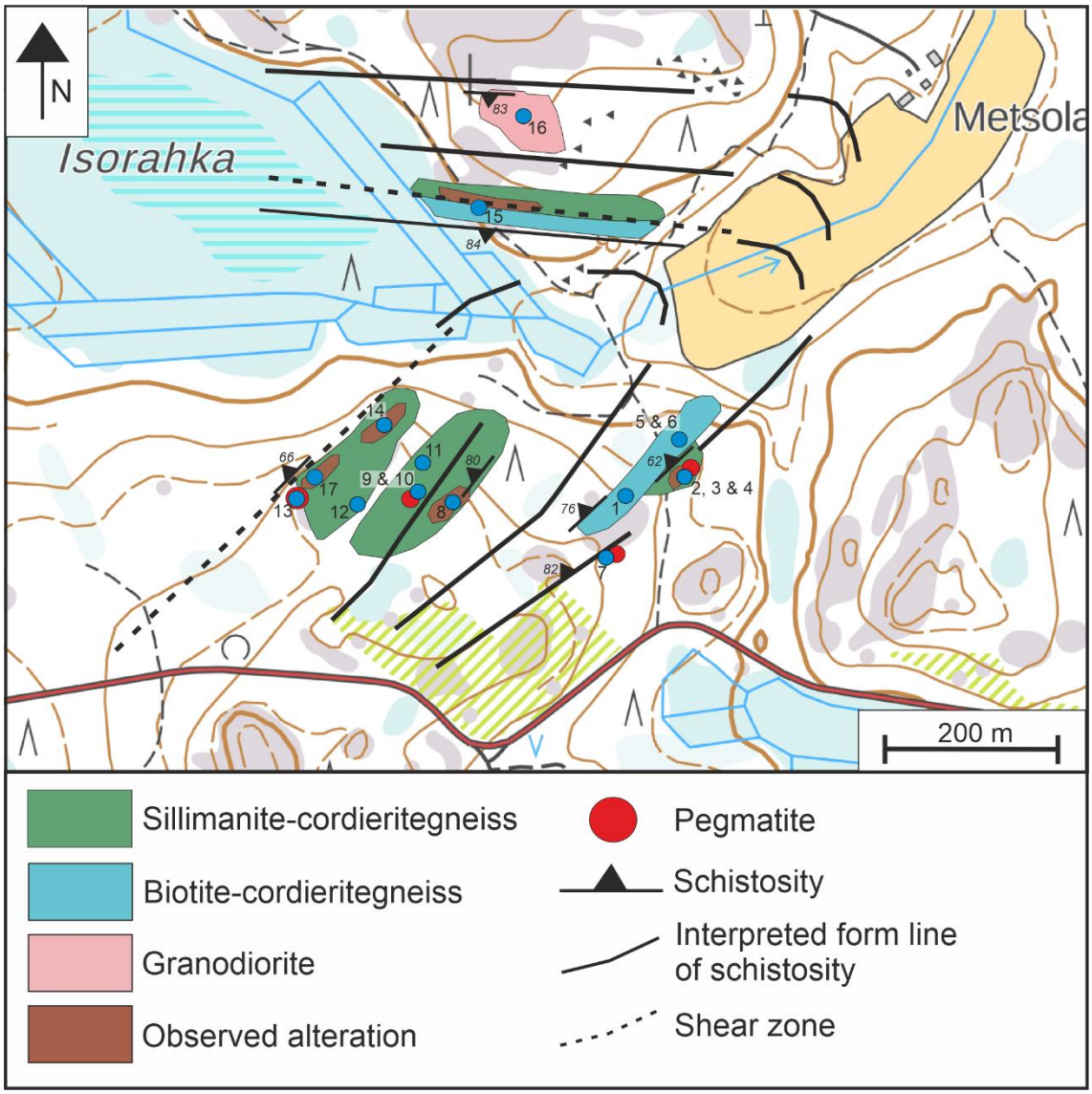

Figure 15. Simplified geological map of Kultanummi with observations. Numbers 1-17 indicate the observations, and information of these is summarized in Table 2. Basemap: Maastokartta 1:20000.

Table 2. Information of observation locations. Information includes their sampling ID, coordinates, type, rocktype, mineralogy, structural measurements and essential comments. Abbreviations: bt = biotite; qz = quartz; msc = muscovite; crd = cordierite; grt = garnet; sil = sillimanite; k-fsp = k-feldspar; plag = plagioclase; tr = tourmaline.

ID	Coordinates (ETRS-TM35FIN)	Type	Rocktype	Mineralogy	Structural measurement (XXX/YY)	Comments
NMHE-2024-01	N: 6710517, E: 276191	Observation	Biotite-cordieritegneiss	bt, crd, qz, grt	310/76	Partially melted, tightly folded
NMHE-2024-02	N: 6710549, E: 276254	Observation & sample	Sillimanite-cordieritegneiss	sil, crd, qz, bt, msc	317/62	Thoroughly altered and rusty
NMHE-2024-03	N: 6710549, E: 276254	Observation & sample	Pegmatite	qz, k-fsp, bt	—	Cuts as a vein, strike ca. 350 degrees
NMHE-2024-04	N: 6710549, E: 276254	Observation & sample	Sillimanite-cordieritegneiss	sil, crd, qz, bt, msc	—	Thoroughly altered and rusty, sillimanite grains clearly visible
NMHE-2024-05	N: 6710587, E: 276237	Observation	Biotite-cordieritegneiss	bt, crd, qz	280/81	Partially melted, tightly folded, different layers (psammitic and pelitic)
NMHE-2024-06	N: 6710566, E: 276246	Observation	Biotite-cordieritegneiss	bt, crd, qz	—	Parially melted, very psammitic
NMHE-2024-07	N: 6710450, E: 276150	Observation	Biotite-cordieritegneiss & pegmatite	bt, crd, qz, k-fsp, tr	333/82	Pegmatite cutting as a vein
NMHE-2024-08	N: 6710514, E: 275968	Observation & sample	Sillimanite-cordieritegneiss	sil, crd, qz, bt, msc	300/80	Rusty outcrop, partially melted
NMHE-2024-09	N: 6710524, E: 275941	Observation	Sillimanite-cordieritegneiss	sil, crd, qz, bt, msc	200/83	Rusty outcrop, evidence from research concluded by GTK visible
NMHE-2024-10	N: 6710524, E: 275942	Observation & sample	Pegmatite	qz, k-fsp, bt	—	Cuts as a vein
NMHE-2024-11	N: 6710546, E: 275947	Observation	Sillimanite-cordieritegneiss	sil, crd, qz, bt, msc	292/83	Folding visible, pegmatite vein penetrates axial plane
NMHE-2024-12	N: 6710525, E: 275888	Observation	Sillimanite-cordieritegneiss	sil, crd, qz, bt, msc, mgt	340/78	Folded magnetite-biotite layers visible, partially melted
NMHE-2024-13	N: 6710528, E: 275803	Observation & sample	Sillimanite-cordieritegneiss & pegmatite	sil, crd, qz, bt, msc, k-fsp, tr, plag	315/82	Layering partially folding, pegmatite cuts as a vein
NMHE-2024-14	N: 6710594, E: 275900	Observation	Sillimanite-cordieritegneiss	sil, crd, qz, bt, msc	—	Partially melted, very rusty outcrop, folded
NMHE-2024-15	N: 6710842, E: 276011	Observation & sample	Sillimanite-cordieritegneiss	sil, crd, qz, bt, msc	193/84	Altered & unaltered boundary visible at the outcrop, three samples taken with drill from different spots (NMHE-2024-15.1, -15.2 & -15.3). Shear zone visible at the outcrop.
NMHE-2024-16	N: 6710956, E: 276057	Observation	Granodiorite	qz, k-fsp, bt	185/83	Porphyric and folded
NMHE-2024-17	N: 6710531, E: 275816	Observation & sample	Sillimanite-cordieritegneiss	sil, crd, qz, bt, msc	338/66	Shear zone visible and sillimanite-rich layers bend with it. Four samples taken with drill from different spots (NMHE-2024-17.1, -17.2, -17.3 & -17.4)

Metasedimentary rocks are mainly either biotite- or sillimanite-cordierite gneisses (Figure 16). In most locations the rocks are typically partially melted/migmatized. Sillimanites stand out on the erosional surface, and they can be observed as mineral clusters. Hydrothermal alteration can be seen as rusty appearance of the rock in most places. Chlorite, which is considered as alteration product, is occasionally observed in thin sections, for example in thin section NMHE-2024-04. At some places it is also evident that sillimanite is altering to muscovite. Deformation appears in form of subvertical to vertical schistosity, that is locally tightly folded. Folds are usually associated with shear zones, however within the unaltered biotite gneisses the leucosomes are also folded (Figure 16A). It is evident that sillimanite is concentrated to the shear/high strain zones, which is especially clear in the outcrop in Figure 16C where a sillimanite-bearing quartz vein occurs in the shear zone.

Most thin sections are from altered metasedimentary rocks with one prepared from pegmatitic sample (Figures 17 C & D). In metasedimentary rocks the grain size is rather fine (mostly >0.5 mm), and shape of the grains varies from euhedral to anhedral. Pegmatitic sample has much coarser grain size. Quartz and biotite are abundant in all metasedimentary samples, and minor amounts of muscovite and K-feldspar can also be observed. Sillimanite is also present in thin sections, and it's very easy to identify due to

its fibrous appearance (Figure 17), and therefore it can be named as fibrolite. Sillimanites are grown over rest of the minerals in all cases, and it is commonly found throughout the thin sections. Tourmaline is also observable especially in quartz and sillimanite-rich spots. Hydrothermal alteration can be seen as the presence of sillimanite and cordierite, and in places chlorite is also present. It is noted that unaltered biotite gneisses lack sillimanite, cordierite and other alteration minerals. Bedded structure of metasedimentary rock is clear from thin sections. Pegmatitic sample (NMHE-2024-13b) show much coarser grain size and it contain a lot of sillimanites. Sulfide and oxide minerals (Figures 17 I & J) are mostly pyrite and pyrrhotite with minor amounts of chalcopyrite, and in some samples magnetite and rutile are also present. These minerals are often associated with sillimanites. In some rutiles the spots left from LA-ICP-MS analysis can be observed.

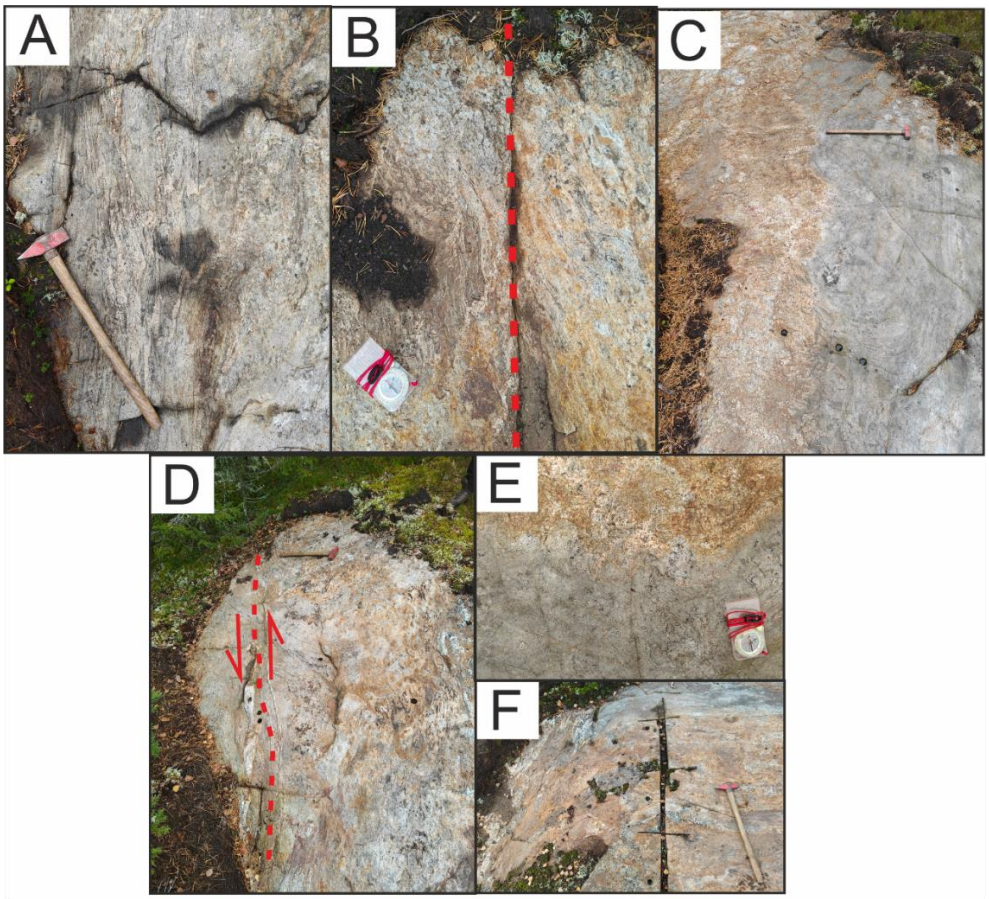

Figure 16. Typical lithologies of Kultanummi area. The tip of hammers handle points towards north. A) Observation NMHE-2024-01 that shows the typical partially melted and folded biotite-cordierite gneiss. B) Observation NMHE-2024-14 that shows more rusty biotite-cordierite gneiss which is cut by SW-NE trending shear zone. C) Observation NMHE-2024-17 that also shows about SW-NE trending shear zone. Rock type is sillimanite-cordierite gneiss, and the outcrop is rusty. Holes left from drilling machine can also be seen. D) Outcrop NMHE-2024-15 that shows a clear boundary between unaltered bedrock and highly altered bedrock. Rock type at the altered zone is sillimanite-cordierite gneiss and at unaltered spot the rock is more psammitic. The holes from drilling machine can also be seen. E) Closer picture from NMHE-2024-15 that show the transition from unaltered to altered bedrock. F) Observation NMHE-2024-09 that shows the trail left by sampling machine when GTK studied the area in early 2000s. The outcrop is similar sillimanite-cordierite gneiss.

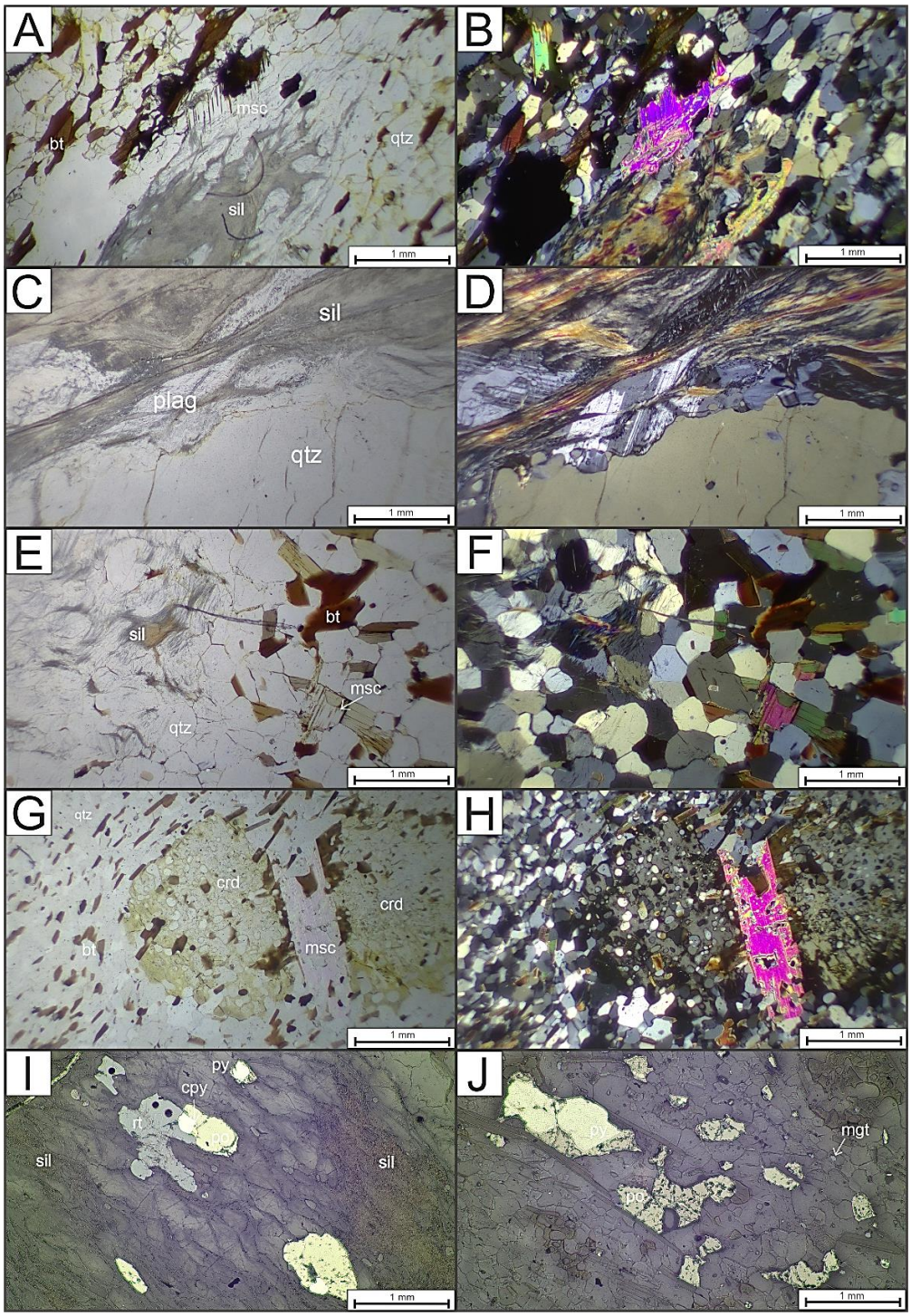

Figure 17. Pictures of thin section from different samples. A) & B) sample NMHE-2024-04 in plane (left) and cross-polarized light (right). Alteration between muscovite and sillimanite is evident. C) & D) sample NMHE-2024-13b in plane (left) and cross-polarized light (right). E) & F) sample NMHE-2024-15.1a in plane (left) and cross-polarized light (right) G) & H) sample NMHE-2024-17.2a in plane (left) and cross-polarized light (right). Two large cordierite grains are clearly visible. I) sample NMHE-2024-15.1a with reflected light. Spots left from LA-ICP-MS can be seen in rutiles. J) sample NMHE-2024-17.2a with reflected light. Abbreviations are as following: sil = sillimanite; msc = muscovite; qtz = quartz; bt = biotite; plag = plagioclase; rt = rutile; py = pyrite; crd = cordierite; po = pyrrhotite; cpy = chalcopyrite and mgt = magnetite.

6.2 U-Pb age determination

Age determinations were carried out from four thin sections: NMHE-2024-04, NMHE-2024-13b, NMHE-2024-15.1a and NMHE-2024-17.2a. Rock type in all thin sections was sillimanite-cordierite gneiss, except thin section NMHE-2024-13b, which was a pegmatitic sample. Minerals for age determinations are zircon, monazite and rutile.

BSE-images were used for identifying the minerals for age determination. Zircons are abundant throughout the samples. Length of the zircon grains is mainly between 20 and 100 µm. Shape of zircons vary a lot from euhedral to anhedral and they are often associated with biotite and quartz (Figure 18 A & B). Zircons are evenly distributed in all thin sections. Core and rim structures can be observed in some grains although majority of the grains seem to lack internal structure. Monazites are also abundant in all the samples. Length of the monazite grains are mainly on between 20 – 80 µm. Their crystal shape varies between euhedral to rounded (Figure 18 C & D). Due to the very high white reflection of monazites, internal structures are very hard to be determined from BSE images. Some monazites are rather anhedral and altered, and in some spots, they are in contact with sillimanites and rutiles (Figure 18F). Rutiles are very abundant in the samples, especially in thin section NMHE-2024-17.2a, where over 1600 rutile grains were detected. Their shapes vary from euhedral to complex cluster of grains (Figure 18E), and especially in thin section NMHE-2024-15.1a, rutile grains are very irregular shaped, and they are often altered to ilmenite (Figure 18F). Rutile grains are also commonly larger compared to zircon and monazite with average length of 20 – 160 µm, and in sample NMHE-2024-15.1a the length of grains is up to 600 µm. Rutiles are often as inclusions and in some places in contact with sillimanites (Figures 17I and 18F).

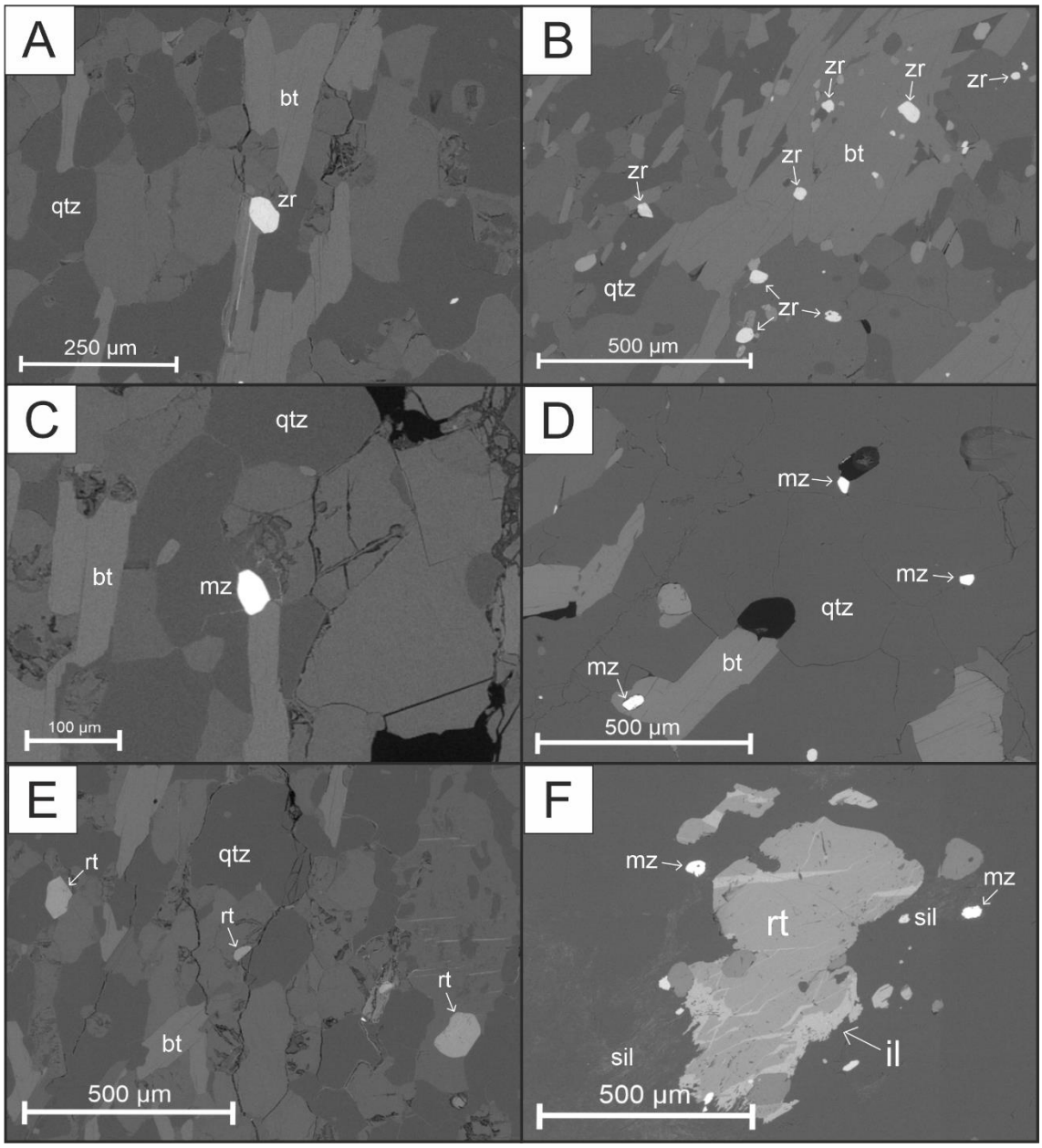

Figure 18. SEM-EDS (BSE) images of different minerals. A) euhedral zircon (zr) grain in sample NMHE-2024-04. This grain provided following ages: $^{206}Pb/^{238}U$ = 1889 Ma, $^{207}Pb/^{235}U$ = 1885 Ma and $^{207}Pb/^{206}Pb$ = 1881 Ma. B) zircon grains with different shapes from sample NMHE-2024-17.2a. C) Subrounded monazite (mz) grain from sample NMHE-2024-04. This grain provided following ages: $^{206}Pb/^{238}U$ = 1777 Ma, $^{207}Pb/^{235}U$ = 1779 Ma and $^{207}Pb/^{206}Pb$ = 1781 Ma. D) euhedral monazite grains from sample NMHE-2024-17.2a. E) rutile (rt) grains from sample NMHE-2024-04. One of the grains is very euhedral and the two are more rounded. F) Very irregular shaped rutile grain from sample NMHE-2024-15.1a. Grain is very large, and it has started altering to ilmenite (il). Rutile is in contact with sillimanite (sil) and two irregular-shaped and altered monazite grains are also in close proximity of rutile and in contact with sillimanite. Other abbreviations are as following: qtz = quartz and bt = biotite.

A total of 73 zircon grains were analysed with LA-ICP-MS. All the samples provided similar zircon U-Pb results and therefore the results are combined and addressed together. Three populations were observed based on the age data: age population one with $^{207}Pb/^{206}Pb$ ages between 2719 Ma – 1912 Ma, age population two with $^{207}Pb/^{206}Pb$ ages between 1899 Ma – 1871 Ma and age population three with $^{207}Pb/^{206}Pb$ ages between 1869 Ma – 1827 Ma. Population division was based merely on age data. All the analyses are shown in Figure 19.

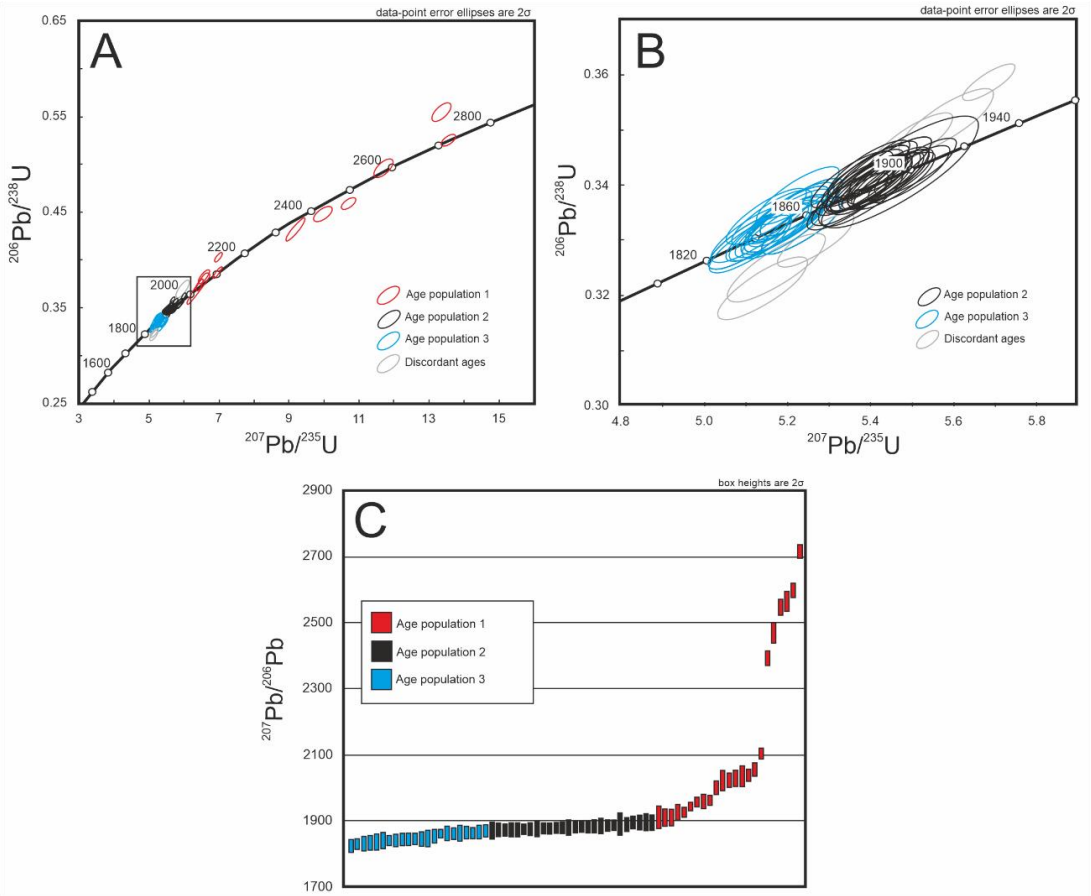

Figure 19. A) All zircon U-Pb analyses on concordia diagram; B) Close-up of the age populations 2 and 3; C) All zircon U-Pb analyses on weighted average $^{207}Pb/^{206}Pb$ diagram. Discordant ages were left out from the concordia age calculation.

Based on the broad scale of ages, which can be seen from $^{207}Pb/^{206}Pb$ ages in Figure 19C, the age population one is considered to consist of inherited grains and was not further studied. It can also be interpreted that zircon grains belonging to this age group are more rounded and sometimes rather irregular-shaped compared to two other age

groups. Thus, the focus is on age populations two and three. Six analyses from population two and seven from population three were omitted from the concordia age calculation due to high discordancy. After this exclusion, the concordia ages of 1885 ± 3 Ma (n = 21, 2σ, MSWD = 6.1) for the population two (Figure 20A) and concordia age of 1856 ± 4 Ma (n = 14, 95% confidence, MSWD = 0.73) for the population three (Figure 20C) were calculated. In addition of concordia ages, the $^{207}Pb/^{206}Pb$ weighted average age was also calculated for both populations in which the discordant analyses were also considered. Thus, a weighted average age of 1883 ± 3 (n = 27, 2σ, MSWD = 0.93) for the population two (Figure 20B) and a weighted average age of 1851 ± 6 (n = 21, 95% confidence, MSWD = 3.1) for the population three (Figure 20D) were calculated.

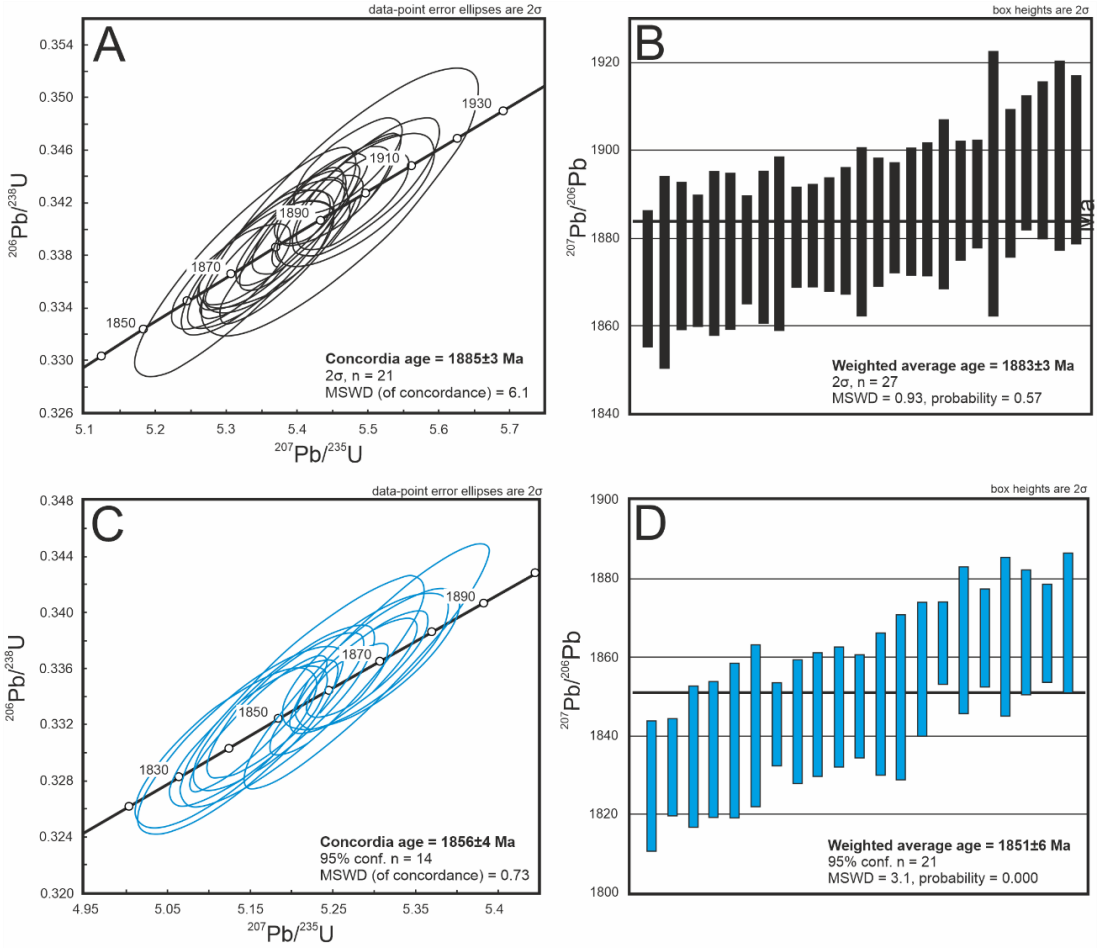

Figure 20. A) concordia diagram for age population 2; B) weighted average diagram for age population 2; C) concordia diagram for age population 3; and D) weighted average diagram for age population 3.

A total of 84 monazite grains were analysed with LA-ICP-MS. Eight analyses were rejected due to bad U-Pb signal (not shown in the diagrams). Three populations were identified merely based on the $^{207}Pb/^{206}Pb$ ages: age population one (two analyses with ages of 1871 Ma and 1868 Ma), age population two with ages between 1816 Ma – 1813 Ma and age population three with ages between 1813 Ma – 1767 Ma. All the analyses are shown in Figure 21.

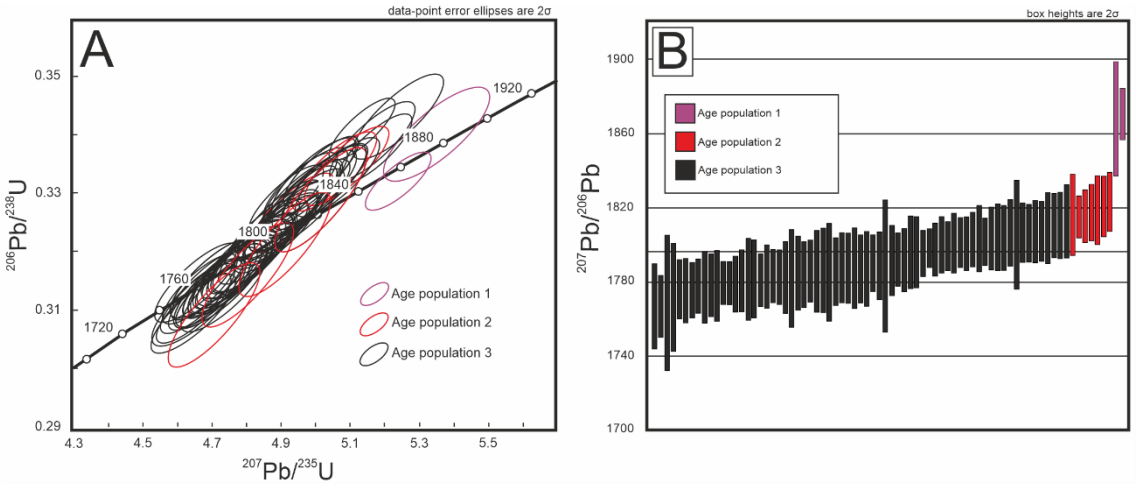

Figure 21. A) all monazite analyses in concordia diagram; and B) all analyses in weighted average diagram.

Because monazite data was considered to be very reliable, no analyses were omitted due to discordancy. Therefore, an upper intercept age of 1818 ± 5 Ma (n = 7, MSWD = 0.22) for age population two (Figure 22A) and an upper intercept age of 1788 ± 4 Ma (n = 67, MSWD = 1.8) for age population three (Figure 22C) were calculated. The $^{207}Pb/^{206}Pb$ weighted average was also calculated for both age populations yielding ages of 1818 ± 6 (n = 7, 2σ, MSWD = 0.18) and 1791 ± 3 (n = 67, 95% confidence, MSWD = 2.1) for age population two (Figure 22B) and age population three (Figure 22D), respectively.

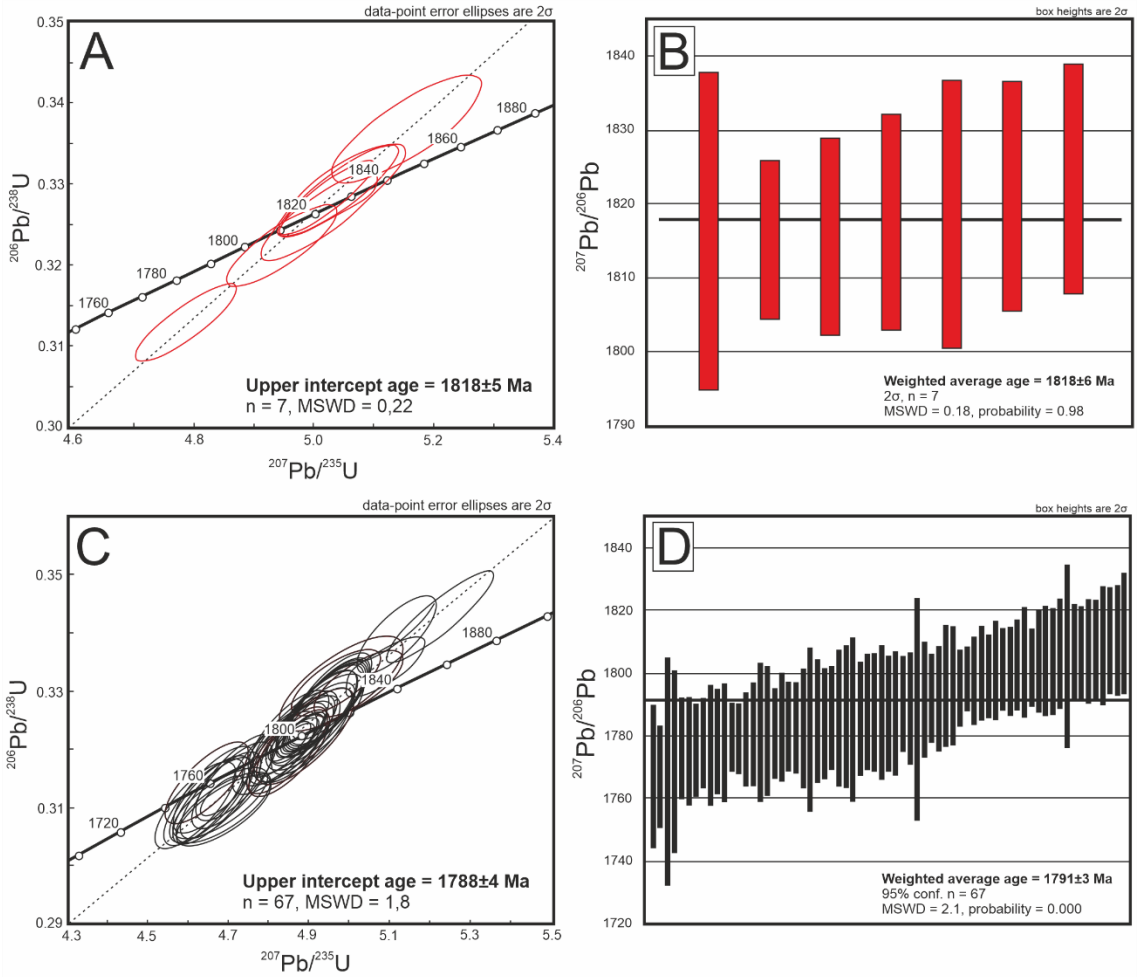

Figure 22. A) an upper intercept diagram for age population 2; B) weighted average diagram for age population 2; C) an upper intercept diagram for age population 3; and D) weighted average diagram for age population 3.

A total of 85 rutile grains were analysed with LA-ICP-MS. Five analyses were rejected from the data analysis due to extremely high reverse discordancy. Whole dataset is considered as one population, and the analyses are shown in Figure 23.

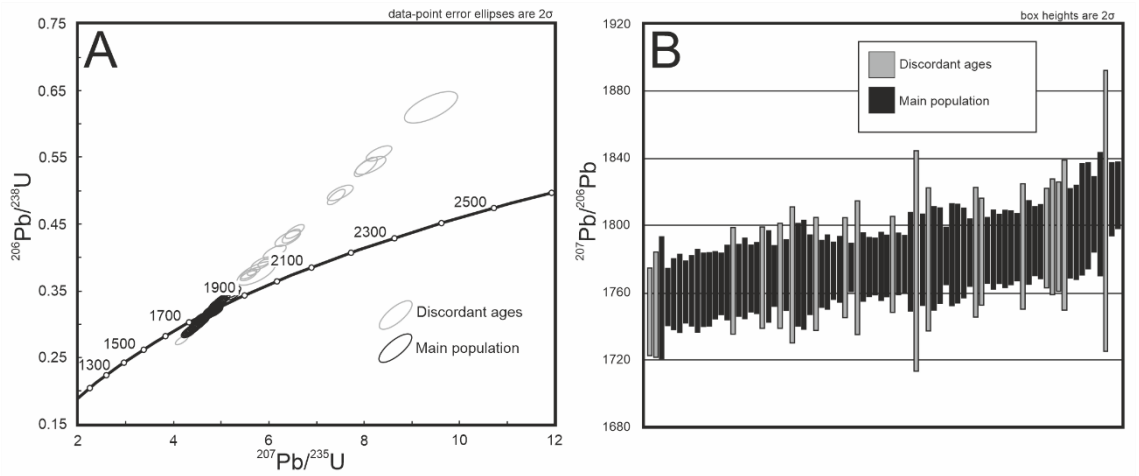

Figure 23. A) All rutile analyses on concordia diagram; and B) $^{207}Pb/^{206}Pb$ weighted average diagram.

20 analyses were reversely discordant due to Pb-U fractionation, and they were omitted from age calculations. Thus, an upper intercept age of 1781 ± 4 Ma (n = 60, MSWD = 1.6) and a weighted average age of 1777 ± 4 Ma (n = 60, 95% confidence, MSWD = 1.6) were determined for rutiles. The diagrams are shown in Figure 24.

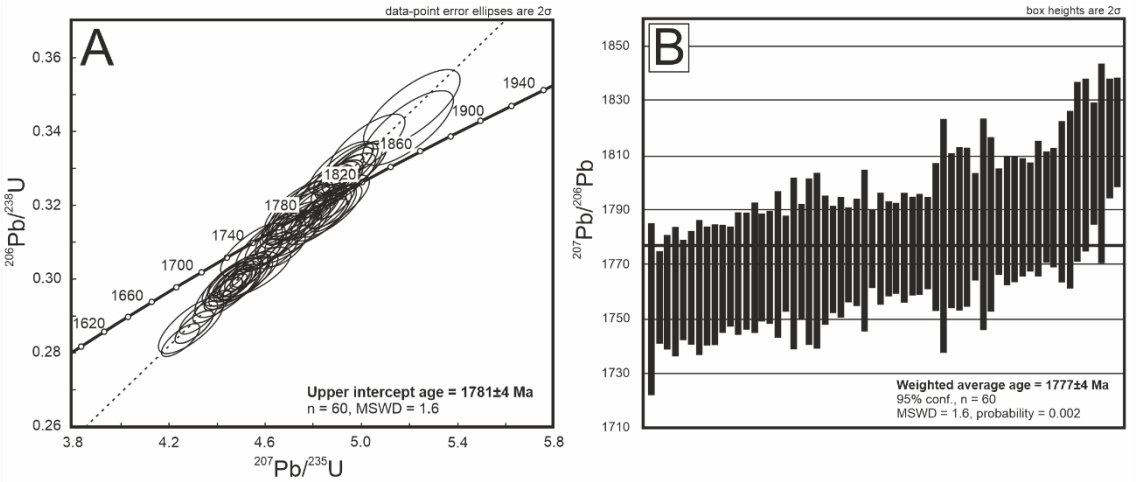

Figure 24. A) Upper intercept age; and B) $^{207}Pb/^{206}Pb$ weighted average age for rutiles.

7. Discussion

7.1 Age constraints

Based on the results, it is evident that multiple geological events can be described from Kultanummi. Firstly, two main events are indicated by the zircon ages; age population two with concordia age of 1885 ± 3 Ma (Figure 20 A) is interpreted to resemble early Svecofennian event in Fennian phase and age population three with age of ca. 1856 ± 4 Ma (Figure 20 C) is interpreted to resemble metamorphic event related to orogenic collapse after Fennian phase. In addition, age population one of zircons (Figure 19) is interpreted to resemble inherited ages due to metasedimentary origin of host rock as the age analyses varies a lot. For the monazites the age population one (ages of ca. 1870 Ma, Figure 21) can be addressed to resemble Fennian phase in similar manner with age population two of zircons. Age population two of monazites (1818 ± 5 Ma, Figure 22 A) on the other hand can be addressed to resemble metamorphic peak in the Uusimaa Belt. Age population three of monazites (1788 ± 4 Ma, Figure 22 C) and also the only age population of rutiles (1781 ± 4 Ma, Figure 24) can be addressed to resemble hydrothermal activity during long time period after metamorphic peak in southern Finland when temperature have been dropped down and other forces (e.g. post-orogenic magmatism) have been driving the fluid activity.

The zircon age population one (Figure 19) can be interpreted to present older, inherited zircons due to their broad scale of ages. These inherited zircons can be found from thin sections NMHE-2024-04, NMHE-2024-15.1a and NMHE-2024-17.2a. From BSE images (Figure 18B) it can be interpreted that some zircon grains belonging to this age group are more rounded and sometimes rather irregular-shaped compared to two other age groups. Therefore, the ages of population one resembles the original crystallisation of zircons in their source rock at least for the older ages on this population. Younger ages of ca. 1928 Ma – 1913 Ma can be interpreted to resemble the initial stage of Svecofennian orogeny at 1.92 Ga – 1.91 Ga when Lapland-Savo phase took place (Lahtinen et al., 2005).

For the other two populations of zircons (age population two and three), which are also found from thin sections NMHE-2024-04, NMHE-2024-15.1a and NMHE-2024-17.2a, several interpretations can be made. For the age population two the concordia age of 1885 ± 3 Ma (Figure 20A) can be interpreted to resemble the first metamorphic event of southern Svecofennia when volcanic arc collided from south between 1.89 Ga – 1.87 Ga during Fennian phase (Lahtinen et al., 2005). Several studies also suggest a major

magmatic event related to arc collision in southern Finland due to similar age determination results and interpretations (e.g. Nironen, 1997; Tiainen et al., 2013; Kara et al., 2020). Th/U ratios of zircon population two are ca. 0.34 (Appendix 1), which indicates that these zircons are formed from partial melting during Fennian phase. These results are different when comparing the rest of Uusimaa Belt since the metamorphic peak in Uusimaa Belt is interpreted to happen at ca. 1.82 Ga (Väisänen et al. 2002), but these ages are not found from zircons on this study. Younger zircon population (age population three) with concordia age of 1856 ± 4 Ma (Figure 20C) can be interpreted to resemble extensional period related to orogenic collapse (Lahtinen et al., 2005). Several authors have also highlighted this metamorphic peak at ca. 1.86 Ga (e.g. Väisänen et al., 2021). Th/U ratios are higher compared to previous population with ratios of ca. 0.48 (Appendix 1). In addition, Kara et al. (2020) discussed that the metamorphism during this time was caused by crustal extension combined with arclogite (eclogite-facies rocks which are composed of amphiboles, clinopyroxene, garnet and rutile) delamination. Therefore, it is possible that these zircon ages can be addressed to represent metamorphic event caused by extensional tectonics and upper mantle upwelling.

From monazites of Kultanummi two older ages (population one) are ca. 1871 Ma and 1868 Ma (Figure 21), which are found from thin section NMHE-2024-13b and NMHE-2024-17.2a. These ages can be linked to first metamorphic event related to Fennian phase (Lahtinen et al., 2005). The ages of these monazites are younger compared to zircons related to same tectonic event. This might be due to the fact that monazites closure temperature in U-Pb system is lower compared to zircon, as the typical closure temperature for monazites are usually between 700 °C – 800 °C (Smith & Giletti, 1997) and for zircons they are often over 900 °C (Cherniak & Watson, 2003). Based on these facts it is possible that monazites have been closed at later stage of Fennian phase when temperature have decreased. Same interpretation can be addressed when comparing the monazite age population two (Figure 22 A & B) to the metamorphic peak age from the Uusimaa Belt of ca. 1825 Ma obtained from zircons (Väisänen et al., 2002). Monazite analyses for age population two on this study are 1818 ± 5 Ma (upper intercept age) and these monazites are found from thin sections NMHE-2024-04, NMHE-2024-15.1a and NMHE-2024-17.2a. It is noted that these ages related to metamorphic peak event are not found from zircons. Monazites belonging to this age population are little bit younger compared to metamorphic peak age of Uusimaa Belt. This difference might be explained by monazites lower closure temperature compared to zircons. Monazite is also reactive mineral in fluid-rich environments, and it can be crystallised during long time periods (e.g.

Högdahl et al., 2012). Therefore, monazite age population two is suggested to represent the peak metamorphic age in southern Finland.

For the youngest population of monazites (age population three, Figure 21) from thin sections NMHE-2024-04, NMHE-2024-13b, NMHE-2024-15.1a and NMHE-2024-17.2a and the single determined population of rutiles (Figure 23) from thin sections NMHE-2024-04, NMHE-2024-15.1a and NMHE-2024-17.2a, a hydrothermal origin is proposed. Hydrothermal activity is especially clear in rutile grains since some grains are very irregular shaped (Figure 18F) which might be an indication of fluid activity. In addition, the alteration between rutile and ilmenite is evidence of fluid activity (Meinhold, 2010). Rutile age (Figure 24) is 1781 ± 4 Ma (upper intercept age) and monazite age (Figure 22 C) is 1788 ± 4 Ma (upper intercept age). This little age difference can be explained by the lower closure temperature of rutile (about 500 °C) compared to monazite (700 °C – 800 °C). Although, there isn't clear clustering of monazites in thin section which would be a strong indication of hydrothermal origin (Schandl & Gorton, 2004), some monazite crystals are still rather irregular shaped as they are little bit rounded (Figure 18 C, D & F) and clearly altered, which can be seen from their irregular shaped edges (Figure 18F). This could be an indication of hydrothermal activity. In addition, these irregular-shaped monazites often occur in close contact with irregular-shaped rutiles (Figure 18F), suggesting that they have been affected by same hydrothermal processes. Monazites have also been determined to react highly in hydrothermal processes and retrograde metamorphism (e.g. Poitrasson et al., 1996; Fitzsimons et al., 2005; Högdahl et al., 2012; Janots et al., 2012). In all, based on these interpretations, it is proposed that these two populations of monazite and rutile could represent hydrothermal activity.

Although the hydrothermal origin for these two minerals can be addressed, the driver for the fluid activity is still questionable as most of the tectonic activity was ceased in southern Finland after the metamorphic peak event at ca. 1825 Ma during Svecobaltic phase (Lahtinen et al., 2005). Several possible causes for fluid activity after this orogeny can be proposed. One cause might be the orogenic collapse at ca. 1.79 Ga – 1.77 Ga that took place after the last orogenic event in southern Finland (e.g. Lahtinen et al., 2005; Korja et al., 2006). This event coincides well with hydrothermal ages of monazites and rutiles (Figures 22 & 24). In addition, first stages of intrusion of Transcandinavian Igneous Belt (TIB) at ca. 1.81 Ga – 1.76 Ga (Högdahl et al., 2004) would also possibly contribute as the driving force of fluid activity. Some post-collisional igneous activity has also been interpreted from southern Finland in form of pegmatites with ages ca. 1.80 Ga

– 1.79 Ga (Alviola et al., 2001) and other 1.81 Ga – 1.76 Ga post-collisional intrusions throughout southern Finland (Teräs et al., 2025).

7.2 Genesis of Kultanummi deposit – orogenic or epithermal?

Determination of the type of gold deposit in Kultanummi is problematic due to its complex geological history and multiple deformation events that can be observed from the area. In addition, metamorphic grade of high amphibolite facies (Figure 25) and alteration sequences are untypical for most gold deposit types. Based on the previous research on Kultanummi (Grönholm et al. 2005; Grönholm & Kärkkäinen 2006) and field observations, deposit type can be narrowed to present one of the two types: either orogenic or epithermal mineralization. Based on the results on this study, I suggest that that the deposit type of Kultanummi is orogenic gold deposit, which was formed by Al-rich fluid. In Kultanummi gold mineralization and alteration sequences is structurally controlled, presence of sillimanite and cordierite is closely associated with gold mineralization and age results suggests that fluid activity is post-metamorphic in age, which coincides with orogenic gold genetic model (Groves et al., 1998). In addition, interpreting Kultanummi as an epithermal deposit is more challenging due to the complex deformational and metamorphic history of the area, however, an epithermal deposit type can't be completely excluded. Therefore, additional research is needed in the area for definition of Kultanummi as an epithermal deposit.

Orogenic and epithermal gold deposits can be formed in rather similar settings as they both are formed at convergent plate margins during subduction/orogenic processes. However, their genesis differs greatly as epithermal deposits are related to porphyry deposits (Sillitoe, 2010) and are often formed in hot springs whereas orogenic gold deposits are related to orogenic processes during syn- to post-peak metamorphic events and they don't require intrusion when formed (Goldfarb & Groves, 2015). There is strong evidence of arc type volcanism during earlier stages of Svecofennian orogeny ca. 1.90 – 1.87 Ga (Lahtinen et al., 2005). Arc volcanism is essential for epithermal deposits, and if Kultanummi is characterized to represent epithermal deposit, gold would have been precipitated during this period. This would imply that gold mineralization is older compared to later tectonic events in the area. Age population two of zircons on this study would coincide with this arc volcanism (Figures 20 A & B). However, epithermal deposits are often associated with porphyry deposits as their genetic link to intrusions contributes as the source for the mineralising fluids (Sillitoe, 2010). Porphyry deposits haven't been observed in the proximity of Kultanummi area nor in Finland in general. Since Kultanummi is metamorphosed in later tectonic events after Fennian phase at 1.90 –

1.87 Ga, it would mean that the primary mineralogy has been altered. Epithermal deposits are often characterised by Al-bearing minerals like illite and smectite, but as these minerals are not found from Kultanummi (Al-bearing minerals are sillimanite and cordierite), it might be possible that these primary Al-bearing minerals have been altered to cordierite and sillimanite. According to Thompson (1982), sillimanite can be formed in metapelitic rocks in high-grade metamorphism by the following reaction:

$$muscovite + biotite + quartz + H_2O \rightarrow sillimanite + melt \quad (16)$$

Therefore, it is evident that when Al-rich minerals are available, sillimanite is able to form in high metamorphic conditions at P-T conditions about 4 – 6 kb and 640 – 740 °C. As illite and smectite are Al-bearing minerals like muscovite and biotite, it is highly possible that this same reaction can be applied to form sillimanite.

Characterizing Kultanummi as orogenic gold deposit is not straightforward either. Firstly, high metamorphic grade of the area (high amphibolite facies, Figure 25) is not typical for orogenic gold deposits as these metamorphic conditions don't usually favour gold precipitation. However, some orogenic gold deposits have been described from high metamorphic grade areas, especially from Australia (e.g. Barnicoat et al., 1991; Cassidy, 1992), and also from Finland (Figure 25). Secondly, as the presence of sillimanite and cordierite are one of the main controlling factors of gold mineralization in Kultanummi (Grönholm & Kärkkäinen, 2006), fluid carrying gold would have to be aluminium rich (sillimanite and cordierite are Al-bearing silicates) which is not typical in orogenic gold systems. However, such fluids, which are rich in H_2O, Al and B, have been described e.g. from Himalayas in India (Roy et al., 2023), where it is interpreted that sillimanites have been formed through metasomatism after peak metamorphism. These Al-rich fluids have flown within ductile shear zones, which is also evident in Kultanummi area as gold mineralization tends to be structurally controlled in the area. Presence of cordierite would also fit with these types of fluids. Temperature of the fluid must be high (>550 °C) to produce sillimanite (Roy et al., 2023), but this temperature can be achieved due to high P-T conditions on the later stages of Svecofennian orogeny (Lahtinen et al., 2005). In addition, presence of aluminium-rich minerals (K-feldspar and micas) makes it possible for sillimanite to form (reaction 16). Based on observations from thin sections, sillimanites and rutiles tend to be closely associated with each other (Figure 17l). Similar association of rutiles in sillimanite bearing shear zone was also observed in the Himalayan shear zones (Roy et al., 2023). Age determination on rutiles yielded age of ca. 1781 ± 4 Ma (upper intercept age), which can be contributed to present the age of the fluid activity for Al-rich fluid. Therefore, the fluid activity is significantly younger compared to peak

metamorphic age in southern Finland. This would also mean that sillimanite is formed due to presence of fluid activity and would therefore be an alteration product. From the thin sections it can be observed that sillimanites are in all cases grown over other minerals, and the shape of the sillimanites resembles that they have formed due to fluid activity as the flow pattern is observable (for example in Figure 17 C & D). Gold in Kultanummi area is closely associated with sillimanites, which means that gold has been transported in these Al-rich fluids and precipitated sometime after 1.80 Ga based on rutile (and also monazite) ages. In addition, structural control of gold mineralization and alteration is evident in the area. Therefore, it's plausible that the genetic type is orogenic gold formed by Al-rich fluid.

7.3 Comparison between other gold deposits in southern Finland

Multiple gold deposits are described from southern Finland (e.g. Eilu et al., 2003, Figure 25) of which most represent orogenic gold type (e.g. Satulinmäki and Riukka, Saalmann et al., 2009). Epithermal deposits are considered to be much less abundant in southern Finland, the most prominent one being the Kutemajärvi deposit (e.g. Luukkonen, 1996; Talikka & Mänttäri, 2005). Zircon ages of ca. 1896 Ma and titanite ages of ca. 1850 Ma have been determined from Kutemajärvi (Talikka & Mänttäri, 2005). The zircon ages are somewhat similar compared to zircon ages determined from Kultanummi on this study (age population 2 of zircons at ca. 1885 Ma, Figures 20 A & B). The host rock for mineralization in Kutemajärvi is interpreted to be sericite-quartz schist with vertical quartz “pipes” cutting through the lithologies (Luukkonen, 1996), whereas in Kultanummi the host rock is sillimanite-rich gneiss. Alteration assemblages are partly similar, as in both cases silicification is common and chlorite is present, but sillimanite and cordierite are not found from Kutemajärvi (Luukkonen, 1996). Moreover, the metamorphic grade varies from high amphibolite facies in Kultanummi to lower amphibolite facies in Kutemajärvi (Eilu et al., 2003; Figure 25).

Like mentioned before, most gold deposits described from southern Finland are interpreted to be an orogenic origin. The most prominent orogenic gold deposits in southern Finland are for example Satulinmäki and Riukka from Häme Belt (Saalmann et al., 2009). These deposits are shown in Figure 25. These deposits are characterized by structural control in shear zones, which is also observable in Kultanummi area. Silicification is a common phenomenon in both Satulinmäki and Riukka, which can also be observed in Kultanummi. In contrast, no aluminium-bearing minerals (sillimanite and cordierite) are present in these deposits, which makes them different from Kultanummi. Quartz veins are the main host of gold mineralization in both Satulinmäki and Riukka and

they are crosscutting the metavolcanic (felsic to mafic) and metasedimentary lithologies. This is also differing characteristic from Kultanummi as the host for gold are sillimanite- and quartz-rich gneisses. Multiple generations of quartz veining can be determined from both areas, but the late Svecofennian veins are the dominant hosts for gold mineralization (Saalmann et al., 2009). Age determination results of gold mineralization from these areas are mainly between ca. 1.82 Ga – 1.79 Ga (Saalmann et al., 2009), which would coincide with age results from Kultanummi area on this study since the interpreted fluid activity populations from monazites (Figure 22 C & D) and rutiles (Figure 24) shows similar results. Metamorphic grade in Kultanummi, Satulinmäki and Riukka are different since Kultanummi is located in high-amphibolite facies (Figure 25), whereas Satulinmäki and Riukka are interpreted to have been metamorphosed in low- to middle amphibolite facies (Saalmann et al., 2009).

Another example of orogenic gold deposit from Svecofennian is Kullaa area, which host several small mineralizations (Kara et al., 2025). Kullaa area is characterized by shear zones and folding structures, which are suitable places for gold precipitation to occur. In Kultanummi brittle-ductile structures can be observed as well (Figure 16). Quartz veins are the main host for gold in Kullaa. Metamorphic grade is similar in both Kultanummi and Kullaa as both deposits are in high amphibolite facies (Figure 25). Interestingly, the geochronological results show similarities in both study areas. Kara et al. (2025) have determined multiple age populations from the Kullaa area; first, the metamorphic peak age of ca. 1887 Ma, which is very close to the zircon ages in population 2 on this study (Figure 20 A & B). Secondly, the secondary metamorphism ages of ca. 1860 Ma which are fairly similar to the zircon ages in population 3 on this study (Figure 20 C & D). Thirdly, the younger ages of ca. 1820 Ma – 1780 Ma which are determined from multiple minerals (zircon, monazite, titanite and garnet). Similar ages are also determined from Kultanummi on this study; age populations two and three from monazites (Figure 22) and single rutile population (Figure 24) fall between these ages also. Therefore, the age relationships are very similar between Kullaa and Kultanummi; the main differences are related to host rocks of gold mineralization and alteration assemblages.

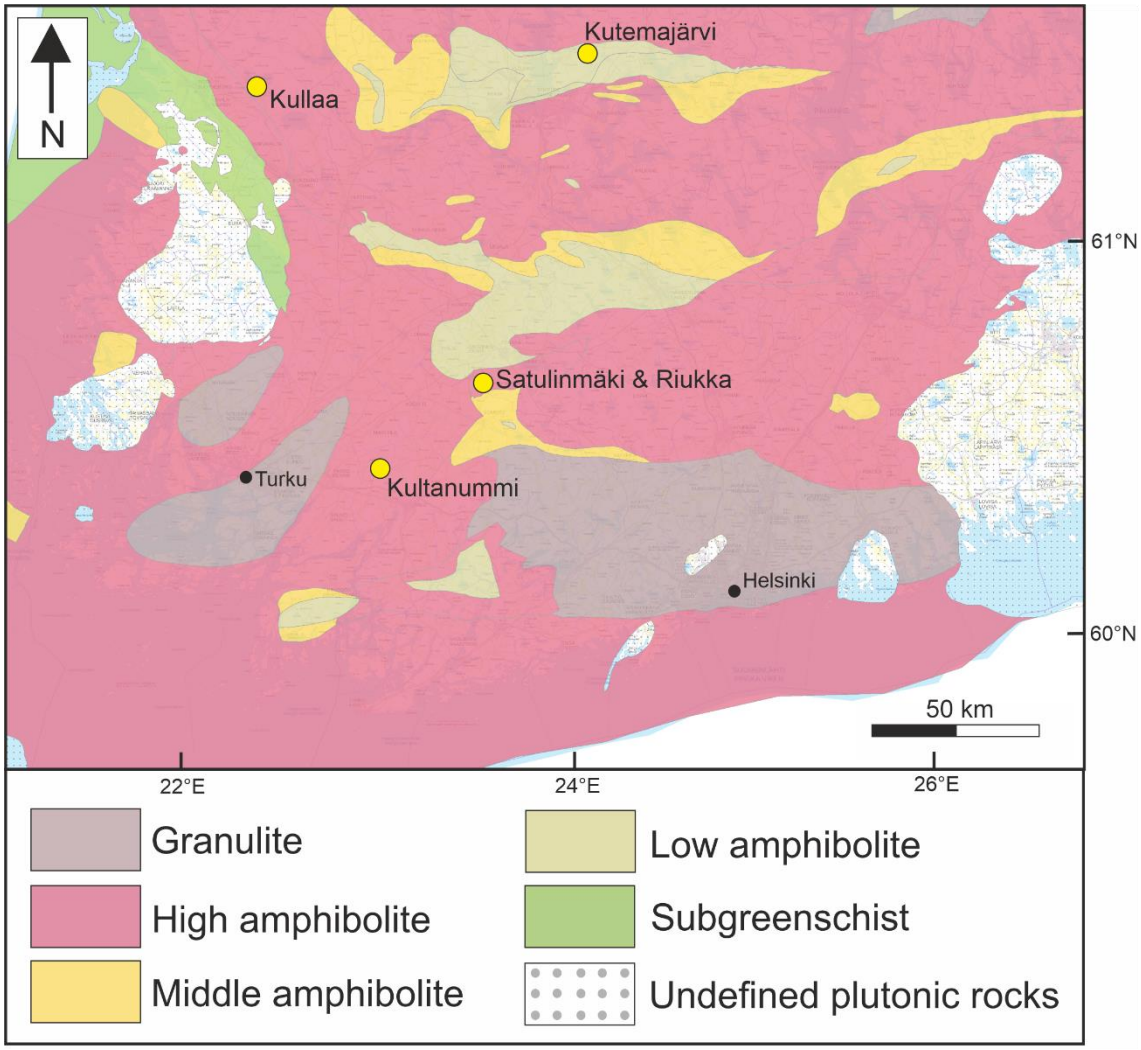

Figure 25. Metamorphic map (scale 1:1000000) of southern Finland with gold deposits discussed in this chapter. Modified after Hölttä & Heilimo (2017).

8. Conclusions

It is evident that multiple geological events can be described from Kultanummi area based on the results on this study. In addition, it is a complex task to determine the possible deposit type for gold mineralization in Kultanummi area. Some concluding remarks can be made:

1. Zircon population two (1885 ± 3 Ma) resembles the early stage of Svecofennian orogeny when volcanic arc collided with Keitele microcontinent from south and partial melting occurred. This is also the main population of zircons. In other hand zircon population three (1856 ± 4 Ma) resembles extensional stage between two major orogenic events where extension and orogenic collapse occurred.
2. Monazite population one with ages of ca. 1870 Ma can be linked to the same orogenic event than the age population two of zircons, whereas monazite population two (1818 ± 5 Ma) is interpreted to resemble metamorphic peak of the Uusimaa Belt and population three (1788 ± 4 Ma) is interpreted to resemble hydrothermal activity after metamorphic peak event.
3. Single rutile population with ages of ca. 1777 ± 4 Ma is interpreted to resemble hydrothermal activity in similar manner with age population three of monazites. Driving force for this hydrothermal activity can be for example orogenic collapse after 1.80 Ga and post-orogenic magmatism.
4. The Kultanummi gold deposit is structurally controlled and has precipitated after 1.80 Ga, therefore it can be defined as orogenic type gold deposit genetically.
5. Gold mineralization is associated sillimanite rich lithologies, therefore it is likely that gold-carrying fluid in Kultanummi has been Al-rich.

9. Acknowledgements

First, I want to thank my supervisor Jaakko Kara for presenting the topic of thesis and for his guidance throughout the whole project. Professor Esa Heilimo is also thanked for helping with the writing process, and he was also the first person to tell me about the topic. Staff at the laboratory on GTK are thanked; first, PhD Paavo Nikkola for the guidance of using SEM, and secondly, PhD Matti Kurhila for the guidance of using mass spectrometer. I would also like to thank Arto Peltola for making the thin sections. I would also like to thank Markku Väisänen since he was on field for one day with me and Jaakko as a guide.

10. References

Allègre, C.J. 2008. Isotope geology. Cambridge University Press. 512 p.

Alviola, R., Mänttäri, I., Mäkitie, H., & Vaasjoki, M. 2001. Svecofennian rare element gra nitic pegmatites of the Ostrobothnia region, western Finland; their metamorphic envi ronment and time of intrusion. In: Mäkitie, H. (Ed.). Svecofennian granitic pegmatites (1.86-1.79 Ga) and quartz monzonite (1.87 Ga), and their metamorphic environment in the Seinäjoki region, western Finland. Geological Survey of Finland, Special Paper 30, 9–29.

Ayers, J. C., Miller, C., Gorisch, B., & Milleman, J. 1999. Textural development of monazite during high-grade metamorphism; hydrothermal growth kinetics, with implications for U, Th-Pb geochronology. American Mineralogist 84, 1766–1780.

Axelsson, E., Pape, J., Berndt, J., Corfu, F., Mezger, K., & Raith, M. M. 2018. Rutile R632–A new natural reference material for U-Pb and Zr determination. Geostandards and Geoanalytical Research 42, 319–338.

Balan, E., Neuville, D. R., Trocellier, P., Fritsch, E., Muller, J. P., & Calas, G. 2001. Metamictization and chemical durability of detrital zircon. American Mineralogist 86, 1025–1033.

Barnicoat, A. C., Fare, R. J., Groves, D. I., & McNaughton, N. J. 1991. Synmetamorphic lode-gold deposits in high-grade Archean settings. Geology 19, 921–924.

Bedrock of Finland – DigiKP200. Digital map database (electronic resource). Geological Survey of Finland (referred 21.2.2025).

Belousova, E.A., Griffin, W.L., O'Reilly, S.Y. 2005: Zircon crystal morphology, trace element signatures and Hf isotope composition as a tool for petrogenetic modelling: examples from eastern Australian granitoids. Journal of Petrology 47, 329–353.

Bloem, E. J. 1994. Structural controls, alteration history and genesis of Archaean gold deposits near Southern Cross, Yilgarn Block, Western Australia. Doctoral dissertation, University of Western Australia.

Budzyń, B., Sláma, J., Corfu, F., Crowley, J., Schmitz, M., Williams, M. L., Jercinovic, M. J., Kozub-Budzyń, G. A., Konečny, P., Rzepa, G., & Włodek, A. 2021. TS-Mnz – a new monazite age reference material for U-Th-Pb microanalysis. Chemical Geology 572, 120–195.

Cassidy, K. F. 1992. Archaean granitoid-hosted gold deposits in greenschist to amphibolite facies terrains: A high PT to low PT depositional continuum equivalent to greenstone-hosted deposits. Doctoral dissertation, University of Western Australia.

Cherniak, D. J. 2000. Pb diffusion in rutile. Contributions to Mineralogy and Petrology 139, 198–207.

Corfu, F., Hanchar, J. M., Hoskin, P. W., & Kinny, P. 2003. Atlas of zircon textures. Reviews in Mineralogy and Geochemistry 53, 469–500.

Daly, J. S., Balagansky, V. V., Timmerman, M. J., & Whitehouse, M. J. 2006. The Lapland-Kola orogen: Palaeoproterozoic collision and accretion of the northern Fennoscandian lithosphere. Geological Society of London, Memoirs 32, 579–598.

Dickin, A.P. 2018. Radiogenic Isotope Geology, 3rd Edition. Cambridge University Press. 492 p.

Ehlers, C., Lindroos, A., & Selonen, O. 1993. The late Svecofennian granite-migmatite zone of southern Finland—a belt of transpressive deformation and granite emplacement. Precambrian Research 64, 295–309.

Eilu, P. K., Mathison, C., Groves, D., & Allardyce, W. 1999. Atlas of alteration assemblages, styles and zoning in orogenic lode-gold deposits in a variety of host rock and metamorphic settings. Geology & Geophysics Department (Centre for Strategic Mineral Deposits) & UWA Extension, The University of Western Australia, Publication 30, 50 p.

Eilu, P., Sorjonen-Ward, P., Nurmi, P., & Niiranen, T. 2003. A review of gold mineralization styles in Finland. Economic Geology 98, 1329–1353.

Eilu, P. 2015. Overview on gold deposits in Finland. Mineral deposits of Finland, Elsevier, 377–410.

Eskola, P. 1914. On Petrology of the Orijärvi Region in Southwestern Finland. Bulletin de la Commission Géologique de Finlande 40, 277 p.

Faure, G., Mensing, T. M. 2005. Isotopes: Principles and applications. John Wiley & Sons Inc., 897 p.

Finch, R. J., & Hanchar, J. M. 2003. Structure and chemistry of zircon and zircon-group minerals. Reviews in Mineralogy and Geochemistry 53, 1–25.

Gebre-Mariam, M., Hagemann, S. G., & Groves, D. I. 1995. A classification scheme for epigenetic Archaean lode-gold deposits. Mineralium Deposita 30, 408–410.

Ghent University. 2025. Laser ablation-ICP-MS. https://www.ams.ugent.be/laser-ablation-icp-ms. Visited 28.1.2025.

Goldfarb, R. J., Groves, D. I., & Gardoll, S. 2001. Orogenic gold and geologic time: a global synthesis. Ore Geology Reviews 18, 1–75.

Goldfarb, R. J., & Groves, D. I. 2015. Orogenic gold: Common or evolving fluid and metal sources through time. Lithos 233, 2–26.

Griffiths, J. 2008. A brief history of mass spectrometry. Analytical Chemistry 80, 5678–5683.

Groves, D. I., Goldfarb, R. J., Gebre-Mariam, M., Hagemann, S. G., & Robert, F. 1998. Orogenic gold deposits: a proposed classification in the context of their crustal distribution and relationship to other gold deposit types. Ore Geology Reviews 13, 7–27.

Groves, D., Condie, K. C., Goldfarb, R. J., Hronsky, J. M. A., & Vielreicher, R. 2005. Secular changes in global tectonic processes and their influence on the temporal distribution of gold-bearing mineral deposits. Economic Geology 100, 203–224.

Groves, D. I., Santosh, M., Goldfarb, R. J., & Zhang, L. 2018. Structural geometry of orogenic gold deposits: Implications for exploration of world-class and giant deposits. Geoscience Frontiers 9, 1163–1177.

Grönholm, S., Kärkkäinen, N. Wiik, J. 2005. The Halikko Kultanummi prospect – a new type of gold mineralization in the high-grade gneiss terrain of southwestern Finland. In: Autio, S. (Eds.) Geological Survey of Finland, Current Research 2003 – 2004. Geological Survey of Finland, Special Paper 38, 15 – 23.

Grönholm, S. & Kärkkäinen, N. 2006. Tutkimustyöselostus malmitutkimuksista Halikon Kultanummen valtauksella, kaivosrekisteri n:o 7395/1. Geological Survey of Finland, Report M06/2021/2006/1/10. 21 p. [In Finnish]

Hanski, E., & Huhma, H. 2005. Central Lapland greenstone belt. Elsevier, Developments in Precambrian Geology 14, 139–193.

Hanski, E., & Melezhik, V. A. 2013. Litho- and chronostratigraphy of the Paleoproterozoic Karelian formations. In: Melezhik, V., Prave, A.R., Fallick, A.E., Kump, L.R., Strauss, H., Lepland, A. & Hanski, E.J. (Eds.). The Palaeoproterozoic of Fennoscandia as Context for the Fennoscandian Arctic Russia – Drilling Early Earth Project, Springer-Verlag, 39–110.

Hedenquist, J. W., Arribas, A., & Gonzalez-Urien, E. 2000. Exploration for epithermal gold deposits. SEG Reviews 13, 245–277.

Hirata, T., & Nesbitt, R. W. 1995. U-Pb isotope geochronology of zircon: Evaluation of the laser probe-inductively coupled plasma mass spectrometry technique. Geochimica et Cosmochimica Acta 59, 2491–2500.

Horn, I., Rudnick, R. L., & McDonough, W. F. 2000. Precise elemental and isotope ratio determination by simultaneous solution nebulization and laser ablation-ICP-MS: application to U–Pb geochronology. Chemical Geology 164, 281–301.

Hoskin, P. W., & Schaltegger, U. 2003. The composition of zircon and igneous and metamorphic petrogenesis. Reviews in Mineralogy and Geochemistry 53, 27–62.

Huhma, H., Mänttäri, I., Peltonen, P., Kontinen, A., Halkoaho, T., Hanski, E., Hokkanen, T., Hölttä, P., Juopperi, H., Konnunaho, J., Lahaye, Y., Luukkonen, E., Pietikäinen, K., Pulkkinen, A., Sorjonen-Ward, P., Vaasjoki, P., Whitehouse, M. 2012: The age of the Archaean greenstone belts in Finland. Geological Survey of Finland, Special Paper 54, 74–175.

Högdahl, K., Andersson, U. B., & Eklund, O. 2004. The Transscandinavian Igneous Belt (TIB) in Sweden: a review of its character and evolution. Geological Survey of Finland, Special Paper 37, 123 p.

Hölttä, P. & Heilimo, E. 2017. Metamorphic map of Finland. Geological Survey of Finland, Special Paper 60, 77−128

Hölttä, P., Huhma, H., Mänttäri, I. and Paavola, J. 2000. P–T–t development of Archean granulites in Varpaisjärvi, Central Finland: II. Dating of high-grade metamorphism with the U–Pb and Sm–Nd methods. Lithos 50, 121−136.

Iana, C., & Figueiredo, I. 2023. Saturn U-Th-Pb. Geochemistry laboratory of Universidade Federal de Ouro Preto, Brazil.

John, D., Vikre, P. G., du Bray, E. A., Blakely, R. J., Fey, D. L., Rockwell, B. W., Mauk, J. L., Anderson, E. D., & Graybeal, F. 2018. Descriptive models for epithermal gold-silver deposits. U. S. Geological Survey, Scientific Investigations Report 2010-5070-Q, 247 p.

Kara, J., Leskelä, T., Väisänen, M., Skyttä, P., Lahaye, Y., Tiainen, M., & Leväniemi, H. 2021. Early Svecofennian rift-related magmatism: Geochemistry, U-Pb-Hf zircon isotope data and tectonic setting of the Au-hosting Uunimäki gabbro, SW Finland. Precambrian Research 364, 106364.

Kara, J., Manninen, J., Skyttä, P., Väisänen, M., O'Brien, H., Cutts, K., & Nikkola, P. 2025. Age and structural evolution of the orogenic gold deposits in Kullaa, SW Finland: Implications for fluid activity and gold precipitation during evolving orogeny. Precambrian Research 425, 107828.

Koistinen, T., Stephens, M.B., Bogatchev, V., Nordgulen, Ø., Wennerström, M. and Korhonen, J. 2001. Geological map of the Fennoscandian Shield, scale 1 : 2 000 000. Geological Surveys of Finland, Norway and Sweden and the North-West Department of Natural Resources of Russia.

Korja, A., Lahtinen, R., & Nironen, M. 2006. The Svecofennian orogen: a collage of microcontinents and island arcs. Geological Society of London, Memoirs 32, 561–578.

Kähkönen, Y., 2005. Svecofennian supracrustal rocks. In: Lehtinen, M., Nurmi, P.A., Rämö, O.T. (Eds.), Precambrian Geology of Finland – Key to the Evolution of the Fennoscandian Shield. Elsevier B.V., Amsterdam, 343–406.

Lahtinen, R., Korja, A., Nironen, M., 2005. Paleoproterozoic tectonic evolution. In: Lehtinen, M., Nurmi, P.A., Rämö, O.T. (Eds.), Precambrian Geology of Finland – Key to the Evolution of the Fennoscandian Shield. Elsevier B.V., Amsterdam, 481–532.

Lahtinen, R., Korja, A., Nironen, M., & Heikkinen, P. 2009. Palaeoproterozoic accretionary processes in Fennoscandia. Geological Society of London, Special Publications 318, 237–256.

Lindgren, W. 1933. Mineral Deposits, 4th ed. McGraw Hill, New York and London, 930 p.

Ludwig, K.R. 2003: User's manual for Isoplot/Ex, Version 3.00. A geochronological toolkit for Microsoft Excel. Berkeley Geochronology Center, Special Publication 4, 75 p.

Luukkonen, A. E. 1994. Main geological features, metallogeny and hydrothermal alteration phenomena of certain gold and gold-tin-tungsten prospects in southern Finland. Geological Survey of Finland, Bulletin 377, 153 p.

Luvizotto, G. L., Zack, T., Meyer, H. P., Ludwig, T., Triebold, S., Kronz, A., Münker, C., Stockli, D. F., Prowatke, S., Klemme, S., Jacob, D. E., & von Eynatten, H. 2009. Rutile crystals as potential trace element and isotope mineral standards for microanalysis. Chemical Geology 261, 346–369.

Meinhold, G. 2010. Rutile and its applications in earth sciences. Earth-Science Reviews 102, 1–28.

Meldrum, A., Boatner, L. A., Weber, W. J., & Ewing, R. C. 1998. Radiation damage in zircon and monazite. Geochimica et Cosmochimica Acta 62, 2509–2520.

Mezger, K., Hanson, G. N., & Bohlen, S. R. 1989. High-precision U-Pb ages of metamorphic rutile: application to the cooling history of high-grade terranes. Earth and Planetary Science Letters 96, 106–118.

McCuaig, T. C., & Kerrich, R. 1998. P—T—t—deformation—fluid characteristics of lode gold deposits: evidence from alteration systematics. Ore Geology Reviews 12, 381–453.

Ni, Y., Hughes, J. M., & Mariano, A. N. 1995. Crystal chemistry of the monazite and xenotime structures. American Mineralogist 80, 21–26.

Nier, A. O. 1940. A mass spectrometer for routine isotope abundance measurements. Review of Scientific Instruments 11, 212–216.

Nironen, M. 1997. The Svecofennian Orogen: a tectonic model. Precambrian Research 86, 21–44.

Nironen, M. 2017. Guide to the geological map of Finland–Bedrock 1: 1 000 000. Geological Survey of Finland, Special Paper 60, 41–76.

Overstreet, W. C. 1967. The geologic occurrence of monazite: a review of the distribution of monazite and of the geologic controls affecting the amount of thorium in monazite. U.S. Geological Survey Professional Paper 530, 327 p.

Parrish, R. R. 1990. U–Pb dating of monazite and its application to geological problems. Canadian Journal of Earth Sciences 27, 1431–1450.

Patchett, J., & Kouvo, O. 1986. Origin of continental crust of 1.9–1.7 Ga age: Nd isotopes and U-Pb zircon ages in the Svecokarelian terrain of South Finland. Contributions to Mineralogy and Petrology 92, 1–12.

Phillips, G. N., & Powell, R. 2009. Formation of gold deposits: Review and evaluation of the continuum model. Earth-Science Reviews 94, 1–21.

Poitrasson, F., Chenery, S., & Bland, D. J. 1996. Contrasted monazite hydrothermal alteration mechanisms and their geochemical implications. Earth and Planetary Science Letters 145, 79–96.

Reed, M. H. 1997. Hydrothermal alteration and its relationship to ore fluid composition. Geochemistry of Hydrothermal Ore Deposits, 303–366.

Robinson, K., Gibbs, G. V., & Ribbe, P. H. 1971. The structure of zircon: a comparison with garnet. American Mineralogist: Journal of Earth and Planetary Materials 56, 782–790.

Roy, A., Roy, S. K., & Ramchandra, H. M. 2023. Origin of metasomatic sillimanite in ductile shear zones: An example from the Proterozoic Sakoli Fold Belt, Bastar Craton, central India. Journal of Earth System Science 132, 1–17.

Ruotoistenmäki, T. 2004. Kultanummi ja Korvenala-Kaleva-alueen geofysiikan kartoista, rakennetulkintaa ja niiden assosioitumisesta kultakriittisiin kohteisiin. Julkaisematon työraportti, Geologian tutkimuskeskus, 4 p. [in Finnish]

Rutherford, E., Soddy, F. 1902. The cause and nature of radioactivity: Pt. I. Philosophical Magazine 4, 370−396.

Saalmann, K., Mänttäri, I., Ruffet, G., & Whitehouse, M. J. 2009. Age and tectonic framework of structurally controlled Palaeoproterozoic gold mineralization in the Häme belt of southern Finland. Precambrian Research 174, 53–77.

Saalmann, K., Mänttäri, I., Peltonen, P., Whitehouse, M. J., Grönholm, P., & Talikka, M. 2010. Geochronology and structural relationships of mesothermal gold mineralization in the Palaeoproterozoic Jokisivu prospect, southern Finland. Geological Magazine 147, 551−569.

Schoene, B. 2014. U–Th–Pb geochronology. Treatise on Geochemistry 4, 341−378.

Schärer, U. 1984. The effect of initial ^{230}Th disequilibrium on young U-Pb ages: the Makalu case, Himalaya. Earth and Planetary Science Letters 67, 191−204.

Suominen, V. 1991. The chronostratigraphy of southwestern Finland with special reference to Postjotnian and Subjotnian diabases. Geological Survey of Finland, Bulletin 356, 100 p.

Sillitoe, R. H. 2010. Porphyry copper systems. Economic geology 105, 3−41.

Talikka, M., & Manttari, I. 2005. Pukala intrusion, its age and connection to hydrothermal alteration in Orivesi, southwestern Finland. Geological Society of Finland, Bulletin 77, 165−180.

Taylor, B. E. 2007. Epithermal gold deposits. In: Mineral Deposits of Canada: A synthesis of major deposit-types, district metallogeny, the evolution of geological provinces, and exploration methods: Geological Association of Canada, Mineral Deposits Division, Special Publication 5, 113−139.

Tera, F., & Wasserburg, G.J. 1972. U-Th-Pb systematics in three Apollo 14 basalts and the problem of initial Pb in lunar rocks. Earth and Planetary Science Letters 14, 281−304.

Teräs, O., Nikkilä, K., Mikkola, P., Kotilainen, A., Eklund, O., & Rämö, T. 2025. Paleoproterozoic post-orogenic magmatism in southern Finland; geochemical, geochronological and Sr-Nd isotopic constraints on origin and magmatic evolution. Geological Society of Finland, Bulletin 96, 135−160.

Thompson, A. B. 1982. Dehydration melting of pelitic rocks and the generation of H_2O – undersaturated granitic liquids. American Journal of Science 282, 1567–1595.

Tilton, G. R. 1960. Volume diffusion as a mechanism for discordant lead ages. Journal of Geophysical Research 65, 2933–2945.

Tomkins, A. G. 2013. On the source of orogenic gold. Geology 41, 1255–1256.

Vaasjoki, M., Korsman, K., Koistinen, T., 2005. Overview. In: Lehtinen, M., Nurmi, P.A., Rämö, O.T. (Eds.), The Precambrian Geology of Finland – Key to the Evolution of the Fennoscandian Shield. Elsevier B.V., Amsterdam, pp. 1–18.

Van Achterbergh, E., Ryan C., Jackson, S. and Griffin W. 2001. Data reduction software for LA-ICP-MS. In: Sylvester, P. (Ed.), Laser-Ablation ICPMS in the Earth Sciences – Principles and applications, Mineralogical Association of Canada short course series 29, St John, Newfoundland, 239−243.

Vanhala, H. 2002. Halikon Kultanummen IP-luotausten tulkinta. Geologian tutkimuskeskus, työraportti, 4 p. 5 appendixes. [in Finnish]

Vry, J. K., & Baker, J. A. 2006. LA-MC-ICPMS Pb–Pb dating of rutile from slowly cooled granulites: confirmation of the high closure temperature for Pb diffusion in rutile. Geochimica et Cosmochimica Acta 70, 1807−1820.

Väisänen, M., Hölttä, P. 1999. Structural and metamorphic evolution of the Turku migmatite complex, southwestern Finland. Geological Society of Finland, Bulletin 71, 177−218.

Väisänen, M., Manttari, I., Kriegsman, L. M., & Holtta, P. 2000. Tectonic setting of post-collisional magmatism in the Palaeoproterozoic Svecofennian Orogen, SW Finland. Lithos 54, 63−81.

Väisänen, M., & Mänttäri, I. 2002. 1.90−1.88 Ga arc and back-arc basin in the Orijärvi area, SW Finland. Geological Society of Finland, Bulletin 74, 185−214.

Väisänen, M., Mänttäri, I., & Hölttä, P. 2002. Svecofennian magmatic and metamorphic evolution in southwestern Finland as revealed by U-Pb zircon SIMS geochronology. Precambrian Research 116, 111−127.

Väisänen, M., & Kirkland, C. L. 2008. U-Th-Pb zircon geochronology on igneous rocks in the Toija and Salittu Formations, Orijärvi area, southwestern Finland: constraints on the age of volcanism and metamorphism. Geological Society of Finland, Bulletin 80, 73−87.

Weber, W. J., Ewing, R. C., & Wang, L. M. 1994. The radiation-induced crystalline-to-amorphous transition in zircon. Journal of Materials Research 9, 688−698.

Wetherill, G.W. 1956. Discordant uranium-lead ages. Transactions American Geophysical Union 37, 320−326.

White, N. C., & Hedenquist, J. W. 1995. Epithermal gold deposits: styles, characteristics and exploration. SEG Newsletter 23, 1–13.

Wiik, J. 2004. Beskrivning av en guldmineralisering i Kultanummi, Halikko SV-Finland. Pro gradu- avhandling, Åbo Akademi, 50 p. [in Swedish]

Zack, T., von Eynatten, H., & Kronz, A. 2004. Rutile geochemistry and its potential use in quantitative provenance studies. Sedimentary Geology 171, 37−58.

Zack, T., & Kooijman, E. 2017. Petrology and geochronology of rutile. Reviews in Mineralogy and Geochemistry 83, 443−467.

Zhu, X. K., & O'nions, R. K. 1999. Zonation of monazite in metamorphic rocks and its implications for high temperature thermochronology: a case study from the Lewisian terrain. Earth and Planetary Science Letters 171, 209−220.

Appendix 1. Zircon U-Pb data

Sample	U (ppm)	Th/U	207Pb/206Pb	2σ	207Pb/235U	2σ	206Pb/238U	2σ	P	% Concordance	206Pb/238U (Ma)	2σ	207Pb/235U (Ma)	2σ	207Pb/206Pb (Ma)	2σ	comment
NMHE-2024-04-74	113	0.70	0.1117	0.88	5.1491	1.55	0.3343	1.27	0.82	102	1859	21	1844	13	1828	16	younger pop.
NMHE-2024-04-80	136	0.59	0.1120	0.67	5.1448	1.20	0.3332	0.99	0.83	101	1854	16	1844	10	1832	12	younger pop.
NMHE-2024-17.2b-71	333	1.09	0.1122	0.96	5.2249	1.59	0.3379	1.26	0.80	102	1876	21	1857	14	1835	18	younger pop.
NMHE-2024-04-89	223	1.03	0.1123	0.92	5.1576	1.43	0.3332	1.10	0.77	101	1854	18	1846	12	1837	17	younger pop.
NMHE-2024-15.1a-756	114	0.11	0.1124	1.06	5.1203	1.77	0.3304	1.42	0.80	100	1840	23	1840	15	1839	19	younger pop.
NMHE-2024-15.1a-1295	257	0.15	0.1126	1.10	5.1385	1.99	0.3309	1.66	0.84	100	1843	27	1843	17	1843	20	younger pop.
NMHE-2024-15.1a-357	302	0.54	0.1127	0.55	5.1598	1.32	0.3321	1.20	0.91	100	1849	19	1846	11	1843	10	younger pop.
NMHE-2024-15.1a-1165	474	0.14	0.1127	0.85	5.1467	1.50	0.3312	1.23	0.83	100	1844	20	1844	13	1844	15	younger pop.
NMHE-2024-17.2b-65	323	1.18	0.1128	0.85	5.2163	1.31	0.3353	1.00	0.77	101	1864	16	1855	11	1846	15	younger pop.
NMHE-2024-17.2b-78	62	1.12	0.1129	0.82	5.1936	1.48	0.3336	1.23	0.83	100	1856	20	1852	13	1847	15	younger pop.
NMHE-2024-04-821	986	0.42	0.1130	0.70	5.1768	1.26	0.3324	1.04	0.83	100	1850	17	1849	11	1848	13	younger pop.
NMHE-2024-15.1a-1002	251	0.14	0.1130	0.97	5.1911	1.75	0.3332	1.45	0.83	100	1854	24	1851	15	1848	18	younger pop.
NMHE-2024-17.2b-2227	784	0.35	0.1131	1.13	5.2127	2.33	0.3343	2.03	0.87	100	1859	33	1855	20	1850	21	younger pop.
NMHE-2024-15.1a-141	926	0.29	0.1135	0.91	5.2989	1.77	0.3385	1.52	0.86	101	1879	25	1869	15	1857	17	younger pop.
NMHE-2024-04-573	469	0.40	0.1140	0.55	5.2452	1.13	0.3338	0.99	0.87	100	1857	16	1860	10	1864	10	younger pop.
NMHE-2024-04-451	272	0.39	0.1140	1.01	5.2898	1.57	0.3365	1.20	0.76	100	1870	20	1867	14	1865	18	younger pop.
NMHE-2024-04-71	775	0.32	0.1140	0.67	5.2749	1.21	0.3355	1.01	0.84	100	1865	16	1865	10	1865	12	younger pop.
NMHE-2024-15.1a-621	351	0.27	0.1141	1.09	5.3557	1.56	0.3406	1.12	0.72	101	1889	18	1878	14	1865	20	younger pop.
NMHE-2024-15.1a-274	593	0.42	0.1141	0.85	5.2908	2.31	0.3362	2.14	0.93	100	1869	35	1867	20	1866	16	younger pop.
NMHE-2024-17.2b-82	788	0.26	0.1141	0.67	5.2918	1.15	0.3363	0.94	0.82	100	1869	15	1868	10	1866	12	younger pop.
NMHE-2024-04-876	305	0.23	0.1143	0.95	5.3049	1.54	0.3367	1.22	0.79	100	1871	20	1870	13	1869	17	younger pop.
NMHE-2024-04-1104	295	0.21	0.1144	0.85	5.3071	1.30	0.3364	0.99	0.76	100	1869	16	1870	11	1871	15	main pop.
NMHE-2024-04-428	756	0.21	0.1145	1.18	5.3282	2.43	0.3375	2.12	0.87	100	1875	35	1873	21	1873	22	main pop.

NMHE-2024-04-666	369	0.26	0.1147	0.90	5.3541	1.44	0.3384	1.12	0.78	100	1879	18	1878	12	1876	16	main pop.
NMHE-2024-15.1a-416	358	0.21	0.1147	0.80	5.3668	1.50	0.3394	1.27	0.85	100	1884	21	1880	13	1875	15	main pop.
NMHE-2024-04-981	629	0.27	0.1148	1.01	5.5003	1.57	0.3476	1.20	0.76	102	1923	20	1901	14	1877	18	main pop.
NMHE-2024-04-1029	577	0.28	0.1148	0.96	5.3532	1.80	0.3382	1.52	0.85	100	1878	25	1877	16	1877	17	main pop.
NMHE-2024-15.1a-456	288	0.40	0.1148	0.67	5.3472	1.29	0.3377	1.10	0.86	100	1876	18	1876	11	1878	12	main pop.
NMHE-2024-15.1a-615	159	0.39	0.1149	0.93	5.3549	1.68	0.3381	1.40	0.83	100	1878	23	1878	15	1878	17	main pop.
NMHE-2024-15.1a-173	213	0.24	0.1149	1.08	5.3573	1.47	0.3381	1.00	0.68	100	1878	16	1878	13	1879	20	main pop.
NMHE-2024-17.2b-49	177	0.38	0.1150	0.61	5.6832	0.94	0.3584	0.71	0.76	105	1974	12	1929	8	1881	11	main pop.
NMHE-2024-17.2b-525	261	0.33	0.1150	0.63	5.433	1.00	0.3425	0.78	0.78	101	1899	13	1890	9	1881	11	main pop.
NMHE-2024-04-507	261	0.29	0.1151	0.69	5.4011	1.33	0.3404	1.13	0.85	100	1889	19	1885	11	1881	13	main pop.
NMHE-2024-04-283	188	0.38	0.1151	0.78	5.4723	1.17	0.3448	0.87	0.75	101	1910	14	1896	10	1882	14	main pop.
NMHE-2024-15.1a-684	270	0.28	0.1151	1.04	5.376	1.63	0.3388	1.25	0.77	100	1881	21	1881	14	1882	19	main pop.
NMHE-2024-04-636	520	0.50	0.1152	0.79	5.5827	1.62	0.3514	1.41	0.87	103	1941	24	1913	14	1884	14	main pop.
NMHE-2024-04-885	196	0.28	0.1153	0.67	5.4017	1.27	0.3398	1.08	0.85	100	1886	18	1885	11	1885	12	main pop.
NMHE-2024-04-319	166	0.32	0.1154	0.79	5.4146	1.19	0.3403	0.90	0.75	100	1888	15	1887	10	1886	14	main pop.
NMHE-2024-15.1a-1054	164	0.18	0.1154	0.82	5.4514	1.22	0.3425	0.91	0.74	101	1899	15	1893	11	1887	15	main pop.
NMHE-2024-04-462	346	0.35	0.1155	1.04	5.1725	1.85	0.3248	1.53	0.83	96	1813	24	1848	16	1888	19	main pop.
NMHE-2024-15.1a-1165	628	0.08	0.1156	0.73	5.4172	1.91	0.34	1.76	0.92	100	1887	29	1888	17	1889	13	main pop.
NMHE-2024-17.2b-307	355	0.34	0.1156	0.66	5.456	1.37	0.3422	1.21	0.88	100	1897	20	1894	12	1890	12	main pop.
NMHE-2024-04-901	405	0.48	0.1158	1.64	5.462	2.94	0.3421	2.44	0.83	100	1897	40	1895	26	1893	30	main pop.
NMHE-2024-17.2b-2542	375	0.16	0.1158	0.91	5.2638	1.44	0.3297	1.11	0.77	97	1837	18	1863	12	1893	17	main pop.
NMHE-2024-04-1113	148	0.30	0.1161	0.83	5.4784	1.21	0.3422	0.89	0.73	100	1897	15	1897	11	1898	15	main pop.
NMHE-2024-04-89	186	1.25	0.1161	0.98	5.496	1.60	0.3432	1.26	0.79	100	1902	21	1900	14	1898	18	main pop.
NMHE-2024-04-373	332	0.37	0.1162	1.17	5.4823	1.69	0.3422	1.22	0.72	100	1897	20	1898	15	1899	21	main pop.
NMHE-2024-15.1a-950	384	0.39	0.1162	1.05	5.1414	1.75	0.321	1.41	0.80	94	1795	22	1843	15	1898	19	main pop.
NMHE-2024-15.1a-745	158	0.29	0.1171	1.70	5.9671	2.64	0.3694	2.02	0.77	106	2027	35	1971	23	1913	31	inherited pop.
NMHE-2024-15.1a-1200	531	0.40	0.1171	1.28	5.3924	2.23	0.334	1.83	0.82	97	1858	30	1884	19	1912	23	inherited pop.
NMHE-2024-17.2b-2564	495	0.38	0.1171	1.17	5.671	2.32	0.3512	2.00	0.86	101	1940	34	1927	20	1913	21	inherited pop.
NMHE-2024-04-949	128	0.43	0.1182	1.09	5.6963	1.61	0.3495	1.19	0.74	100	1932	20	1931	14	1930	20	inherited pop.

NMHE-2024-17.2b-1593	250	0.31	0.1182	0.58	5.4174	1.16	0.3325	1.00	0.87	96	1851	16	1888	10	1929	10	inherited pop.
NMHE-2024-04-635	309	0.36	0.1193	0.56	5.7907	1.84	0.3519	1.75	0.95	100	1944	30	1945	16	1946	10	inherited pop.
NMHE-2024-04-395	182	0.68	0.1202	0.60	5.9957	0.97	0.3618	0.77	0.79	102	1991	13	1975	9	1959	11	inherited pop.
NMHE-2024-04-493	100	0.46	0.1204	0.99	5.9014	1.44	0.3555	1.04	0.72	100	1961	18	1961	13	1962	18	inherited pop.
NMHE-2024-15.1a-278	307	0.27	0.1207	0.63	5.8609	1.06	0.3523	0.85	0.81	99	1945	14	1956	9	1966	11	inherited pop.
NMHE-2024-17.2b-1980	363	0.46	0.1231	0.85	6.2228	1.39	0.3666	1.10	0.79	101	2013	19	2008	12	2003	17	inherited pop.
NMHE-2024-15.1a-1046	80	0.44	0.1247	1.40	6.5712	2.16	0.3822	1.65	0.76	103	2087	29	2056	19	2025	26	inherited pop.
NMHE-2024-15.1a-535	164	0.50	0.1248	0.99	6.4524	1.42	0.375	1.01	0.72	101	2053	18	2039	13	2027	17	inherited pop.
NMHE-2024-15.1a-204	571	0.13	0.1252	1.21	6.4096	4.16	0.3714	3.98	0.96	100	2036	70	2034	37	2032	21	inherited pop.
NMHE-2024-04-596	74	0.38	0.1257	1.56	6.5272	2.63	0.3767	2.12	0.81	101	2061	38	2050	24	2038	27	inherited pop.
NMHE-2024-17.2b-3136	344	0.48	0.1259	0.85	6.9906	1.35	0.4028	1.05	0.78	106	2182	20	2110	12	2041	15	inherited pop.
NMHE-2024-04-623	115	0.36	0.1271	0.91	6.6098	1.25	0.3773	0.86	0.69	100	2064	15	2061	11	2058	16	inherited pop.
NMHE-2024-15.1a-482	333	0.14	0.1307	0.77	6.9673	1.52	0.3867	1.31	0.86	100	2108	24	2107	14	2107	14	inherited pop.
NMHE-2024-17.2b-66	283	0.17	0.1544	1.04	9.1844	2.55	0.4314	2.33	0.91	96	2312	45	2357	24	2396	18	inherited pop.
NMHE-2024-17.2b-940	32	0.25	0.1616	1.64	9.9693	2.18	0.4474	1.44	0.66	96	2384	29	2432	20	2472	28	inherited pop.
NMHE-2024-17.2b-3092	72	0.70	0.1691	1.18	10.7	1.59	0.459	1.06	0.67	95	2435	22	2497	15	2549	20	inherited pop.
NMHE-2024-17.2b-2538	106	0.18	0.1710	1.52	11.6966	2.10	0.4962	1.45	0.69	101	2597	31	2580	20	2567	25	inherited pop.
NMHE-2024-17.2b-2533	436	0.37	0.1746	1.12	13.3637	1.66	0.5552	1.23	0.74	109	2847	28	2706	16	2602	19	inherited pop.
NMHE-2024-04-874	50	0.31	0.1874	0.92	13.5588	1.29	0.5247	0.90	0.70	100	2719	20	2719	12	2719	15	inherited pop.

Appendix 2. Monazite U-Pb data

Sample	207Pb/206Pb	2σ	207Pb/235U	2σ	206Pb/238U	2σ	P	206Pb/238U (Ma)	2σ	207Pb/235U (Ma)	2σ	207Pb/206Pb (Ma)	2σ	comment
NMHE-2024-13b-192c	0.1081	1.21	4.6557	2.08	0.3124	1.69	0.81	1753	26	1759	18	1767	22	hydroth. pop.
NMHE-2024-17.2a-3657	0.1081	0.86	4.6656	1.98	0.3131	1.79	0.90	1756	28	1761	17	1767	16	hydroth. pop.
NMHE-2024-17.2a-2756	0.1082	1.93	4.6958	2.74	0.3148	1.95	0.71	1765	30	1767	23	1769	36	hydroth. pop.
NMHE-2024-17.2a-2981	0.1084	1.54	4.7068	2.38	0.3150	1.81	0.76	1765	28	1768	20	1772	29	hydroth. pop.
NMHE-2024-04-764	0.1086	0.84	4.8651	1.59	0.3249	1.35	0.85	1814	21	1796	13	1776	15	hydroth. pop.
NMHE-2024-15.1a-10	0.1086	0.90	4.9512	1.70	0.3308	1.44	0.85	1842	23	1811	15	1775	17	hydroth. pop.
NMHE-2024-17.2a-2430	0.1086	0.78	4.7973	1.56	0.3204	1.35	0.87	1792	21	1784	13	1776	14	hydroth. pop.
NMHE-2024-04-1063	0.1087	0.76	4.8713	1.55	0.3250	1.35	0.87	1814	21	1797	13	1778	14	hydroth. pop.
NMHE-2024-04-1010	0.1087	1.02	4.6606	2.00	0.3110	1.72	0.86	1746	26	1760	17	1777	19	hydroth. pop.
NMHE-2024-13b-192b	0.1087	0.89	4.8329	1.83	0.3224	1.60	0.88	1801	25	1791	16	1778	16	hydroth. pop.
NMHE-2024-15.1a-575	0.1087	1.00	4.7876	1.94	0.3194	1.66	0.86	1787	26	1783	16	1778	19	hydroth. pop.
NMHE-2024-04-1005	0.1088	0.58	4.8127	1.36	0.3208	1.23	0.91	1793	19	1787	12	1780	11	hydroth. pop.
NMHE-2024-15.1a-83	0.1088	0.58	4.7454	1.39	0.3163	1.26	0.91	1772	20	1775	12	1779	11	hydroth. pop.
NMHE-2024-17.2a-1147	0.1088	0.78	4.6896	1.82	0.3127	1.64	0.90	1754	25	1765	15	1779	14	hydroth. pop.
NMHE-2024-04-320	0.1089	0.87	4.7636	1.53	0.3173	1.27	0.83	1777	20	1779	13	1781	16	hydroth. pop.
NMHE-2024-04-961	0.1089	1.17	4.8822	2.02	0.3251	1.65	0.82	1815	26	1799	17	1781	22	hydroth. pop.
NMHE-2024-04-1060	0.1089	1.10	4.8385	2.01	0.3221	1.68	0.84	1800	27	1792	17	1782	20	hydroth. pop.
NMHE-2024-15.1a-40	0.1089	0.75	4.8304	1.54	0.3217	1.34	0.87	1798	21	1790	13	1781	14	hydroth. pop.
NMHE-2024-04-1004	0.1090	0.90	4.9087	1.73	0.3266	1.47	0.85	1822	23	1804	15	1783	17	hydroth. pop.
NMHE-2024-04-736	0.1090	0.74	4.8603	1.51	0.3233	1.31	0.87	1806	21	1795	13	1783	14	hydroth. pop.
NMHE-2024-04-959	0.1090	0.76	5.1196	1.55	0.3406	1.35	0.87	1890	22	1839	13	1783	14	hydroth. pop.
NMHE-2024-17.2a-3847	0.1090	1.01	4.8275	1.74	0.3213	1.42	0.81	1796	22	1790	15	1783	19	hydroth. pop.
NMHE-2024-17.2a-4144	0.1090	1.38	4.9681	2.61	0.3307	2.22	0.85	1842	36	1814	22	1782	26	hydroth. pop.
NMHE-2024-04-377	0.1091	1.04	4.7556	1.85	0.3160	1.53	0.83	1770	24	1777	16	1785	19	hydroth. pop.
NMHE-2024-15.1a-693	0.1091	0.93	4.8224	1.85	0.3206	1.60	0.86	1793	25	1789	16	1784	17	hydroth. pop.
NMHE-2024-04-680	0.1092	0.88	4.8520	1.61	0.3223	1.35	0.84	1801	21	1794	14	1786	16	hydroth. pop.

NMHE-2024-04-641	0.1092	1.16	4.9720	2.09	0.3302	1.74	0.83	1840	28	1815	18	1786	21	hydroth. pop.
NMHE-2024-15.1a-1021	0.1092	1.21	4.8343	1.89	0.3210	1.45	0.77	1795	23	1791	16	1787	22	hydroth. pop.
NMHE-2024-17.2a-3044	0.1092	1.39	4.7514	2.33	0.3157	1.86	0.80	1769	29	1776	20	1786	26	hydroth. pop.
NMHE-2024-17.2a-3022	0.1092	0.96	4.7504	1.68	0.3156	1.38	0.82	1768	21	1776	14	1786	18	hydroth. pop.
NMHE-2024-04-1087	0.1093	0.98	4.9067	1.82	0.3256	1.54	0.84	1817	24	1803	16	1788	18	hydroth. pop.
NMHE-2024-04-369	0.1093	0.99	4.9349	1.71	0.3275	1.39	0.81	1826	22	1808	15	1788	18	hydroth. pop.
NMHE-2024-04-297	0.1093	1.14	4.9308	2.19	0.3272	1.87	0.85	1825	30	1808	19	1788	21	hydroth. pop.
NMHE-2024-04-1009	0.1093	0.97	4.7198	1.87	0.3133	1.59	0.85	1757	25	1771	16	1787	18	hydroth. pop.
NMHE-2024-13b-192	0.1093	1.05	4.7461	2.04	0.3150	1.75	0.86	1765	27	1775	17	1787	19	hydroth. pop.
NMHE-2024-04-1021	0.1094	0.80	4.7457	1.57	0.3145	1.35	0.86	1763	21	1775	13	1790	15	hydroth. pop.
NMHE-2024-13b-311	0.1094	0.94	4.7336	1.75	0.3139	1.47	0.84	1760	23	1773	15	1789	17	hydroth. pop.
NMHE-2024-17.2a-4022	0.1094	1.89	4.6828	2.82	0.3106	2.10	0.74	1744	32	1764	24	1789	35	hydroth. pop.
NMHE-2024-04-513	0.1095	0.98	4.7466	1.74	0.3143	1.44	0.83	1762	22	1776	15	1792	18	hydroth. pop.
NMHE-2024-04-288	0.1096	0.74	4.8939	1.54	0.3240	1.35	0.88	1809	21	1801	13	1792	14	hydroth. pop.
NMHE-2024-04-65	0.1096	0.89	4.7997	1.66	0.3178	1.40	0.85	1779	22	1785	14	1792	16	hydroth. pop.
NMHE-2024-04-453	0.1098	1.03	4.9249	1.66	0.3253	1.31	0.79	1816	21	1807	14	1796	19	hydroth. pop.
NMHE-2024-15.1a-623	0.1098	1.00	4.8872	1.75	0.3228	1.43	0.82	1804	23	1800	15	1796	18	hydroth. pop.
NMHE-2024-17.2a-2423	0.1098	0.64	4.8520	1.40	0.3206	1.24	0.89	1793	20	1794	12	1796	12	hydroth. pop.
NMHE-2024-15.1a-1	0.1099	0.54	4.9694	1.35	0.3279	1.24	0.92	1828	20	1814	12	1798	10	hydroth. pop.
NMHE-2024-15.1a-730	0.1099	0.74	4.9126	1.64	0.3242	1.46	0.89	1810	23	1804	14	1798	14	hydroth. pop.
NMHE-2024-04-459	0.1100	0.80	4.9612	1.61	0.3270	1.40	0.87	1824	22	1813	14	1800	15	hydroth. pop.
NMHE-2024-15.1a-1083	0.1100	0.69	4.8996	1.61	0.3230	1.46	0.91	1805	23	1802	14	1800	13	hydroth. pop.
NMHE-2024-04-605	0.1101	0.84	4.6975	1.80	0.3095	1.59	0.89	1738	24	1767	15	1801	15	hydroth. pop.
NMHE-2024-15.1a-1005	0.1101	0.70	4.9331	1.39	0.3249	1.21	0.87	1814	19	1808	12	1802	13	hydroth. pop.
NMHE-2024-17.2a-2094	0.1101	0.75	4.7786	1.38	0.3148	1.16	0.84	1764	18	1781	12	1801	14	hydroth. pop.
NMHE-2024-04-988	0.1102	0.76	4.9883	1.55	0.3283	1.35	0.87	1830	22	1817	13	1803	14	hydroth. pop.
NMHE-2024-15.1a-576	0.1102	0.93	5.0645	1.59	0.3332	1.29	0.81	1854	21	1830	14	1804	17	hydroth. pop.
NMHE-2024-15.1a-220	0.1102	0.65	4.9162	1.42	0.3237	1.27	0.89	1808	20	1805	12	1802	12	hydroth. pop.
NMHE-2024-04-951	0.1103	0.88	4.9208	1.55	0.3236	1.28	0.83	1808	20	1806	13	1804	16	hydroth. pop.

NMHE-2024-04-393	0.1103	0.94	4.7017	2.00	0.3092	1.76	0.88	1737	27	1768	17	1804	17	hydroth. pop.
NMHE-2024-15.1a-142	0.1103	0.90	4.9404	1.56	0.3249	1.27	0.81	1814	20	1809	13	1804	17	hydroth. pop.
NMHE-2024-04-888	0.1104	0.93	5.0359	1.69	0.3308	1.40	0.83	1842	23	1825	14	1807	17	hydroth. pop.
NMHE-2024-04-297	0.1104	1.55	4.8632	2.60	0.3196	2.08	0.80	1788	33	1796	22	1806	29	hydroth. pop.
NMHE-2024-04-703	0.1104	0.83	4.9004	1.69	0.3218	1.48	0.87	1799	23	1802	14	1807	15	hydroth. pop.
NMHE-2024-15.1a-41	0.1104	0.80	4.8984	1.49	0.3218	1.25	0.84	1798	20	1802	13	1806	15	hydroth. pop.
NMHE-2024-04-277	0.1105	0.88	4.9617	1.64	0.3258	1.38	0.84	1818	22	1813	14	1807	16	hydroth. pop.
NMHE-2024-15.1a-773	0.1105	0.84	4.9641	1.67	0.3258	1.44	0.86	1818	23	1813	14	1808	15	hydroth. pop.
NMHE-2024-17.2a-1652	0.1106	1.00	5.0918	1.64	0.3340	1.30	0.79	1858	21	1835	14	1809	18	hydroth. pop.
NMHE-2024-04-304	0.1107	0.90	5.0103	1.61	0.3283	1.33	0.83	1830	21	1821	14	1811	17	hydroth. pop.
NMHE-2024-15.1a-473	0.1107	0.94	5.2292	2.10	0.3427	1.88	0.89	1900	31	1857	18	1811	17	hydroth. pop.
NMHE-2024-15.1a-906	0.1108	1.04	4.9230	1.74	0.3222	1.40	0.80	1801	22	1806	15	1813	19	hydroth. pop.
NMHE-2024-04-457	0.1110	1.17	5.1554	1.99	0.3368	1.61	0.81	1871	26	1845	17	1816	21	met. peak pop.
NMHE-2024-15.1a-1299	0.1110	0.58	5.0221	1.28	0.3283	1.14	0.89	1830	18	1823	11	1815	11	met. peak pop.
NMHE-2024-17.2a-2089	0.1110	0.72	4.7874	1.43	0.3129	1.23	0.86	1755	19	1783	12	1816	13	met. peak pop.
NMHE-2024-04-803	0.1111	0.79	5.0416	1.63	0.3292	1.42	0.87	1834	23	1826	14	1818	15	met. peak pop.
NMHE-2024-04-694	0.1112	0.98	5.0557	1.60	0.3299	1.26	0.79	1838	20	1829	14	1819	18	met. peak pop.
NMHE-2024-04-942	0.1113	0.85	4.9479	1.53	0.3224	1.27	0.83	1801	20	1811	13	1821	16	met. peak pop.
NMHE-2024-04-873	0.1114	0.84	5.0094	1.60	0.3260	1.36	0.85	1819	22	1821	14	1823	15	met. peak pop.
NMHE-2024-17.2a-3349	0.1142	1.64	5.3566	2.50	0.3401	1.88	0.75	1887	31	1878	22	1868	30	old met. peak pop.
NMHE-2024-15.1a-738	0.1144	0.71	5.2377	1.48	0.3321	1.29	0.88	1848	21	1859	13	1871	13	old met. peak pop.

Appendix 3. Rutile U-Pb data

Sample	207Pb/206Pb	2σ	207Pb/235U	2σ	206Pb/238U	2σ	P	% Concordance	206Pb/238U (Ma)	2σ	207Pb/235U (Ma)	2σ	207Pb/206Pb (Ma)	2σ
NMHE-2024-04-677	0.1073	1.67	4.5505	2.49	0.3076	1.85	0.74	99	1729	28	1740	21	1754	31
NMHE-2024-17.2a-965	0.1075	0.84	4.6645	1.39	0.3146	1.11	0.80	100	1763	17	1761	12	1758	16
NMHE-2024-15.1a-497	0.1077	1.13	4.5798	1.74	0.3085	1.32	0.76	98	1734	20	1746	14	1760	20
NMHE-2024-15.1a-769	0.1077	1.26	4.7548	1.98	0.3203	1.53	0.77	102	1791	24	1777	17	1760	23
NMHE-2024-17.2a-789	0.1077	0.94	4.4274	1.56	0.2981	1.25	0.80	95	1682	19	1718	13	1761	18
NMHE-2024-17.2a-2717	0.1078	1.13	4.6956	1.81	0.3161	1.42	0.78	100	1770	22	1767	15	1762	20
NMHE-2024-17.2a-3294	0.1078	1.33	4.7965	2.17	0.3228	1.72	0.79	102	1803	27	1784	18	1762	24
NMHE-2024-17.2a-3057	0.1078	1.14	4.7203	1.92	0.3176	1.54	0.80	101	1778	24	1771	16	1763	21
NMHE-2024-04-199	0.1078	1.14	4.4426	1.93	0.2989	1.56	0.81	95	1686	23	1720	16	1763	21
NMHE-2024-04-115	0.1079	0.99	4.6733	1.67	0.3140	1.35	0.81	100	1760	21	1763	15	1765	19
NMHE-2024-17.2a-1615	0.1080	0.96	4.5999	1.59	0.3089	1.27	0.80	98	1735	20	1749	13	1766	18
NMHE-2024-17.2a-2147	0.1080	1.12	4.4967	1.72	0.3018	1.30	0.76	96	1700	20	1730	15	1767	22
NMHE-2024-04-1013	0.1081	1.11	4.7441	1.86	0.3182	1.49	0.80	101	1781	23	1775	16	1768	21
NMHE-2024-17.2a-2462	0.1082	1.27	4.4464	1.94	0.2981	1.47	0.76	95	1682	22	1721	16	1769	23
NMHE-2024-17.2a-970	0.1082	1.05	4.8653	1.68	0.3262	1.31	0.78	103	1820	21	1796	14	1769	19
NMHE-2024-17.2a-1507	0.1082	1.08	4.4939	1.51	0.3012	1.06	0.70	96	1697	16	1730	13	1769	20
NMHE-2024-04-804	0.1083	1.45	4.4392	2.10	0.2974	1.52	0.72	95	1678	22	1720	17	1770	26
NMHE-2024-04-1089	0.1083	0.95	4.4700	1.42	0.2994	1.06	0.74	95	1689	16	1725	12	1771	17
NMHE-2024-17.2a-2970	0.1083	1.67	4.9253	2.43	0.3299	1.77	0.73	104	1838	28	1807	21	1771	31
NMHE-2024-17.2a-2674	0.1083	1.09	4.8271	1.67	0.3232	1.26	0.76	102	1806	20	1790	14	1771	20
NMHE-2024-04-950	0.1083	1.59	4.3305	3.27	0.2900	2.86	0.87	92	1641	41	1699	27	1771	30
NMHE-2024-17.2a-2415	0.1083	1.68	5.0225	2.60	0.3363	1.99	0.76	105	1869	32	1823	22	1771	32
NMHE-2024-17.2a-2342	0.1083	1.21	4.6938	1.66	0.3142	1.14	0.69	99	1762	18	1766	14	1772	23
NMHE-2024-17.2a-1568	0.1084	1.06	4.3360	1.74	0.2902	1.38	0.79	92	1643	20	1700	14	1772	19
NMHE-2024-17.2a-2704	0.1084	1.14	4.9127	1.66	0.3287	1.21	0.73	103	1832	19	1804	14	1773	21

NMHE-2024-04-210	0.1085	0.93	4.5720	1.45	0.3057	1.11	0.77	97	1720	17	1744	12	1774	17
NMHE-2024-04-207	0.1085	1.01	4.7322	1.73	0.3163	1.40	0.81	100	1772	22	1773	15	1775	19
NMHE-2024-15.1a-118	0.1086	1.60	4.8718	2.17	0.3255	1.46	0.67	102	1817	23	1797	18	1775	29
NMHE-2024-17.2a-38	0.1086	0.76	4.4574	1.24	0.2977	0.98	0.79	94	1680	15	1723	10	1776	14
NMHE-2024-04-130	0.1086	1.08	4.7017	1.64	0.3140	1.23	0.75	99	1761	19	1768	14	1776	20
NMHE-2024-04-116	0.1086	0.91	4.4647	1.30	0.2982	0.93	0.71	94	1682	14	1724	11	1776	17
NMHE-2024-04-228	0.1086	0.86	4.2528	1.64	0.2840	1.40	0.85	90	1611	20	1684	14	1776	16
NMHE-2024-04-238	0.1086	1.04	4.3981	1.79	0.2937	1.46	0.81	93	1660	21	1712	15	1776	20
NMHE-2024-17.2a-1375	0.1086	0.90	4.7526	1.67	0.3173	1.41	0.84	100	1776	22	1777	14	1777	17
NMHE-2024-17.2a-703	0.1087	0.97	4.5918	1.60	0.3064	1.27	0.79	97	1723	19	1748	13	1778	18
NMHE-2024-04-1067	0.1087	0.87	4.3055	1.49	0.2872	1.21	0.81	91	1628	18	1694	13	1778	16
NMHE-2024-04-771	0.1088	1.39	4.5017	2.10	0.3000	1.57	0.75	95	1691	23	1731	18	1780	27
NMHE-2024-04-547	0.1089	2.28	4.7447	4.61	0.3161	4.01	0.87	99	1770	62	1775	39	1781	42
NMHE-2024-17.2a-3850	0.1090	1.51	4.5283	2.27	0.3013	1.70	0.75	95	1698	26	1736	19	1783	28
NMHE-2024-04-571	0.1090	1.55	4.8658	2.28	0.3237	1.67	0.73	101	1808	26	1796	20	1783	29
NMHE-2024-04-419	0.1091	1.57	4.7722	2.31	0.3174	1.69	0.73	100	1777	26	1780	19	1784	28
NMHE-2024-17.2a-1955	0.1091	1.05	4.8988	1.81	0.3257	1.48	0.82	102	1818	24	1802	15	1784	19
NMHE-2024-04-943	0.1091	2.03	5.2080	3.17	0.3461	2.44	0.77	107	1916	41	1854	28	1785	38
NMHE-2024-17.2a-3851	0.1091	1.66	4.9282	2.25	0.3275	1.52	0.68	102	1826	24	1807	20	1785	31
NMHE-2024-17.2a-1127	0.1092	1.03	4.6883	1.68	0.3114	1.33	0.79	98	1748	21	1765	14	1786	19
NMHE-2024-04-1026	0.1092	1.24	4.4860	1.80	0.2980	1.30	0.72	94	1681	19	1728	15	1786	23
NMHE-2024-17.2a-3130	0.1092	1.17	4.9872	1.93	0.3311	1.54	0.80	103	1844	25	1817	17	1787	22
NMHE-2024-17.2a-3056	0.1093	1.16	4.8028	1.73	0.3187	1.28	0.74	100	1784	20	1785	15	1788	21
NMHE-2024-04-225	0.1093	1.05	4.4301	1.85	0.2940	1.52	0.82	92	1661	22	1718	15	1788	19
NMHE-2024-15.1a-164	0.1095	1.34	4.7190	2.06	0.3126	1.56	0.76	98	1754	24	1771	17	1791	24
NMHE-2024-04-188	0.1095	1.07	4.5443	1.55	0.3010	1.12	0.72	94	1696	17	1739	13	1791	20
NMHE-2024-04-1094	0.1095	1.15	4.9907	1.71	0.3306	1.27	0.74	103	1841	20	1818	14	1791	21
NMHE-2024-04-688	0.1096	1.53	4.6745	2.51	0.3092	1.99	0.79	97	1737	31	1763	22	1793	29
NMHE-2024-04-712	0.1097	1.75	4.5705	2.45	0.3023	1.71	0.70	95	1703	25	1744	20	1794	32

NMHE-2024-17.2a-3343	0.1103	1.77	4.8710	2.26	0.3204	1.40	0.62	99	1791	22	1797	19	1804	32
NMHE-2024-04-883	0.1104	1.64	4.8470	2.29	0.3183	1.60	0.70	99	1782	25	1793	20	1807	31
NMHE-2024-04-314	0.1105	1.21	4.8524	1.79	0.3186	1.32	0.74	99	1783	21	1794	15	1807	22
NMHE-2024-15.1a-1319	0.1105	1.96	5.1857	3.11	0.3404	2.42	0.78	104	1889	40	1850	27	1807	36
NMHE-2024-04-236	0.1110	1.14	4.9323	1.72	0.3222	1.29	0.75	99	1801	20	1808	15	1816	21
NMHE-2024-17.2a-2565	0.1112	1.09	4.8501	1.67	0.3164	1.27	0.76	97	1772	20	1794	14	1819	19